



## Aspects of Mathematical Morphology

K. Michielsen<sup>1</sup>, H. De Raedt<sup>1</sup> and J.Th.M. De Hosson<sup>2</sup>

<sup>1</sup>*Centre for Theoretical Physics, Materials Science Centre*

<sup>2</sup>*Department of Applied Physics, Materials Science Centre and*

*Netherlands Institute for Metals Research*

*University of Groningen, Nijenborgh 4*

*NL-9747 AG Groningen, The Netherlands*

K.F.L.Michielsen@phys.rug.nl, H.A.De.Raedt@phys.rug.nl,

J.T.M.De.Hosson@phys.rug.nl

<http://www.compphys.rug.nl>

In this paper we review the basic concepts of integral-geometry-based morphological image analysis. This approach yields an objective, numerical characterization of two- and three-dimensional patterns in terms of geometrical and topological descriptors called Minkowski functionals. We review its mathematical foundation and show that it is easy to put the theory into practice by presenting simple computer algorithms to perform the analysis. Illustrative examples are given of applications of this approach to simple lattice structures, random point sets and minimal surfaces. As a more advanced application we show how the technique can be used to obtain a morphological characterization of computer tomography images of metal foams.

Keywords: Morphology, Euler characteristic, integral geometry, Minkowski functionals, computer tomography images, metal foams.

## Content:

1.	Introduction . . . . .	2
2.	Integral geometry: Theory . . . . .	4
2.1	Image measurements . . . . .	4
2.2	Minkowski addition and subtraction . . . . .	5
2.3	Parallel sets . . . . .	5
2.4	Convex sets and Minkowski functionals . . . . .	7
2.5	Convex rings and additive image functionals . . . . .	9
2.6	Relation to topology and differential geometry . . . . .	10
2.7	Application to images . . . . .	12
2.8	Integral geometry on a hypercubic lattice . . . . .	14
2.9	Integral geometry on a lattice: Alternative formulation . . . . .	15
3.	Integral geometry in practice . . . . .	19
3.1	Minkowski functionals . . . . .	20
3.2	Computer program . . . . .	21
3.3	Analysis of point patterns . . . . .	22
3.4	Analysis of digitized and thresholded images . . . . .	22
3.5	What integral geometry cannot do . . . . .	23
3.6	Reducing digitization errors . . . . .	24
3.7	Normalization of image functionals . . . . .	24
4.	Illustrative examples . . . . .	24
4.1	Regular lattices . . . . .	25
4.2	Dislocations . . . . .	26
4.3	Random point sets . . . . .	29
4.4	Topology of triply periodic minimal surfaces . . . . .	33
5.	Computer tomography images of metal foams . . . . .	36
5.1	Computation of 3D Minkowski functionals . . . . .	37
5.2	Aluminium foams with closed-cell and open-cell structure . . . . .	38
6.	Summary . . . . .	39
7.	Acknowledgements . . . . .	40
	Appendix A. Algorithm . . . . .	40
	Appendix B. Programming example (Fortran 90) . . . . .	42
	Appendix C. Derivation of Eq.(36) . . . . .	47
	Appendix D. Proof of Eq.(56) . . . . .	48
	Appendix E. Proof of Eq.(57) . . . . .	51
1.	Figure Captions . . . . .	54
2.	References . . . . .	57

# 1. Introduction

Geometrical patterns are encountered in many different fields of science and technology [1, 2]. Very often these patterns come in the form of photographic images. In general, the purpose of image analysis is to find out what is in these images [3 – 7]. Describing this information in words is one extreme form of characterizing the image, another extreme form is to assign one or more numbers to the observation. In this paper we only consider the latter.

In particular we will analyze two-dimensional (2D) and three-dimensional (3D) patterns by numerical representations of the corresponding images in terms of two-valued functions. Therefore a numerical characterization of features in the image requires that the image has been digitized, i.e. that the image has been converted to numerical form [3 – 6]. This conversion may include additional digital image processing steps [3 – 6] to enhance the quality of the images. If the image contains color or gray-level information, the digitization process should include the mapping of the spatial and color/brightness information in the image onto a collection of black-and-white image elements [3 – 6]. For simplicity we will use the term *pixel* to refer to both 2D and 3D image elements.

Morphology is a branch of biology dealing with the form and structure of animals and plants. The same word is used for the study of the geometry and topology of patterns. *Integral-Geometry Morphological Image Analysis* (MIA for short from now on) employs additive image functionals to assign numbers to the shape and connectivity of patterns formed by the pixels in the image. Integral geometry [8, 9, 10] provides a rigorous mathematical framework to define these image functionals. A fundamental theorem (discussed below) of integral geometry [8] states that under certain conditions, the number of different additive image functionals is equal to the dimension of the pattern plus one. Thus, in the case of a 2D (3D) image there are exactly 3 (4) of these functionals, called quermassintegrals or Minkowski functionals. For a given image the first step in MIA is to compute these functionals themselves. The second step is to study the behavior of the three or four numbers as a function of some control parameters, such as time, density etc.

A remarkable feature of MIA is the big contrast between the simplicity of implementation and use and the level of sophistication of the mathematical theory. Indeed, as will be explained below, the calculation of the image functionals merely amounts to the proper counting of e.g. faces, edges and vertices of pixels. The application of MIA requires little computational effort. Another appealing feature of MIA is that the image functionals have a geometrically and topologically clear interpretation: For 2D images they correspond to the area, boundary length, and connectivity number. The four functionals for 3D images are the volume, surface area, integral mean curvature and connectivity number.

This paper gives an overview of the various aspects of MIA, with an emphasis

on the practical application. MIA has proven to be very useful to describe the morphology of porous media and complex fluids [11 – 14], the large-scale distribution of matter in the Universe [14 – 16], regional seismicity realizations [17], quantum motion in billiards [18], microemulsions [14, 19], patterns in reaction diffusion systems [14, 20], spinodal decomposition kinetics [14, 21, 22], and the dewetting structure in liquid crystal and liquid metal films [23], and in polymer films [24]. In many cases additional information can be extracted from the pattern by making assumptions about size, shape and distribution of the objects. Usually this involves making a probabilistic model of the pattern and comparing the Minkowski functionals of the model with those of the images. Applications of this stochastic-geometry approach to model natural phenomena can be found in [10].

In the preceding discussion we took for granted that the digitized images are free of noise and other artifacts that may affect the geometry and topology of the structures of interest. Such perfect images are easily generated by computer and are very useful for the development of theoretical concepts and models. Unfortunately, genuine images or patterns obtained from computer simulations are seldom perfect. Therefore some form of image processing may be necessary before attempting to make measurements of the features in the image.

Digital image processing is very important for many industrial, medical and scientific applications. There is a vast amount of literature on this subject so we can only cite a few books here [3 – 6]. There also is a huge number of different processing steps and methods. The type of measurements that will be performed on the image is an important factor in making a selection of the most appropriate processing steps.

In MIA the geometric and topological content of the image are of prime importance and this should be reflected in the operations that are used to enhance the image quality. The morphological image processing (MIP) technique [25 – 28] is well-adapted for this purpose because MIP and MIA are based on the same mathematical roots. In the present review we will not discuss this very important aspect of image processing but focus entirely on the problem of pattern characterization in terms of morphological descriptors.

This review is structured as follows. Section 2 reviews the mathematical concepts of integral geometry as far as they are relevant to MIA. In section 3 we describe how to use MIA in practice and provide algorithms (including examples of computer code) to compute the morphological descriptors. In section 4 we apply MIA to simple point patterns, random point sets and geometrical objects (minimal surfaces) to illustrate the salient features of MIA. Section 5 discusses the application of MIA to computer tomography images of metal foams. Our conclusions are given in Section 6.

## 2. Integral geometry: Theory

In this section we review the theoretical framework that lies at the heart of integral-geometry-based morphological image analysis. For simplicity we adopt the following conventions:

- We make no distinction between two and three-dimensional images, e.g. we always write “pixel”, also if we actually mean voxel. We consider black-and-white images only, unless mentioned explicitly.
- The background color of an image is white. Pixels that are set are black, others are white. This corresponds to the way one normally draws and prints black-and-white images on paper. On a display the roles of black and white are reversed.
- Definitions are printed slanted.

### 2.1 Image measurements

The purpose of image analysis is to extract information from the image. Integral (and differential) geometry provides information on the geometrical and topological structure of sets of points in Euclidean space. In an image, the presence of a point in space is represented by a pixel that is black. Thus, objects in Euclidean space are represented by a collection of black pixels. Empty space corresponds to white pixels.

A function that assigns a number to a black-and-white image is called an *image functional* [27]. An image functional performs a measurement of certain properties or features in the image, such as the brightness, or location of objects, their surface, perimeter, size distribution etc. An example of an image functional  $\varphi$  is the area of black pixels on a background of white pixels. If  $P_1$  and  $P_2$  are two patterns of black pixels we obviously have

$$\varphi(P_1 \cup P_2) = \varphi(P_1) + \varphi(P_2) - \varphi(P_1 \cap P_2) \quad . \quad (1)$$

The last term in (1) compensates for the double counting of black pixels that are common to  $P_1$  and  $P_2$ . Image functionals that share property (1) are called *additive*. Intuitively it may seem obvious to require image functionals to be additive. In general one would like to avoid counting a feature in an image more than once.

Additive image functionals play a central role in integral-geometry but this does not mean that these are the only useful image functionals. Indeed there are many image functionals that are not additive but yield valuable information on specific features of an image [3]. As a prominent example, we mention the two-point correlation function of the positions of the black pixels (i.e. the Fourier transform of the structure factor). This is a non-additive functional but it certainly yields very useful information about the spatial distribution of the black pixels.

Another important property we would like to have is that the value of the image functional does not depend on the choice of the coordinate system. Formally we say that an image functional  $\varphi$  is *motion invariant* if  $\varphi(sA) = \varphi(A)$  for  $s \in \mathcal{S}$ . Here  $\mathcal{S}$  denotes the group of all symmetry operations in the  $d$ -dimensional Euclidean space  $\mathbb{R}^d$ .

A key point of the theory reviewed in the eight subsections to come is that there are only  $d + 1$  fundamentally different, motion invariant, additive image functionals that describe the morphological content of a  $d$ -dimensional array of pixels. These functionals are directly related to simple geometrical concepts. The reader who is not interested in the mathematical aspects of integral geometry can skip the rest of this section and go directly to section 3.

## 2.2 Minkowski addition and subtraction

Consider two sets of points in Euclidean space (e.g. two images), specified by the position vectors  $A = \{a_1, \dots, a_n\}$  and  $B = \{b_1, \dots, b_m\}$ . Translating every point of  $A$  by  $b_i$ , for  $i = 1, \dots, m$  and collecting all points yields a new set of points

$$C = A \oplus B = B \oplus A = \bigcup_{\substack{i=1, \dots, n \\ j=1, \dots, m}} a_i + b_j \quad , \quad (2)$$

which is called the *Minkowski sum* of the sets  $A$  and  $B$ . The operation  $\oplus$  is called *Minkowski addition*. Similarly *Minkowski subtraction*  $\ominus$  is defined by

$$C = A \ominus B = B \ominus A = \bigcap_{\substack{i=1, \dots, n \\ j=1, \dots, m}} a_i + b_j \quad , \quad (3)$$

i.e. we translate every point of  $A$  by every element of  $B$  and only keep those points that intersect.

Minkowski addition increases the number of points. Minkowski subtraction removes points from an image. Unless  $B$  contains the origin, image  $A \ominus B$  is not necessarily a subset of image  $A$ . The operations  $\oplus$  and  $\ominus$  play a central role in morphological image processing [27]. In this context the former is often called *dilation* and has the effect of “inflating” the image  $A$ . The latter is called *erosion* and results in a “shrinking” of  $A$ . For a review of the properties of Minkowski algebra, see e.g. Ref. [8, 27].

### 2.3 Parallel sets

Consider the set of points of a line  $L$  of length  $a$  embedded in one-dimensional (1D) Euclidean space. We take a similar segment  $S_r^{(1)}$  of length  $2r$  and put the center of this line at each point of the line  $L$ . How does the union of all these points look like? Obviously it is another line that is longer than  $L$ . The sets  $L$  (black line),  $S_r^{(1)}$  (gray line) and  $L_r$  (union of black and gray lines), the result of this operation, are shown in Fig.1. In terms of the operations discussed above, it is clear that  $L_r = L \oplus S_r^{(1)}$ . The length  $l$  of  $L_r$  is given by

$$l(L_r) = a + 2r = l(L) + 2r \quad . \quad (4)$$

The set  $L_r$  is called the parallel set of  $L$  at a distance  $r$ .

The one-dimensional case readily extends to two and three dimensions. In Euclidean space the *parallel set*  $A_r$  of  $A$  is defined by

$$A_r = A \oplus S_r^{(d)} \quad , \quad (5)$$

where  $S_r^{(d)}$  denotes a  $d$ -dimensional sphere of radius  $r$ . Let us consider some simple examples, e.g. a circular disk  $D$  of radius  $a$ , a square  $Q$  of edge length  $a$  and an equilateral triangle  $T$  of side length  $a$  embedded in the two-dimensional (2D) Euclidean space. Take a disc of radius  $r$  and perform the same operation as in the one dimensional (1D) case. Put the center of the disc of radius  $r$  at each point of  $D$  (or  $Q$  or  $T$ ) and consider the union of all points. The resulting parallel sets  $D_r$ ,  $Q_r$  and  $T_r$  are shown in Fig.2. The area  $U$  of  $D_r$ ,  $Q_r$  and  $T_r$  is given by

$$U(D_r) = \pi a^2 + 2\pi a r + \pi r^2 \quad , \quad (6a)$$

$$U(Q_r) = a^2 + 4a r + \pi r^2 \quad , \quad (6b)$$

$$U(T_r) = \frac{\sqrt{3}}{4} a^2 + 3a r + \pi r^2 \quad . \quad (6c)$$

The formulae (6) suggest that there may be a general relationship between the area of the original set and its parallel set at a distance  $r$ . It is not difficult to see that the areas of the three parallel sets can be written as

$$U(K_r) = U(K) + P(K)r + \pi r^2 \quad , \quad (7)$$

where  $P(K)$  denotes the boundary length (or perimeter) of the geometrical object  $K$ .

As a last example we consider a cube  $C$  of edge length  $a$  embedded in three-dimensional (3D) space. A simple calculation shows that the volume  $V$  of the parallel set  $C_r$  can be written as

$$V(C_r) = a^3 + 6a^2r + 3a\pi r^2 + \frac{4\pi}{3}r^3 \quad . \quad (8)$$

Again, (8) suggests the generalization

$$V(K_r) = V(K) + S(K)r + 2\pi B(K)r^2 + \frac{4\pi}{3}r^3 \quad , \quad (9)$$

where  $S(K)$  is the surface area and  $B(K)$  is the *mean breadth*.

The examples presented above suggest that for a sufficiently simple 3D (2D) geometrical object, the change in the volume (area) can be computed from the original volume, area, and mean breadth (area and perimeter), as long as we inflate or deflate the object without changing its topology. In fact these relations only hold for convex sets. Convex sets play an important role in integral geometry and are the key to the morphological characterization of sets of points in Euclidean space. Obviously, sets of pixels can be analyzed using these concepts too. However, to be useful in practice, there should be no constraints on the shape of the objects. The purpose of the next two subsections is to discuss the generalization of the above concept to objects of arbitrary shape.

#### 2.4 Convex sets and Minkowski functionals

A collection of points  $K$  in the  $d$ -dimensional Euclidean space  $\mathbb{R}^d$  is called a *convex set* if for every pair of points in  $K$ , the entire line segment joining them also lies in  $K$ . A convex set with nonempty interior is called a *convex body*. A single point  $\mathbf{x} \in \mathbb{R}^d$  is also a convex set and convex body. We will only consider convex sets that are bounded and closed, i.e. that are *compact*. The class of all compact convex sets is denoted by  $\mathbb{K}$ .

The parallel set  $K_r = K \oplus S_r^{(d)}$  of a compact convex set  $K \in \mathbb{K}$  at a distance  $r$  is the union of all closed spheres of radius  $r$ , the centers of which are points of  $K$  [9]. The operation of taking a parallel set preserves the properties of convexity and compactness, i.e.  $K_r \in \mathbb{K}$  [10].

The general expression for the volume  $v^{(d)}$  of the parallel body  $K_r$  at a distance  $r$  of a convex body  $K$ , is given by the Steiner formula [8]

$$v^{(d)}(K_r) = \sum_{\nu=0}^d \binom{d}{\nu} W_{\nu}^{(d)}(K) r^{\nu} \quad , \quad (10)$$

where the  $W_{\nu}^{(d)}(K)$  are called *quermassintegrals* or *Minkowski functionals*. Their relation to the familiar geometrical quantities is given in Table I. Clearly (10) contains the results for the simple examples given in the previous subsection as special cases.



Table.I Relation between the Minkowski functionals  $W_\nu^{(d)}(K)$  of a convex set  $K$  and conventional geometrical quantities.

	$d = 1$	$d = 2$	$d = 3$
$W_0^{(d)}(K)$	$l(K)$	$U(K)$	$V(K)$
$W_1^{(d)}(K)$	2	$P(K)/2$	$S(K)/3$
$W_2^{(d)}(K)$	–	$\pi$	$2\pi B(K)/3$
$W_3^{(d)}(K)$	–	–	$4\pi/3$

It can be shown [8] that the Minkowski functionals are

- Motion invariant:  $\varphi$  is motion invariant if  $\varphi(sK) = \varphi(K)$  for  $s \in \mathcal{S}$ .
- $C$ -additive: A functional is  $C$ -additive if  $\varphi(K_1 \cup K_2) = \varphi(K_1) + \varphi(K_2) - \varphi(K_1 \cap K_2)$  for  $K_1, K_2 \in \mathbb{K}$  and  $K_1 \cup K_2 \in \mathbb{K}$ . The notion of  $C$ -additive (means additive on the set  $\mathbb{K}$ ) is not just a technical one because the union of two convex sets is not necessarily convex, although the intersection is.
- Continuity:  $\varphi$  is *continuous* if  $\lim_{l \rightarrow \infty} \varphi(K_l) = \varphi(K)$  whenever  $\{K_l\}$  is a sequence of compact sets such that  $\lim_{l \rightarrow \infty} K_l = K$  in the Hausdorff metric [27]. Intuitively, this continuity property of  $\varphi$  means that whenever the compact convex sets  $K_l$  approach the compact convex set  $K$ , also  $\varphi(K_l)$  approaches  $\varphi(K)$ . This is a rather technical condition that is satisfied when we limit ourselves to sets of pixels.
- Monotonically increasing:  $\varphi$  is *monotonically increasing*  $\varphi(A) \leq \varphi(B)$  if  $A \subseteq B$ . In simple terms, the value of the Minkowski functionals of a set  $A$  will not decrease if  $A$  becomes larger.

A fundamental result in integral geometry is the completeness of the family of Minkowski functionals. A theorem by Hadwiger [8] states that every motion invariant,  $C$ -additive and continuous functional  $\varphi$  over  $\mathbb{K}$  can be written as

$$\varphi(K) = \sum_{\nu=0}^d a_\nu W_\nu^{(d)}(K) \quad , \quad (11)$$

with suitable coefficients  $a_\nu \in \mathbb{R}$ . A similar result holds if  $\varphi(K)$  is  $C$ -additive and monotonically increasing. Then the numbers  $a_\nu$  are non-negative. In other words, the  $d+1$  Minkowski functionals form a complete system of morphological measures on the class of convex sets  $\mathbb{K}$  [8].

MIA uses additive image functionals to characterize images. Of course we prefer to use motion invariant, additive image functionals. If we could replace “ $C$ -additive” by “additive” then Hadwiger’s theorem would tell us that there are no more, no less than  $d+1$  different additive image functionals. This would imply that we would have to switch to non-additive or coordinate-system-dependent image functionals

to find additional non-morphological structure in the image. However, in general an image is not a convex set of points. The extension of Hadwiger's theorem to additive instead of  $C$ -additive image functionals requires further consideration. On the positive side, in the end it turns out that Hadwiger's completeness theorem holds for arbitrary images as well.

## 2.5 Convex rings and additive image functionals

The results of the previous subsection can be generalized to a much more general class of objects by considering the *convex ring* [8]  $\mathcal{R}$ , the class of all subsets  $A$  of  $\mathbb{R}^d$  which can be expressed as finite unions of compact convex sets

$$A = \bigcup_{i=1}^l K_i \quad ; \quad K_i \in \mathbb{K} \quad . \quad (12)$$

If  $A_1$  and  $A_2$  both belong to  $\mathcal{R}$  then so do  $A_1 \cup A_2$  and  $A_1 \cap A_2$ . As before, an additive functional  $\varphi$  has the property  $\varphi(A_1 \cup A_2) = \varphi(A_1) + \varphi(A_2) - \varphi(A_1 \cap A_2)$ . Motion invariance of  $\varphi$  on  $\mathcal{R}$  is defined as for  $\varphi$  on  $\mathbb{K}$ . Obviously any image is an instance of the convex ring  $\mathcal{R}$ , the pixels being the convex sets and elements of  $\mathbb{K}$ .

Fundamental to the extension from  $\mathbb{K}$  to  $\mathcal{R}$  is the *Euler characteristic* or *connectivity number*  $\chi$  defined as [8]

$$\chi(K) = \begin{cases} 1 & K \neq \emptyset \\ 0 & K = \emptyset \end{cases} \quad , \quad (13)$$

for all  $K \in \mathbb{K}$ . The Euler characteristic is an additive, motion invariant functional on  $\mathcal{R}$  [8]. For an element  $A$  of the convex ring  $\mathcal{R}$ , the use of the property of additivity of  $\chi$  yields

$$\chi(A) = \chi\left(\bigcup_{i=1}^l K_i\right) = \sum_i \chi(K_i) - \sum_{i < j} \chi(K_i \cap K_j) + \dots + (-1)^{l+1} \chi(K_1 \cap \dots \cap K_l) \quad . \quad (14)$$

The value of  $\chi(A)$  is independent of the representation of  $A$  as a finite union of compact convex sets [8]. Note that all sets appearing on the right hand side of (14) are convex so that we can use (13) to compute the numerical (integer) value of  $\chi(A)$ .

The Euler characteristic can be used to define the Minkowski functionals for all elements of the convex ring  $A \in \mathcal{R}$  [8]. Recalling that a single point  $\mathbf{x} \in \mathbb{R}^d$  is a convex set, we can write the characteristic function of the set  $A$  as  $I_A(\mathbf{x}) = \chi(A \cap \mathbf{x})$ . Then the volume of  $A$  is given by  $W_0^{(d)}(A) = \int_{\mathcal{S}} I_A(s\mathbf{x}) ds$ . Here  $ds$  denotes the motion-invariant kinematical density [8, 9] and the integration is over all elements of  $\mathcal{S}$  [8, 9]. The expression of the volume suggests the following definition [8] of the

Minkowski functionals on  $\mathcal{R}$ :

$$\begin{aligned} W_\nu^{(d)}(A) &= \int_{\mathcal{S}} \chi(A \cap sE_\nu) ds \quad \nu = 0, \dots, d-1, \\ W_d^{(d)}(A) &= \omega_d \chi(A) \quad \omega_d = \pi^{d/2} / \Gamma(1 + d/2) \quad , \end{aligned} \quad (15)$$

where  $E_\nu$  is a  $\nu$ -dimensional plane in  $\mathbb{R}^d$ . The normalization is chosen such that for a  $d$ -dimensional sphere  $S_r^{(d)}$  with radius  $r$ ,  $W_\nu^{(d)}(S_r^{(d)}) = \omega_d r^{d-\nu}$  where  $\omega_d$  denotes the volume of the unit sphere ( $\omega_0 = 1$ ,  $\omega_1 = 2$ ,  $\omega_2 = \pi$ ,  $\omega_3 = 4\pi/3$ ) [14].

The Minkowski functionals inherit from  $\chi$  the property of additivity

$$\begin{aligned} W_\nu^{(d)}(A) &= W_\nu^{(d)}\left(\bigcup_{i=1}^l K_i\right) = \sum_i W_\nu^{(d)}(K_i) - \sum_{i<j} W_\nu^{(d)}(K_i \cap K_j) + \dots \\ &\quad + (-1)^{(l+1)} W_\nu^{(d)}(K_1 \cap \dots \cap K_l) \quad , \end{aligned} \quad (16)$$

and motion invariance.

It is not difficult to see that Hadwiger's completeness theorem (11) carries over from the class of convex sets  $\mathbb{K}$  to the ring  $\mathcal{R}$ . Replacing  $K$  by  $A = \bigcup_{i=1}^l K_i$  where  $K_i \in \mathbb{K}$  and using (16) repeatedly one finds that (11) holds for any element of  $\mathcal{R}$  [8]. Thus, the  $d+1$  Minkowski functionals form a complete system of additive functionals on the set of objects that are unions of a finite number of convex sets [8].

For completeness and also because we make use of it later, we state one more important result in integral geometry, the so-called *kinematic formulae* [8]

$$\int_{\mathcal{S}} M_\mu^{(d)}(A \cap sB) ds = \sum_{\nu=0}^{\mu} \binom{\mu}{\nu} M_\nu^{(d)}(A) M_{\mu-\nu}^{(d)}(B) \quad , \quad (17)$$

where

$$M_\mu^{(d)}(A) = \frac{\omega_{d-\mu}}{\omega_\mu \omega_d} W_\mu^{(d)}(A) \quad ; \quad \mu = 0, \dots, d \quad , \quad (18)$$

defines the *normalized Minkowski functionals*. The relation between the normalized Minkowski functionals  $M_\nu^{(d)}(K)$  of a convex set  $K$  and conventional geometrical quantities are given in Table II. The kinematic formulae (17) are very useful in stereology and stochastic geometry [8, 9, 25]. They also play a key role in deriving configurational averages of Minkowski functionals.

In translating these abstract mathematical concepts to a practical scheme it is important to keep in mind the conditions under which the above theorems hold. Fortunately, in practice, this is easy to do. The crucial step is to decompose the image into a union of convex sets so that we can use the theoretical results that hold on the convex ring. We address this issue in section 2.7.

Table.II Relation between the normalized Minkowski functionals  $M_\nu^{(d)}(K)$  of a convex set  $K$  and conventional geometrical quantities in Euclidean space. Note that the Euler characteristic of a convex set is equal to one.

	$d = 1$	$d = 2$	$d = 3$
$M_0^{(d)}(K)$	$l(K)$	$U(K)$	$V(k)$
$M_1^{(d)}(K)$	$\chi(K)/2$	$P(K)/2\pi$	$S(k)/8$
$M_2^{(d)}(K)$	–	$\chi(K)/\pi$	$B(K)/\pi$
$M_3^{(d)}(K)$	–	–	$3\chi(K)/4\pi$

## 2.6 Relation to topology and differential geometry

The Euler characteristic  $\chi$  is identical to the one defined in algebraic topology [8]. For  $d = 2$ ,  $\chi(A)$  equals the number of connected components minus the number of holes. In three dimensions  $\chi(A)$  is given by the number of connected components minus the number of tunnels plus the number of cavities. Some examples are shown in Fig.3. The Euler characteristic describes  $A$  in a purely topological way, i.e. without reference to any kind of metric.

Very often one is interested in the topology of the surface  $\partial A$  of  $A$  [2, 15]. The Euler characteristic of  $\partial A$  is directly related to that of  $A$ , namely

$$\chi(\partial A) = \chi(A)[1 - (-1)^n] \quad , \quad (19)$$

where  $n$  is the dimension of the body  $A$  ( $n \leq d$ ) [19].

The principal curvatures of a surface are useful quantities for the numerical characterization of the surface of a 3D body. They are defined as follows. Consider a point on the surface and the vector through this point, normal to the surface. A plane containing this normal vector intersects the surface. This intersection is a planar curve with a curvature called the normal curvature. Rotation of the plane about the normal produces various planar curves with different values of normal curvature. The extreme values of the normal curvatures are called the *principal curvatures*  $\kappa_1$  and  $\kappa_2$  of a surface. These two curvatures can be combined to give two useful measures of the curvature of a surface, namely the Gaussian and mean curvature defined as  $G = \kappa_1\kappa_2$  and  $H = (\kappa_1 + \kappa_2)/2$  respectively. The integral mean curvature  $H$  and integral Gaussian curvature  $G$  are given by

$$H(A) = \frac{1}{2} \int_{\partial A} \left( \frac{1}{R_1} + \frac{1}{R_2} \right) df \quad , \quad (20)$$

and

$$G(A) = \int_{\partial A} \frac{1}{R_1 R_2} df \quad , \quad (21)$$

respectively. Here  $R_1 = 1/\kappa_1$  and  $R_2 = 1/\kappa_2$  are the principal radii of curvature of  $A$  and  $df$  is the area element on  $A$ . For  $H$  and  $G$  to be well defined the boundary  $\partial A$  should be regular.

The mean breadth is proportional to the integral mean curvature:

$$H(A) = 2\pi B(A) \quad . \quad (22)$$

The Euler characteristic of  $\partial A$  is closely related to the integral Gaussian curvature  $G$  and the genus  $g$  (number of handles, i.e. number of holes in the closed surface):

$$G(A) = 2\pi\chi(\partial A) \quad , \quad \chi(\partial A) = 2(1 - g) \quad . \quad (23)$$

Note that integral geometry imposes no regularity conditions on the boundary  $\partial A$  of the objects:  $H(A)$  and  $\chi(A)$  are always well-defined.

## 2.7 Application to images

Each pixel in a 2D (3D) black-and-white image is a convex set. Therefore such images may be considered as an element of the convex ring  $\mathcal{R}$  and we can invoke integral geometry to build additive image functionals to measure features in the image. However, as mentioned before, some care has to be taken because the Minkowski functionals take known values on convex sets only.

The key to the practical application of integral geometry to images is the additivity of  $\chi$  (see (14) ): We can compute the Minkowski functionals of an image  $A$  by decomposing  $A$  into convex sets  $K_i$ . However, if we would take for  $\{K_i\}$  all black pixels (assuming the background consists of white pixels), then we would have to compute all the intersections that appear in (14) . Although this can be done, it is much more expedient to take a slightly different route.

First we write each pixel  $K$  as the union of the disjoint collection of its interior body, interior faces (in 3D only), open edges and vertices [19]. We will denote the interior of a set  $A$  by  $\check{A} = A \setminus \partial A$ . The values of the Minkowski functionals of the open interior of a  $n$ -dimensional body  $A \in \mathcal{R}$  embedded in  $\mathbb{R}^d$  ( $n \leq d$ ) are given by [19]

$$W_\nu^{(d)}(\check{A}) = (-1)^{d+n+\nu} W_\nu^{(d)}(A) \quad ; \quad \nu = 0, \dots, d \quad . \quad (24)$$

By making use of the additivity of the Minkowski functionals (see (16) ) and the fact that there is no overlap between open sets on a lattice, the values of the Minkowski functionals on the whole pattern  $\mathcal{P}$  may be obtained from

Table.III Minkowski functionals  $W_\nu^{(2)}$  ( $\nu = 0, \dots, d = 2$ ) for the open sets  $\check{N}_m$ , the basic building blocks of a square in two-dimensional Euclidean space.  $\check{Q}$ : open square of edge length  $a$ ;  $\check{L}$ : open edge of length  $a$ ;  $\check{P}$ : vertex.

$m$	$\check{N}_m$	$W_0^{(2)}$	$W_1^{(2)}$	$W_2^{(2)}$
0	$\check{P}$	0	0	$\pi$
1	$\check{L}$	0	$a$	$-\pi$
2	$\check{Q}$	$a^2$	$-2a$	$\pi$

Table.IV Minkowski functionals  $W_\nu^{(3)}$  ( $\nu = 0, \dots, d = 3$ ) for the open sets  $\check{N}_m$ , the basic building blocks of a cube in three-dimensional Euclidean space.  $\check{C}$ : open cube of edge length  $a$ ;  $\check{Q}$ : open square of edge length  $a$ ;  $\check{L}$ : open edge of length  $a$ ;  $\check{P}$ : vertex.

$m$	$\check{N}_m$	$W_0^{(3)}$	$W_1^{(3)}$	$W_2^{(3)}$	$W_3^{(3)}$
0	$\check{P}$	0	0	0	$4\pi/3$
1	$\check{L}$	0	0	$\pi a/3$	$-4\pi/3$
2	$\check{Q}$	0	$2a^2/3$	$-2\pi a/3$	$4\pi/3$
3	$\check{C}$	$a^3$	$-2a^2$	$\pi a$	$-4\pi/3$

$$W_\nu^{(d)}(\mathcal{P}) = \sum_m W_\nu^{(d)}(\check{N}_m) n_m(\mathcal{P}) \quad ; \quad \nu = 0, \dots, d \quad , \quad (25)$$

where  $n_m(\mathcal{P})$  denotes the number open sets  $\check{N}_m$  of type  $m$  present in  $\mathcal{P}$ . On a square and cubic lattice there are  $d + 1$  open sets  $\check{N}_m$ :  $\check{N}_0$  corresponds to a vertex,  $\check{N}_1$  to an open line segment,  $\check{N}_2$  to an open square on both the 2D square and the 3D cubic lattice, and  $\check{N}_3$  to an open cube on the 3D cubic lattice. The calculation of the Minkowski functionals for the building blocks  $\check{N}_m$  of a 2D square and a 3D cubic lattice is given elsewhere [29]. For convenience their values are reproduced in Tables III and IV, respectively. The procedure to calculate  $n_m(\mathcal{P})$  for a square and cubic lattice is given in Appendix A. Note that the value of the Minkowski functionals depends on the type of lattice, i.e. the shape of the pixels, the pattern is represented on. An example of a decomposition of a pattern on a hexagonal lattice is given in Ref.22.

In Fig.4 we show a simple example of the decomposition of the pixels of a two-dimensional black-and-white pattern (left) into squares, edges and vertices (right). For this example, the number of squares  $n_2 = 8$ , number of edges  $n_1 = 24$  and

number of vertices  $n_0 = 16$ . Hence  $W_0 = U = 8a^2$ ,  $W_1 = P/2 = -16a + 24a = 8a$  and  $W_2 = \pi\chi = 8\pi - 24\pi + 16\pi = 0$ , where  $a$  denotes the edge length of the open square and open edge. We further illustrate the procedure to compute the Minkowski functionals by considering the 2D checkerboard pattern with an even number  $L_0$  of cells, of edge length one, in each direction. We consider free and periodic boundary conditions (see Fig.5). The left image in Fig.5 shows the  $4 \times 4$  checkerboard lattice with free boundary conditions, i.e. the pattern is completely surrounded by white pixels. The right image shows the same pattern but with periodic boundary conditions. For the  $L_0 \times L_0$  checkerboard  $\mathcal{P}_F$  with free boundary conditions we find  $n_0(\mathcal{P}_F) = (L_0+1)^2 - 2$ ,  $n_1(\mathcal{P}_F) = 2L_0^2$ ,  $n_2(\mathcal{P}_F) = L_0^2/2$  and hence  $U(\mathcal{P}_F) = L_0^2/2$ ,  $P(\mathcal{P}_F) = 2L_0^2$  and  $\chi(\mathcal{P}_F) = L_0^2/2 - (L_0 - 1)^2$ . Note that this value of  $\chi$  corresponds to the value we find if we calculate  $\chi$  as the number of connected components minus the number of holes, since the number of connected components (black structure) equals one and the number of holes equals  $(L_0/2 - 1)(L_0 - 2)$ . For the  $L_0 \times L_0$  checkerboard  $\mathcal{P}_P$  with periodic boundary conditions we find  $n_0(\mathcal{P}_P) = L_0^2$ ,  $n_1(\mathcal{P}_P) = 2L_0^2$ ,  $n_2(\mathcal{P}_P) = L_0^2/2$  which yields  $U(\mathcal{P}_P) = L_0^2/2$ ,  $P(\mathcal{P}_P) = 2L_0^2$  and  $\chi(\mathcal{P}_P) = -L_0^2/2$ . Note that  $\chi(\mathcal{P}_P)/L_0^2 = \lim_{L_0 \rightarrow \infty} \chi(\mathcal{P}_F)/L_0^2 = -1/2$ .

Summarizing: In practice the calculation of the Minkowski functionals of a black-and-white image amounts to counting vertices, edges, etc.

## 2.8 Integral geometry on a hypercubic lattice

Most modern image acquisition systems are pixel-based. In many cases the pixels represent an average of the signal (light, electrons, ...) over some area or volume of the sample. In other cases, for instance in scanning electron microscope images taken at low magnification, the dimension of the sampled volume is smaller than the dimension of the pixel in the image [3]. Then the pixels represent points that are discrete and well separated and it is no longer evident that the set of pixels corresponds to an image of an object in Euclidean space. In this case, it is more appropriate and correct to regard the image as a collection of points on a square or cubic lattice instead of in continuum space.

Not surprisingly, the concepts of integral-geometry can be used to characterize structure in these situations as well. In fact, the theory reviewed above directly applies if we replace the group  $\mathcal{S}$  of all symmetry operations in  $\mathbb{R}^d$  by the group  $\mathcal{S}'$  of translations, rotations and reflections that leave the finite  $d$ -dimensional, regular (hypercubic) lattice  $\mathbb{Z}^d$  invariant [30 – 33]. In the following we closely follow [33]. In analogy with Eq.(15), on the  $d$ -dimensional lattice the Minkowski functionals are defined by

$$V_d^{(d)}(A) = \chi(A) \quad ,$$

Table.V Relation between the Minkowski functionals  $V_\nu^{(d)}(A)$  on a  $d$ -dimensional hypercubic lattice  $\mathbb{Z}^d$  and the length  $l$ , area  $U$ , perimeter  $P$ , volume  $V$ , surface area  $S$ , integral mean breadth  $B$  and Euler characteristic  $\chi$ .

	$d = 1$	$d = 2$	$d = 3$
$V_0^{(d)}$	$l$	$U$	$V$
$V_1^{(d)}$	$\chi$	$P/4$	$S/6$
$V_2^{(d)}$	—	$\chi$	$2B/3$
$V_3^{(d)}$	—	—	$\chi$

$$V_\nu^{(d)}(A) = \binom{d}{\nu}^{-1} (2^d d!)^{-1} \sum_{s \in \mathcal{S}'} \chi(A \cap sE_\nu) ds \quad ; \quad \nu = 0, \dots, d-1 \quad , \quad (26)$$

where  $E_\nu$  is a  $\nu$ -dimensional plane in  $\mathbb{Z}^d$ . The sum in (26) denotes the sum over all translations, rotations and reflections in  $\mathbb{Z}^d$ . The factor  $2^d d!$  reflects the number of symmetry operations that leave the  $d$ -cubic lattice invariant. Fig.6 shows the basic elements of integral geometry in  $\mathbb{Z}^2$ : an elementary square (a), two connected elementary squares (b), two 0-dimensional planes (lattice points)  $E_0$  and two 1-dimensional planes (horizontal and vertical lines through the lattice points)  $E_1$ .

As in the Euclidean case, the Minkowski functionals (26) also have a intuitively clear meaning. In Table V we summarize the relationships between the Minkowski functionals on  $\mathbb{Z}^d$  and the conventional morphological quantities.

Unlike in the Euclidean case, the Minkowski functionals (26) are no longer homogenous functions of the length scale (which is fixed to one on  $\mathbb{Z}^d$ ). As a consequence kinematic formulae (17) no longer hold but have to be replaced by [33]

$$\frac{1}{2^d d!} \sum_{s \in \mathcal{S}'} V_\mu^{(d)}(A \cap sB) ds = \sum_{\nu=0}^{\mu} \sum_{\kappa=0}^{\nu} \binom{\mu}{\nu} \binom{\kappa}{\nu} V_\nu^{(d)}(A) V_{\mu-\kappa}^{(d)}(B) \quad . \quad (27)$$

In section 4.3 we make use of Eq.(27) to compute analytically the configurational averages of the Minkowski functionals for random distributions of points in  $\mathbb{Z}^d$ .

## 2.9 Integral geometry on a lattice: Alternative formulation

On the two-dimensional square lattice  $\mathbb{Z}^2$ , it is a simple matter to identify the fundamental geometrical elements. Indeed, any image can be decomposed in vertices (points), line segments (edges) connecting the vertices and the squares enclosed by vertices and edges. In Euclidean space, these fundamental elements correspond to the open sets used in section 2.7. Obviously this construction can be made for any dimension  $d$  and any shape of the pixels.



In terms of these fundamental elements, the basic equations of integral geometry take a particularly simple form. The basic reason is that the intersection of a set of e.g. vertices and a set of e.g. edges is empty. We now proceed with this alternative formulation of integral geometry and obtain the (simple) formulae that will actually be used in integral-geometry morphological image analysis (MIA).

We consider the  $d$ -cubic lattice  $\mathbb{Z}^d$ . This lattice can be viewed as the union of the disjoint sets of vertices  $O_0$ , edges  $O_1$ , faces  $O_2$ , cubes  $O_3$  etc. Obviously, in Euclidean space these are the basic open elements (see section 2.7). Any pattern  $A$  on  $\mathbb{Z}^d$  can be decomposed into the elements  $O_\nu$ ,  $\nu = 0, \dots, d$ . This decomposition is trivially unique. An example for  $d = 2$  is given in Fig.7.

Let the functional  $F_\nu(A)$  count the number of elements  $O_\nu$  in  $A$ . It is easy to see that the  $F_\nu$  are functionals on  $\mathbb{Z}^d$  that take positive integer values and are

- additive:  $F_\nu(A \cup B) = F_\nu(A) + F_\nu(B) - F_\nu(A \cap B)$  and  $F_\nu(\emptyset) = 0$
- motion invariant:  $F_\nu(sA) = F_\nu(A)$  where  $s$  denotes all translations, rotations and reflections on  $\mathbb{Z}^d$
- monotonically increasing:  $F_\nu(A) \leq F_\nu(B)$  for  $A \subseteq B$ .

Since there are no other type of fundamental elements in  $\mathbb{Z}^d$  than the  $O_\nu$ 's (i.e. there is nothing else to be counted), any additive and motion-invariant functional  $\varphi$  on  $\mathbb{Z}^d$  must be a linear combination of the form

$$\varphi(A) = \sum_{\nu=0}^d a_\nu F_\nu(A) \quad , \quad (28)$$

where  $a_\nu = \varphi(O_\nu)$ . In this formulation of integral-geometry on a lattice, Hadwiger's representation theorem is almost self-evident. The  $F_\nu$  play the role (but are not the same as) the Minkowski functionals.

We proceed to write the conventional functionals describing the morphology of subsets  $A \subset \mathbb{Z}^d$  as a linear combination of the functionals  $F_\nu(A)$ . It is expedient to introduce the notion of a *simplex*  $S_\nu$ ,  $\nu = 0, \dots, d$ . A vertex ( $S_0$ ), an edge with a vertex at each end ( $S_1$ ), a square surrounded by four edges and four vertices ( $S_2$ ), etc. are examples of simplexes (see Fig.7). Clearly, in Euclidean space the equivalent of a simplex is a closed convex set. Every pattern in  $\mathbb{Z}^d$  has a unique decomposition in terms of simplexes  $S_\nu$ ,  $\nu = 0, \dots, d$ . In the case of a  $d$ -dimensional digital image, each pixel is a simplex  $S_d$ . Hence the decomposition only contains simplexes  $S_d$ .

The topology of a subset  $A$  is characterized by the Euler characteristic. In analogy with the definition of the Euler characteristic  $\chi$  of a convex body, we define the additive and motion invariant functional  $\chi$  by  $\chi(\emptyset) = 0$  and  $\chi(S_\nu) = 1$  for all  $\nu = 0, \dots, d$ . By construction, since every pattern  $A$  has a unique decomposition in terms of the simplexes  $S_\nu$ ,  $\chi(A)$  is uniquely determined by  $\chi(S_\nu)$ , hence  $\chi(A)$  is unique.

Let  $E_d(L)$  denote a  $d$ -cube of linear size  $L$  (see Fig.7 for  $d = 2$ ). Simple counting shows that the number of  $O_\nu$  in  $E_d(L)$  is given by

$$F_\nu(E_d(L)) = \binom{d}{\nu} L^\nu (L+1)^{d-\nu} \quad . \quad (29)$$

We now derive the classical alternating formula for the Euler characteristic [34]. Let us define an additive functional  $\Phi$  by setting  $\Phi(\emptyset) = 0$  and  $\Phi(O_\nu) = (-1)^\nu$ . Then, since  $E_d(L)$  is a disjoint union of the  $O_\nu$ 's, we can use the additivity of  $\Phi$  to write

$$\Phi(E_d(L)) = \sum_{\nu=0}^d \Phi(O_\nu) F_\nu(E_d(L)) \quad , \quad (30a)$$

$$= \sum_{\nu=0}^d (-1)^\nu F_\nu(E_d(L)) \quad , \quad (30b)$$

$$= \sum_{\nu=0}^d (-1)^\nu \binom{d}{\nu} L^\nu (L+1)^{d-\nu} = 1 \quad . \quad (30c)$$

Note that (30) also holds for simplexes since  $S_\nu = E_\nu(1)$ . Therefore  $\Phi(S_\nu) = \chi(S_\nu)$  for all  $\nu = 0, \dots, d$  and hence  $\Phi(A) = \chi(A)$  for any  $A$ . Invoking the additivity of  $F_\nu$ , Eq.(30a) implies that

$$\begin{aligned} \chi(A) &= \sum_{\nu=0}^d \chi(O_\nu) F_\nu(A) = \sum_{\nu=0}^d (-1)^\nu F_\nu(A) \\ &= F_0(A) - F_1(A) + F_2(A) - \dots + (-1)^d F_d(A) \quad , \end{aligned} \quad (31)$$

which is the well-known discrete Euler formula [34].

The logic used to derive this formula can also be used to derive the relationships between the functionals  $F_\nu$  on  $\mathbb{Z}^d$  and the conventional geometrical quantities. We illustrate this for the case of  $d = 2$ . First of all, it is trivial that the area  $U(E_2(L)) = F_2(E_2(L))$  and hence  $U(A) = F_2(A)$ . We already found the expression for the Euler characteristic, namely  $\chi(A) = F_2(A) - F_1(A) + F_0(A)$ . Let us write for the perimeter  $P(A) = a_2 F_2(A) + a_1 F_1(A) + a_0 F_0(A)$ . Since we know that  $P(A = E_2(1)) = 4$ ,  $P(A = E_2(2)) = 8$ , and  $P(A = E_2(3)) = 12$ , we can set up a linear set of equations for the unknowns  $a_0$ ,  $a_1$ , and  $a_2$  and solve it. We find that  $P(A) = -4F_2(A) + 2F_1(A)$ .

Repeating this procedure for all other quantities of interest we find for  $d = 1$

$$l(A) = F_1(A) \quad , \quad (32)$$

for  $d = 2$

$$U(A) = F_2(A), \quad P(A) = -4F_2(A) + 2F_1(A) \quad , \quad (33)$$

and finally for  $d = 3$

$$V(A) = F_3(A), \quad S(A) = -6F_3(A) + 2F_2(A), \quad 2B(A) = 3F_3(A) - 2F_2(A) + F_1(A) \quad . \quad (34)$$

Expressions (32)-(34), together with Eq.(31), will be used as the starting point for the algorithms to compute the morphological descriptors (see section 3). Not surprisingly these expressions are identical to those obtained by starting from the Euclidian version of integral geometry, followed by the procedure described in section 2.7.

For completeness we also derive the discrete analogue of the kinematic formulae in terms of the functionals  $F_\mu$ . As might be anticipated from the discussion above, they should take a very simple form and indeed they do. In general, for fixed  $B$ ,  $\sum_{s \in \mathcal{S}'} F_\mu(A \cap sB)$  is a motion invariant, additive functional of  $A$ . Likewise for fixed  $A$ ,  $\sum_{s \in \mathcal{S}'} F_\mu(A \cap sB) = \sum_{s \in \mathcal{S}'} F_\mu(sA \cap B)$  is a motion invariant, additive functional of  $B$ . Hence we have

$$\frac{1}{2^d d!} \sum_{s \in \mathcal{S}'} F_\mu(A \cap sB) = \sum_{\kappa, \nu=0}^d c_{\kappa\nu} F_\kappa(A) F_\nu(B) \quad ; \quad \mu = 0, \dots, d \quad . \quad (35)$$

Since  $\sum_{s \in \mathcal{S}'} F_\mu(A \cap sB) = \sum_{s \in \mathcal{S}'} F_\mu(sA \cap B)$  we must have  $c_{\kappa\nu} = c_{\nu\kappa}$ . The remaining constants  $c_{\kappa\nu}$  can be computed by looking at specific examples for  $A$  and  $B$ . An example of such a calculation is given in appendix C. In general we find for the kinematic formulae

$$\frac{1}{2^d d!} \sum_{s \in \mathcal{S}'} F_\mu(A \cap sB) = \binom{d}{\mu}^{-1} F_\mu(A) F_\mu(B) \quad ; \quad \mu = 0, \dots, d \quad . \quad (36)$$

The kinematic formulae Eq.(17) and Eq.(27) have a more complicated structure than Eq.(36) but this is hardly a surprise: The left-hand side of Eq.(36) only counts the number of elements of the type  $\mu$  in  $A \cap sB$  and therefore the right-hand side cannot depend on the number of elements in  $A$  or  $B$  that are of a type different from  $\mu$ . The Minkowski functionals that enter the kinematic formulae Eq.(17) and Eq.(27) do not have this property.

The kinematic formulae for the conventional geometrical quantities  $\varphi$  follow from

$$\frac{1}{2^d d!} \sum_{s \in \mathcal{S}'} \varphi(A \cap sB) = \frac{1}{2^d d!} \sum_{s \in \mathcal{S}'} \sum_{\mu=0}^d \varphi(O_\mu) F_\mu(A \cap sB) \quad . \quad (37)$$

Table.VI Values for the geometrical quantities  $\varphi(O_\nu)$ ,  $\nu = 0, \dots, d$ , where  $\varphi$  stands for  $l, U, P, V, S, B$  or  $\chi$ .

	$l$	$U$	$P$	$V$	$S$	$B$	$\chi$
$O_0$	0	0	0	0	0	0	1
$O_1$	1	0	2	0	0	1/2	-1
$O_2$	-	1	-4	0	2	-1	1
$O_3$	-	-	-	1	-6	3/2	-1

The values for  $\varphi(O_\mu)$  can be derived from Eqs.(28) and Eqs.(31)-(34) and are summarized in Table VI. For instance, the kinematic formula for the Euler characteristic reads

$$\begin{aligned} \frac{1}{2^d d!} \sum_{s \in \mathcal{S}'} \chi(A \cap sB) &= \frac{1}{2^{2d} d!} \sum_{s \in \mathcal{S}'} \sum_{\mu=0}^d \chi(O_\mu) F_\mu(A \cap sB) \\ &= \sum_{\mu=0}^d (-1)^\mu \binom{d}{\mu}^{-1} F_\mu(A) F_\mu(B) \quad ; \quad \mu = 0, \dots, d \quad , \quad (38) \end{aligned}$$

which is similar to the expression of Theorem 3.2.5 in [34] and has a much more simple structure than Eq.(27) .

Summarizing: Given a set of pixels representing a black-and-white image there are two ways to perform an integral-geometry analysis of the data. If we consider the pixels as the only information we have, then we use integral geometry on a lattice. If we know or have good arguments to assume that continuum space is a better model we adopt the Euclidean formulation. It will be clear from our discussion below of the practical realization of integral-geometry-based image analysis, one can switch from one to the other formulation without difficulty.

### 3. Integral geometry in practice

An appealing feature of the integral-geometry approach is that the complexity of the mathematical framework is in no way comparable to the simplicity of its practical application. In this section we focus on the practical aspects. Therefore we will omit most mathematical justification, references to relevant work, and discussions of examples. As before we only consider black-and-white images.

From the theory reviewed above, it follows that the  $d+1$  Minkowski functionals form a complete system of additive image functionals on the set of objects that are unions of a finite number of convex sets [8]. In ordinary language this implies that if we restrict ourselves to using additive image functionals we only have to compute

the  $d + 1$  Minkowski functionals to characterize the morphology of the pattern.

In section 2.7, or equivalently section 2.9, we described the basic ideas behind a simple and efficient procedure to compute the Minkowski functionals. In the next two subsections we translate these ideas into a computer program. In subsections 3.3 and 3.4 we focus on the second step of Integral Geometry Morphological Image Analysis (MIA): The study of the dependence of these functionals on some control parameters. In the remaining subsections we discuss several technical topics that are relevant to practical applications.

### 3.1 Minkowski functionals

Consider a 2D lattice filled with black pixels on a white background (see Fig.4). For simplicity we will assume that the pixels are squares and that the linear size of each square has been normalized to one. We want to characterize the geometry and topology of the pattern formed by the black pixels. According to Hadwiger's completeness theorem, there are three additive image functionals, called Minkowski functionals, that describe the morphological content of this 2D pattern, namely the area  $U$ , the perimeter  $P$  and the Euler characteristic  $\chi$ . The latter describes the connectivity (topology) of the pattern: In 2D  $\chi$  equals the number of regions of connected black pixels minus the number of completely enclosed regions of white pixels. Two black pixels are "connected" if and only if they are nearest neighbors or next-nearest neighbors of each other or can be connected by a chain of black pixels that are nearest and/or next-nearest neighbors. Using this definition we find that the Euler characteristic of the pattern shown in Fig.4 is zero.

Conceptually the procedure (that easily extends to three dimensions) to compute these three numbers consists of two steps. First we decompose each black pixel into 4 vertices, 4 edges and the interior of the pixel (see Fig.4). Then we count the total number of squares  $n_2$ , edges  $n_1$  and vertices  $n_0$ . By definition we have  $F_\nu = n_\nu$  for  $\nu = 0, \dots, d$ . A simple algorithm and computer program to count these numbers are described in Appendix A and B respectively. Using Eq.(25) and Table IV, or directly from (33), it follows that the area  $U$ , perimeter  $P$  and Euler characteristic  $\chi$  are given by

$$U = n_2 \quad , \quad P = -4n_2 + 2n_1 \quad , \quad \chi = n_2 - n_1 + n_0 \quad . \quad (39)$$

For the example shown in Fig.4, the number of squares  $n_2 = 8$ , number of edges  $n_1 = 24$  and number of vertices  $n_0 = 16$  and we find  $U = 8$ ,  $P = 16$  and  $\chi = 0$ .

For a 3D cubic lattice filled with black and white pixels the four Minkowski functionals are the volume  $V$ , the surface area  $S$ , the mean breadth  $B$  (see section 2.3), and the Euler characteristic  $\chi$ . In 3D  $\chi$  equals the number of regions of connected black pixels plus the number of completely enclosed regions of white pixels minus the number of tunnels, i.e. regions of white pixels piercing regions of

Table.VII Normalized Minkowski functionals  $M_\nu^{(3)}(K)$  for the elementary convex sets of linear size  $a$  in 3D Euclidean space.

		vertex	line	square	cube
$M_0^{(3)}/a^3$	$V/a^3$	0	0	0	1
$8M_1^{(3)}/a^2$	$S/a^2$	0	0	2	6
$\pi M_2^{(3)}/a$	$B/a$	0	1/2	1	3/2
$4\pi M_3^{(3)}/3$	$\chi$	1	1	1	1

connected black pixels. As in the 2D case, the first step in the calculation of these four numbers is to consider each black pixel as the union of 8 vertices, 12 edges, 6 faces and the interior of the cube. From Eq.(25) and Table IV, or from (34) , it follows that

$$V = n_3 \quad , \quad S = -6n_3 + 2n_2 \quad , \quad 2B = 3n_3 - 2n_2 + n_1 \quad , \quad \chi = -n_3 + n_2 - n_1 + n_0, \quad (40)$$

where  $n_3$  is the number of cubes. Thus, as in the 2D case, the morphological characterization of a 3D pattern reduces to the counting of the elementary geometrical objects (vertices, edges, faces, cubes) that constitute the pattern. For reference, in Table VII we collect some basic results for the normalized Minkowski functionals of simple shapes in 3D Euclidean space.

### 3.2 Computer program

Technically the only real “problem” with the procedure described above is to avoid counting e.g. a face, an edge or vertex more than once. However this problem is easily solved, as illustrated by the algorithm we will briefly discuss now.

In appendix B we list a computer program to compute  $V$ ,  $S$ ,  $B$  and  $\chi$  for a 3D black-and-white pattern. For an example of a program for 2D images see [29]. For some applications, notably those where the patterns are the result of computer simulation, it is useful to adopt periodic boundary conditions. Therefore we present computer code for the case of periodic boundary conditions too. Alternatively one can embed the original image into a larger one, formed by surrounding the original image by one extra layer of pixels. The value of these pixels is determined by making use of the periodic boundary conditions. Then one can use the code that does not explicitly use the boundary conditions.

Conceptually what this program does is to build up the whole image using vertices, edges, etc.. In practice this is accomplished by adding active (= black in the example above) pixels to an initially empty (= white in the example above)

image (held in array `tmp(.)`) one by one. Just before adding the active pixel to the current image (in `tmp(.)`) subroutine “`minko_3D_free`” determines the change in  $V$ ,  $S$ ,  $B$  and  $\chi$  that would result if this pixel is actually added to the current image. This change is calculated by first decomposing this cubic pixel as discussed above and then checking whether e.g. a face overlaps with a face of another active pixel in the current image. Then the pixel is made active in the current image and the changes are added to the current values of  $V$ ,  $S$ ,  $B$  and  $\chi$ . Inspection of “`minko_3D_free`” shows that all it does is check to see if the pixel-to-be-added has active nearest neighbors and/or next-nearest neighbors and count the number of faces, edges and vertices accordingly. Clearly the number of arithmetic operations required to compute  $V$ ,  $S$ ,  $B$  and  $\chi$  scales linearly with the number of pixels of the image. Thus, the numerical procedure is efficient.

### 3.3 Analysis of point patterns

Many systems observed in nature may be modelled by point patterns. For example, a system of particles may be viewed as a collection of points defined by the position of the particles. These points are usually called the *germs* of the model [10, 35]. In order to study the morphological properties of the set of points (degree of randomness, clustering, periodic ordering, ...) it is useful to attach to the points discs (spheres) of radius  $r$ . Those discs (spheres) are called the *grains* of the model [10, 35]. The study of the coverage of the image by the grains gives information about the distribution of the germs.

Mapping the point pattern onto a square (cubic) lattice yields a black-and-white image. Black pixels represent the germs of the model. On the pixel lattice we can construct the grains of the model in two different ways. In the first method we consider the germs to be discs (spheres) of radius  $r = 0$ . We enlarge the discs (spheres) by making black all pixels that are positioned at a distance smaller or equal to  $r > 0$  from the germs. The grains form discrete approximations to discs (spheres) in the Euclidean space. An example of this graining procedure in two dimensions is shown on the left hand side of Fig.8 for grains of radius  $r = 3$ . The right hand side of Fig.8 illustrates the second graining procedure (for  $d = 2$ ), where we take the germs to be squares (cubes) of edge length  $r = 1$  and the grains to be enlarged squares (cubes) of edge length  $r = 2n + 1$ ,  $n > 0$ . Note that the growing of the cubic grains leads to a faster complete coverage of the image than the growing of the circular grains.

For this category of problems MIA consists of the calculation of the three (four) numbers  $U$ ,  $P$ , and  $\chi$  ( $V$ ,  $S$ ,  $B$  and  $\chi$ ) as a function of the grain size  $r$ . A schematic representation of this procedure for the case of 2D point patterns is shown in Fig.9.

### 3.4 Analysis of digitized and thresholded images

In general the intensity (or gray level) in experimental images may be thought of as a continuous function of the position in the image. In order to analyze such images by computer we first have to digitize them [3 – 6]. The digitization process requires the mapping of the image on a grid and a quantization of the gray level. Usually 2D (3D) images are partitioned into square (cubic) regions. Each square (cube) is centered at a lattice point, corresponding to a pixel. In general the range of gray levels is divided into intervals and the gray level at any lattice point is required to take only one of these values.

The output of image analysis should be a description of the given image. Thus we have to define the various objects building up the image, i.e. we need a method to distinguish objects from the background [3, 6]. The simplest method of reducing gray-scale images to two-valued images or black-and-white images is to make use of a *threshold*. If the given image  $\mathcal{P}(\mathbf{x})$  with  $\mathbf{x} \in \mathbb{R}^d$  has gray level range  $[a, b]$ , and  $q$  is any number between  $a$  and  $b$ , the result of thresholding  $\mathcal{P}(\mathbf{x}, q)$  at  $q$  is the two-valued image  $\mathcal{P}(\mathbf{x}, q)$  defined by [3 – 6]

$$\mathcal{P}(\mathbf{x}, q) = \begin{cases} 1 & \mathcal{P}(\mathbf{x}) \geq q \\ 0 & \mathcal{P}(\mathbf{x}) < q \end{cases} . \quad (41)$$

By definition if  $\mathcal{P}(\mathbf{x}, q) = 0$ ,  $\mathbf{x}$  is part of the background, and if  $\mathcal{P}(\mathbf{x}, q) = 1$ ,  $\mathbf{x}$  is part of an object. In practice not all thresholds  $q$  yield useful  $\mathcal{P}(\mathbf{x}, q)$ . If  $q$  is too large too many objects are classified as background or if  $q$  is too small the opposite happens. Other thresholding operations may also be considered [3 – 6].

For this type of image, MIA consists of the calculation of the three (four) numbers  $U$ ,  $P$ , and  $\chi$  ( $V$ ,  $S$ ,  $B$  and  $\chi$ ) as a function of the threshold  $q$ . A schematic representation of this procedure for the case of 2D gray-scale images is shown in Fig.10.

### 3.5 What integral geometry cannot do

Although Hadwiger’s theorem on the completeness of the  $d + 1$  Minkowski functionals is rather powerful, the term “completeness” should not be taken too literally. An almost trivial example may serve to illustrate this point. Consider a triangle in 2D Euclidean space. Can we use the Minkowski functionals to “completely” characterize this triangle? The answer is no. It is not difficult to show that the length of the edges of the triangle are given by

$$a = \frac{P}{4} + \frac{U}{P} \frac{1 + \cos \theta}{\sin \theta} \pm \sqrt{\left(\frac{P}{4} + \frac{U}{P} \frac{1 + \cos \theta}{\sin \theta}\right)^2 - \frac{2U}{\sin \theta}} , \quad (42a)$$



$$b = \frac{P}{4} + \frac{U}{P} \frac{1 + \cos \theta}{\sin \theta} \mp \sqrt{\left(\frac{P}{4} + \frac{U}{P} \frac{1 + \cos \theta}{\sin \theta}\right)^2 - \frac{2U}{\sin \theta}} \quad , \quad (42b)$$

$$c = \frac{P}{2} - \frac{2U}{P} \frac{1 + \cos \theta}{\sin \theta} \quad , \quad (42c)$$

where  $\theta$  denotes the angle between the sides of length  $a$  and  $b$  and  $U$  and  $P$  are the area and perimeter respectively. From (42) it is clear that the Minkowski functionals  $U$ ,  $P$  and  $\chi = 1$  do not specify the triangle completely. Different choices of the angle  $\theta$  results in different triangles with the same area  $U$  and perimeter  $P$ . For MIA to yield useful information about the morphological content of an image, it is necessary to study the dependence of the Minkowski functionals on one or more control parameters (e.g. threshold, grain size, etc.).

### 3.6 Reducing digitization errors

Often the lattice of pixels represents an image of objects in Euclidean space. The Minkowski functionals computed using this lattice approximate the Minkowski functionals in Euclidean space. By digitizing the 2D (3D) image we have introduced square (cubic) distortions in the objects, causing a directional bias. For example digitizing a 2D (3D) image transforms a smooth contour (surface) to a more stepwise contour (surface). The more complicated the image the better the digital approximations are likely to become since the parts of the stepwise boundary or surface will exhibit each orientation more often. The most problematic structures may be isotropic ones.

There are several methods to correct for systematic errors caused by digitization of the image [3, 26]. Many of them can be used to improve the accuracy of the approximations to the area, perimeter, etc. We will not treat problems of digitization here because it is not of fundamental importance for the application of integral-geometry concepts.

### 3.7 Normalization of image functionals

For presentation purposes it is convenient to introduce the following normalized quantities:

$$\tilde{U} = U/L^2, \tilde{P} = P/LN^{1/2}, \tilde{\chi} = \chi/N \quad ; \quad d = 2 \quad , \quad (43a)$$

and

$$\tilde{V} = V/L^3, \tilde{S} = S/L^2N^{1/3}, \tilde{B} = 2B/LN^{2/3}, \tilde{\chi} = \chi/N \quad ; \quad d = 3 \quad , \quad (43b)$$

where  $L$  denotes the linear size of the square (cube) and  $N$  denotes the number of germs.

## 4. Illustrative examples

In this section we apply MIA to point sets and complicated surfaces. These examples serve to illustrate the two basic modes of analysis discussed in sections 3.3 and 3.4. We first apply MIA to simple cubic, face-centered cubic and body-centered cubic lattice structures with and without imperfections. Then we compute the mean value of the Minkowski functionals of random point sets, i.e. the average over all configurations, grain sizes and shapes. Finally we compute the Euler characteristic of a selection of minimal surfaces.

### 4.1 Regular lattices

The face-centered cubic (FCC) and body-centered cubic (BCC) lattices are of great importance, since an enormous variety of solids and several complex fluids [36] crystallize in these forms. The simple cubic (SC) lattice, however, is relatively rare but is often used in theoretical models.

The SC lattice may be generated from the following set of primitive vectors

$$\mathbf{a}_1 = L_0[100] \quad , \quad \mathbf{a}_2 = L_0[010] \quad , \quad \mathbf{a}_3 = L_0[001] \quad , \quad (44)$$

where  $L_0$  denotes the lattice constant. A symmetric set of primitive vectors for the FCC cubic lattice is

$$\mathbf{a}_1 = \frac{L_0}{2}[011] \quad , \quad \mathbf{a}_2 = \frac{L_0}{2}[101] \quad , \quad \mathbf{a}_3 = \frac{L_0}{2}[110] \quad , \quad (45)$$

and for the BCC cubic lattice is

$$\mathbf{a}_1 = \frac{L_0}{2}[11\bar{1}] \quad , \quad \mathbf{a}_2 = \frac{L_0}{2}[1\bar{1}1] \quad , \quad \mathbf{a}_3 = \frac{L_0}{2}[\bar{1}11] \quad . \quad (46)$$

To compute the Minkowski functionals for the SC, FCC, and BCC lattices we imbed these lattices in a cubic lattice with lattice constant one, and make use of (44) - (46) to determine the position of the black pixels. Then we follow the procedure described in section 3.3, to transform the resulting point pattern into a pattern of “spherical” grains of radius  $r$  and to study the behavior of the Minkowski functionals as a function of  $r$ . An example of the graining procedure is shown in Fig.11 for the SC lattice with periodic boundary conditions and  $L_0 = 4$ . The thick solid line indicates the dimensions of the conventional unit cell, simply called the unit cell from now on.

Fig.12 shows the Minkowski functionals  $\tilde{V}$ ,  $\tilde{S}$ ,  $\tilde{B}$  and  $\tilde{\chi}$  as a function of  $r$  for the SC (dotted curve), FCC (solid curve) and BCC (dashed curve) lattice without imperfections. The SC, FCC and BCC lattices with periodic boundaries consist of one unit cell of linear dimension  $L_0 = 32$ . Because of the normalization (43) the

curves for more than one unit cell will be the same as the ones shown in Fig.12. Fig.12 clearly shows that the behavior of the Minkowski functionals as a function of  $r$  differs for the various lattice types. The area  $\tilde{S}$  reaches a maximum if  $r$  equals  $L_0/2$ ,  $L_0\sqrt{2}/4$ ,  $L_0\sqrt{3}/4$ , for the SC, FCC and BCC lattice, respectively. At this value for  $r$  the Euler characteristic  $\tilde{\chi}$  starts to deviate from one because the “spheres” touch each other. For the SC lattice  $\tilde{\chi}$  jumps to -2 independent of  $L_0$  (result not shown). In the case of the FCC (BCC) lattice and for sufficiently large  $L_0$  ( $L_0 \geq 16$ ) the Euler characteristic jumps to a large negative (positive) value. For the SC, FCC and BCC lattice with  $r = 0$  the Euler characteristic per unit cell equals 1, 4 and 2, respectively. This corresponds to the number of “spheres” per unit cell.

Crystal structures formed in materials are not perfect. Therefore it is of interest to study the influence of defects on the curves shown in Fig.12 for the BCC lattice. Imperfections in the crystal structure may be formed by the absence or by small displacements of some of the basic lattice points. Also the presence of impurities, creating extra lattice points, causes an imperfect crystal structure. In Fig.13 we show the Minkowski functionals as a function of  $r$  for perfect and imperfect BCC lattice structures. The solid curve depicts the data for a perfect BCC lattice containing  $M = 8$  unit cells of linear dimension  $L_0 = 16$ . The dashed curve shows the data for the same BCC lattice to which  $\pm 30\%$  of defects have been added at randomly chosen positions. The dotted curve depicts the results of displacing  $\pm 30\%$  randomly chosen basic lattice points over a random distance 0 or 1. Apart from some minor changes the three curves behave in the same way. Only if we move all the lattice points over a random distance 0 or 1 (dash-dotted lines), the curves for  $\tilde{B}$  and  $\tilde{\chi}$  differ qualitatively from the ones of the perfect BCC lattice. Therefore we may conclude that the presence of small amounts of defects in the crystal structure does not alter the characteristic behavior of the Minkowski functionals as a function of  $r$ .

An appealing feature of MIA is that it is capable of distinguishing different lattice types even if the amount of lattice points is relatively small. MIA is not very sensitive to finite size effects [33].

## 4.2 Dislocations

Dislocations comprise an important class of defects because they are the basic carriers of plasticity in crystalline material. This is even so, to a rather great extent, for quasi-crystalline and even non-crystalline solid material that can be described in terms of a network of disclinations, i.e. groups of dislocations, ordered and disordered, respectively. In a well-annealed crystal the dislocation density, defined as the total length of dislocations per unit volume, is usually between  $10^9$  and  $10^{12}\text{m}^{-2}$  [37]. Dislocations represent discontinuities in displacements and they can

also be used to describe, at least in a mathematical sense, a macroscopic static crack. As such the dislocation can be considered to be the basic building block of a crack. This idea that a crack can be thought of as an array of discrete coplanar and parallel dislocations was introduced by Eshelby, Frank and Nabarro [38], and by Leibfried [39]. For dislocation based fracture mechanics references are made to Lardner's book [40] and to the recently published excellent text by Weertman [41].

The two simplest kinds of dislocations are the edge and screw dislocations [42]. An edge dislocation can be considered by inserting an extra half plane of atoms into the lattice. The edge of the extra half plane of atoms is called the dislocation line. The presence of a screw dislocation in the crystal transforms the crystal planes into a helicoidal surface, i.e. the atom planes perpendicular to the dislocation line are turned into a spiral ramp.

The atoms in a crystal containing a dislocation are displaced from their perfect lattice positions. If a complete circuit is made around a dislocation line, the displacement of the end point must differ from the displacement of the starting point by the length of the Burgers vector  $\mathbf{b}$ . In the case of a screw dislocation the Burgers vector is parallel to the dislocation line. The Burgers vector of an edge dislocation is perpendicular to the dislocation line. The slip plane is uniquely defined as the plane that contains both the dislocation line and the Burgers vector [42]. The glide of an edge dislocation is therefore limited to a specific plane. However, the dislocation line and the Burgers vector of a screw dislocation do not define a unique plane and hence the glide of the dislocation is not restricted to a specific plane. Movement of the screw dislocation produces a displacement parallel to the dislocation line.

In what follows we orient the coordinate system such that the  $z$ -axis coincides with the dislocation line. The  $y$ -axis is chosen to be perpendicular to the slip plane, the plane on which a dislocation line glides. Hence for a screw dislocation the Burgers vector determines the position of the  $z$ -axis and for an edge dislocation it fixes the  $x$ -axis.

In the case of a screw dislocation there are no displacements in the  $x$ - and  $y$ -direction ( $u_x = u_y = 0$ ). The dislocation in the  $z$ -direction increases uniformly from zero to  $b \equiv |\mathbf{b}|$  and for the dislocation in an isotropic linear elastic medium the displacement reads [42]

$$u_z = \frac{b}{2\pi} \tan^{-1} \frac{y}{x} \quad , \quad (47)$$

where  $b$  is the magnitude of the Burgers vector of the dislocation.

For an edge dislocation the displacements are given by [42]

$$u_x = \frac{b}{2\pi} \left[ \tan^{-1} \frac{y}{x} + \frac{xy}{2(1-\nu)(x^2 + y^2)} \right]$$

$$\begin{aligned}
u_y &= -\frac{b}{2\pi} \left[ \frac{1-2\nu}{4(1-\nu)} \ln(x^2 + y^2) + \frac{x^2 - y^2}{4(1-\nu)(x^2 + y^2)} \right] \\
u_z &= 0 \quad ,
\end{aligned} \tag{48}$$

where  $\nu$  denotes Poisson's ratio. Typical values of  $\nu$  for metallic and ceramic solids lie in the range 0.2–0.45 [42]. The displacement fields of Eqs.(47) and (48) describe the fields of stationary dislocations that are affected by the velocity of a moving dislocation in a drag-controlled regime [43, 44, 45].

Possible Burgers vectors are determined by the crystallographic structure of the crystal. A dislocation whose Burgers vector is a lattice translation vector is known as a perfect dislocation [42]. We only consider Burgers vectors that are the shortest lattice translation vectors on the characteristic slip planes. For the FCC lattice it is observed experimentally that slip takes place on the  $\{111\}$  planes along the  $\langle 110 \rangle$  directions [42]. We choose the Burgers vector to point along the  $[110]$  direction. Thus the smallest possible Burgers vector of a perfect dislocation is  $\mathbf{b} = [110]L_0/2$  with length  $b = L_0/\sqrt{2}$ . For the BCC lattice the smallest possible Burgers vector of a perfect dislocation is  $\mathbf{b} = [111]L_0/2$  with length  $b = \sqrt{3}L_0/2$  [42]. Experimentally slip has been observed on the  $\{110\}$ ,  $\{112\}$  and  $\{123\}$  planes [42]. We consider as slip planes the  $\{110\}$  planes, which are the most densely packed.

To compute the Minkowski functionals for the FCC and BCC lattices with a screw or edge dislocation we first create a perfect FCC and BCC lattice by imbedding these lattices in a cubic lattice with lattice constant one and use (44) - (46) to determine the positions of the black pixels. For the four different cases we rotate the coordinate system such that

$$\begin{aligned}
\text{FCC, screw} &: z = [100], y = [\bar{1}11], x = y \times z = [\bar{1}1\bar{2}] \\
\text{BCC, screw} &: z = [111], y = [\bar{1}10], x = y \times z = [11\bar{2}] \\
\text{FCC, edge} &: x = [110], y = [\bar{1}11], z = x \times y = [1\bar{1}2] \\
\text{BCC, edge} &: x = [111], y = [\bar{1}10], z = x \times y = [\bar{1}\bar{1}2] \quad ,
\end{aligned} \tag{49}$$

and we compute the atom displacements using Eqs. (47) and (48). Then we rotate back to the original  $(x, y, z)$  coordinate system. Finally we follow the procedure described in section 3.3 to transform the resulting point pattern into a pattern of "spherical" grains of radius  $r$  or cubic grains of edge length  $r$ , and study the behavior of the Minkowski functionals as a function of  $r$ . For the computation of the Minkowski functionals we make use of free boundary conditions.

The results for  $\tilde{V}$ ,  $\tilde{S}$  and  $\tilde{B}$  for FCC and BCC crystals containing screw or edge dislocations only differ very little from the results for the perfect crystal structures. Therefore we only present the results for  $\tilde{\chi}$ . Fig.14 depicts the Euler characteristic for a perfect FCC lattice (Fig.14a,d), an FCC lattice with a screw dislocation in the centre (Fig.14b,e) and an FCC lattice with an edge dislocation located at the

crystal centre (Fig.14c,f). The FCC lattice contains  $M = 5$  unit cells of linear dimension  $L_0 = 16$ . In Fig.14a,b,c the grains are spheres and in Fig.14d,e,f the grains are cubes. Similar results for the BCC lattice are shown in Fig.15. As seen from Figs.14,15 the Euler characteristics as a function of  $r$  for the FCC and BCC lattices show a completely different behavior, independent of the choice of the shape of the grains. This was already concluded from Fig.12 where spherical grains and periodic boundaries were used. Fig.14 shows that using spherical grains to study the Euler characteristic as a function of  $r$  makes it difficult to detect a dislocation in an FCC lattice. Only very small changes in the curve for the Euler characteristic are seen (except for the change in the amplitudes of the peaks). Using cubic grain instead of spherical grains gives a clear signature of the presence of a dislocation in  $\tilde{\chi}$ . However, the distinction between a screw and an edge dislocation is not clear. For the BCC lattice it is better to use spherical than cubic grains to detect dislocations in the crystal, as seen from Fig.15. Also for the BCC lattice it is not easy to distinguish between an edge and a screw dislocation.

If we increase the number of unit cells in the crystal the signature of the dislocation in the Euler characteristic weakens (results not shown). This is due to the large contribution from the perfect lattice part to  $\tilde{\chi}$  compared to the contribution from the part of the crystal containing the dislocation. Hence, for large crystal structures local measurements of the Euler characteristic are necessary to detect dislocations.

### 4.3 Random point sets

We consider a collection of  $N$  points  $p_i$ , with positions generated from a uniformly uncorrelated random distribution, in a convex domain  $\tilde{\Omega} \subset \mathbb{R}^d$  of Euclidean space. The mean density of points equals  $\rho = N/\Omega$ , where  $\Omega$  denotes the volume of  $\tilde{\Omega}$ . We attach to every point  $p_i$  (germ) a grain  $A_i \in \mathcal{R}$ , where  $\mathcal{R}$  denotes the convex ring, the class of all subsets  $A$  of  $\mathbb{R}^d$  which can be expressed as finite unions of compact convex sets (see section 2.5). A configuration of the grains  $A_i$  gives rise to a set  $\mathcal{A}_N \in \mathcal{R}$

$$\mathcal{A}_N = \bigcup_{i=1}^N s_i A_i \quad , \quad (50)$$

where  $s_i \in \mathcal{S}$ , under the assumption that the translations are restricted to  $\tilde{\Omega}$ . Here  $\mathcal{S}$  denotes the group of all symmetry operations in  $\mathbb{R}^d$ . This random distribution of grains includes the Boolean model [35], a basic model in stereology and stochastic geometry [9, 10]. A nice feature of this model is that the configurational average of the Minkowski functionals of  $\mathcal{A}_N$  can be calculated analytically [11, 29, 46, 47]. This is useful to assess the validity of numerical calculations.

We first consider the case of Euclidean space. In the bulk limit  $N, \Omega \rightarrow \infty$ ,  $\rho = N/\Omega$  fixed, the closed form expressions for the configurational averages  $\langle M_\nu/N \rangle_N$ ,  $\nu = 0, \dots, d$  are known exactly [11, 29, 46, 47] and are given by

$$\langle M_0/N \rangle_N = (1 - e^{-\rho m_0}) / \rho \quad , \quad (51a)$$

$$\langle M_1/N \rangle_N = m_1 e^{-\rho m_0} \quad , \quad (51b)$$

$$\langle M_2/N \rangle_N = (m_2 - m_1^2 \rho) e^{-\rho m_0} \quad , \quad (51c)$$

$$\langle M_3/N \rangle_N = (m_3 - 3m_1 m_2 \rho + m_1^3 \rho^2) e^{-\rho m_0} \quad , \quad (51d)$$

where we introduced the notation  $M_\nu \equiv M_\nu^{(d)}$ ,  $\langle M_\nu \rangle_N$  denote the configurational average of the Minkowski functionals over realisations with density  $\rho$  and  $m_\nu$  denote the mean values of the Minkowski functionals of a single grain.

In 2D Euclidean space (51) reduces to

$$\langle \tilde{U}(\rho) \rangle = (1 - e^{-\rho u}) \quad , \quad (52a)$$

$$\langle \tilde{P}(\rho) \rangle = p \rho^{1/2} e^{-\rho u} \quad , \quad (52b)$$

$$\langle \tilde{\chi}(\rho) \rangle = \left( 1 - \frac{1}{4\pi} p^2 \rho \right) e^{-\rho u} \quad , \quad (52c)$$

where  $u$  and  $p$  denote the mean values of the area and perimeter of a single grain. Note that in 2D (51d) has no meaning. The Euler characteristic of a single grain equals one.

In 3D Euclidean space we find

$$\langle \tilde{V}(\rho) \rangle = (1 - e^{-\rho v}) \quad , \quad (53a)$$

$$\langle \tilde{S}(\rho) \rangle = s \rho^{2/3} e^{-\rho v} \quad , \quad (53b)$$

$$\langle \tilde{B}(\rho) \rangle = 2b \rho^{1/3} \left( 1 - \frac{\pi}{64} \frac{s^2}{b} \rho \right) e^{-\rho v} \quad , \quad (53c)$$

$$\langle \tilde{\chi}(\rho) \rangle = \left( 1 - \frac{1}{2} s b \rho + \frac{\pi}{384} s^3 \rho^2 \right) e^{-\rho v} \quad , \quad (53d)$$

where the mean values of the volume, area and mean breadth of a single grain are denoted by  $v$ ,  $s$  and  $b$  respectively. The Euler characteristic of a single grain equals one.

The mean values of the Minkowski functionals depend on the (averaged) shape of the single grains. For instance, in the 2D case where the (averaged) grains are circular discs of radius  $r$ ,  $u = \pi r^2$  and  $p = 2\pi r$ . If the (averaged) grains are spheres of radius  $r$  we employ (53) with  $v = 4\pi r^3/3$ ,  $s = 4\pi r^2$  and  $b = 2r$ . In the latter case we obtain

$$\langle \tilde{V} \rangle = 1 - e^{-n} \quad , \quad (54a)$$

$$\langle \tilde{S} \rangle = 4\pi\rho^{2/3}r^2 e^{-n} \quad , \quad (54b)$$

$$\langle \tilde{B} \rangle = 4\rho^{1/3}r \left( 1 - \frac{3\pi^2}{32}n \right) e^{-n} \quad , \quad (54c)$$

$$\langle \tilde{\chi} \rangle = \left( 1 - 3n + \frac{3\pi^2}{32}n^2 \right) e^{-n} \quad , \quad (54d)$$

with  $n = 4\pi r^3 \rho / 3$ .

We adopt the procedure outlined in section 3.3 to compute the morphological properties of a uniform random distribution of points in a cube of edge length  $L$ , subject to periodic boundaries. In Fig.16 we depict the Minkowski functionals as a function of  $r$  for two random point sets with  $L = 128$  and different density. The solid (dashed) lines show the data for  $N = 1024$  ( $N = 512$ ). For both cases the behavior of the Minkowski functionals as a function of  $r$  is very similar: The curves show the same qualitative behavior (the grains have the same shape in both cases) and are only shifted with respect to each other. Results (not shown) for various other system sizes and densities show similar, minor quantitative differences. For small  $r$  the grains are isolated leading to a small covered volume and surface area and to a positive Euler characteristic. For large  $r$  the grains largely overlap and cover almost completely the whole cube. Only small cavities remain. This gives rise to a large covered volume, a small surface area and a positive Euler characteristic which approaches zero in the case of the completely covered cube. For intermediate  $r$  the coverage has a tunnel-like structure with a negative Euler characteristic and a large surface area.

The dash-dotted ( $N = 1024$ ) and dotted ( $N = 512$ ) lines in Fig.16 are the results obtained by fitting

$$\langle \tilde{V}_F \rangle = 1 - e^{-n} \quad , \quad (55a)$$

$$\langle \tilde{S}_F \rangle = s\rho^{2/3}e^{-n} \quad , \quad (55b)$$

$$\langle \tilde{B}_F \rangle = 2 \left( b - \frac{\pi\rho s^2}{64} \right) \rho^{1/3} e^{-n} \quad , \quad (55c)$$

$$\langle \tilde{\chi}_F \rangle = \left( 1 - \frac{\rho s b}{2} f_4 + \frac{\pi\rho^2 s^3}{384} f_5 \right) e^{-n} \quad , \quad (55d)$$

to the data with  $n = 4\pi\rho f_1 r^3 / 3$ ,  $s = 4\pi f_2 r^2$  and  $b = 2f_3 r$ . The functional behavior of  $\tilde{V}_F$ ,  $\tilde{S}_F$ ,  $\tilde{B}_F$  and  $\tilde{\chi}_F$  is chosen to be the same as for perfect spherical grains in the Euclidean space (see (54)). The fitting parameters  $f_1, \dots, f_5$  have been introduced to take into account that in practice we are working on a lattice and are approximating spheres by discrete structures. We find for  $N = 512$  and  $N = 1024$ ,  $f_1 = 0.108$ ,  $f_2 = 0.32$ ,  $f_3 = 0.8$ ,  $f_4 = 0.72$  and  $f_5 = 0.77$  for the dash-dotted



(dotted) line by fitting the solid (dashed) line. The Minkowski functionals of random point sets generically display the behavior shown in Fig.16. In general the fitting parameters  $f_i$  considerably deviate from their Euclidian value ( $f_i = 1$ ). Clearly the use of a lattice introduces some artifacts which after all is not unexpected. Recall that some of these artifacts will remain if we use a finer mesh [29].

On a regular  $d$ -dimensional lattice it may be more natural to work with hypercubes instead of digital approximations of the corresponding Euclidean shapes. This suggests the use of integral geometry on a lattice (see Sections 2.8 and 2.9). Thus, we consider a collection of  $N$  pixels  $p_i$  in a hypercubic domain  $Z \subset \mathbb{Z}^d$  of volume  $|Z| = L^d$ . The positions of the pixels are generated from a uniformly uncorrelated random distribution. The mean density of pixels equals  $\rho = N/|Z|$ . As before we attach to every germ  $p_i$  a hypercubic grain  $C_i$ . In appendices D and E we give a derivation of the lattice equivalent of (51) by making use of the kinematic formulae (27) and (36), respectively. Our derivation differs from the one given in [11] in the sense that it uses another technique and is valid for small systems too.

In the bulk limit  $N, |Z| \rightarrow \infty$  with  $\rho$  fixed, the averaged Minkowski functionals  $V_\nu \equiv V_\nu^{(d)}$  of random configurations of grains on a lattice are given by

$$\begin{aligned} \left\langle \frac{V_0}{N} \right\rangle_N &= (1 - e^{-\rho v_0})/\rho \\ \left\langle \frac{V_1}{N} \right\rangle_N &= e^{-\rho v_0} (1 - e^{-\rho v_1})/\rho \\ \left\langle \frac{V_2}{N} \right\rangle_N &= -e^{-\rho v_0} (1 - 2e^{-\rho v_1} + e^{-\rho(2v_1+v_2)})/\rho \\ \left\langle \frac{V_3}{N} \right\rangle_N &= e^{-\rho v_0} (1 - 3e^{-\rho v_1} + 3e^{-\rho(2v_1+v_2)} - e^{-\rho(3v_1+3v_2+v_3)})/\rho \quad , \end{aligned} \quad (56)$$

where  $v_\nu$  denote the mean values of  $V_\nu$  for one single grain. Analogously, in the bulk limit  $N, |Z| \rightarrow \infty$  with  $\rho$  fixed, the averaged functionals  $F_\nu$  of random configurations of grains on a lattice are given by

$$\left\langle \frac{F_\nu}{N} \right\rangle_N = \binom{d}{\nu} \left[ 1 - \exp \left( -\rho f_\nu \binom{d}{\nu}^{-1} \right) \right] / \rho \quad ; \quad \nu = 0, \dots, d \quad , \quad (57)$$

where  $f_\nu$  denote the mean values of  $F_\nu$  for one single grain. Rewriting formulae (56) and (57) in terms of the morphological functionals  $U, P, \chi$  for two dimensions and  $V, S, B, \chi$  for three dimensions and specializing to (averaged) square and cubic grains so that  $v_\nu = r^{d-\nu}$  and  $f_\nu = \binom{d}{\nu} r^\nu (r+1)^{d-\nu}$  for  $\nu = 0, \dots, d$ , we have

$$\langle \tilde{U} \rangle = 1 - e^{-\rho r^2} \quad , \quad (58a)$$

$$\langle \tilde{P} \rangle = 4e^{-\rho r^2} (1 - e^{-\rho r})/\rho^{1/2} \quad , \quad (58b)$$

$$\langle \tilde{\chi} \rangle = e^{-\rho r^2} (-1 + 2e^{-\rho r} - e^{-\rho(2r+1)})/\rho \quad , \quad (58c)$$

for the case of a 2D lattice and

$$\langle \tilde{V} \rangle = 1 - e^{-\rho r^3} \quad , \quad (59a)$$

$$\langle \tilde{S} \rangle = 6e^{-\rho r^3} (1 - e^{-\rho r^2}) / \rho^{1/3} \quad , \quad (59b)$$

$$\langle \tilde{B} \rangle = 3e^{-\rho r^3} (-1 + 2e^{-\rho r^2} - e^{-\rho(2r^2+r)}) / \rho^{2/3} \quad , \quad (59c)$$

$$\langle \tilde{\chi} \rangle = e^{-\rho r^3} (1 - 3e^{-\rho r^2} + 3e^{-\rho(2r^2+r)} - e^{-\rho(3r^2+3r+1)}) / \rho \quad , \quad (59d)$$

for the 3D lattice. In (58) and (59) the linear size of the (averaged) square and cubic grain is denoted by  $r$ . Note that  $r$  is a positive integer.

In Figs.17(18) we show the Minkowski functionals for one realization of a 2D (3D) random points set. Square (cubic) grains were used to compute the Minkowski functionals. The linear size of the system  $L = 128$  and the number of points  $N = 1024$ . The solid lines are the results obtained from (58) and (59). There is excellent agreement between the numerical data and the theoretical results. Note that there is no need to use adjustable parameters if we adopt the lattice version of integral geometry.

#### 4.4 Topology of triply periodic minimal surfaces

A *minimal surface* in  $\mathbb{R}^3$  is defined as a surface  $\partial\mathcal{P}$  for which the mean curvature  $H = (1/R_1 + 1/R_2)/2$  is zero at each of its points, where  $R_1$  and  $R_2$  are the two principal radii of curvature. Hence the Gaussian curvature  $G = 1/R_1 R_2$  is always non-positive. For every closed circuit on the surface, the area is a minimum. We will consider the triply periodic minimal surfaces (TPMS), minimal surfaces that are periodic in three independent directions. Structures related to TPMS may form spontaneously in physico-chemical and in biological systems [2, 48]. Examples may be found in various crystal structures [2, 49–53], lipid-containing systems [54–59], polymers [60–75], skeletal elements in sea urchins [76, 77] and cell membranes [78]. Recently TPMS became also of interest in the analysis of the relations between the geometry and topology of the surface and surface diffusion [79–81].

A TPMS is either free of self-intersections or may intersect itself in a more or less complicated way. Each TPMS without self-intersections is two-sided and subdivides  $\mathbb{R}^3$  into two infinite, connected but disjoint regions. These two regions, or labyrinths, are not simply connected. They interpenetrate each other in a complicated way. The two labyrinths may differ in shape or they may be congruent, i.e. there exist symmetry operations mapping one labyrinth onto the other. In the latter case the surface is called a *balance surface* [82]. Balance surfaces divide space into two labyrinths with equal volume fractions. The symmetry of a balance surface is described by a group-subgroup pair  $\mathcal{H}/\mathcal{I}$  of spacegroups, where  $\mathcal{H}$  contains all isometries of  $\mathbb{R}^3$  which map the surface onto itself. An isometry of  $\mathcal{H}$  maps each side of the surface and each labyrinth either onto itself or onto the other side and

the other labyrinth [82].  $\mathcal{I}$  contains only those isometries which map each side of the surface and each labyrinth onto itself. If the two sides of a balance surface are “colored” so that they are symmetrically distinct, black-white space groups instead of the group-subgroup pairs with index 2 may be used to describe its symmetry [82]. In this case the surface is called oriented. Nonbalance surfaces have  $\mathcal{I} \equiv \mathcal{H}$  and divide space into two labyrinths with unequal volume fractions.

The topology of a TPMS can be characterized by means of the Euler characteristic  $\chi$  which is related to the genus  $g$  of the surface by means of  $g = 1 - \chi(\partial\mathcal{P})/2$  (see section 2.6). A finite surface of genus  $g$  is the topological equivalent of a sphere with  $g$  handles. In this sense a TPMS has an infinite Euler characteristic and genus. Therefore, to characterize the topology of a TPMS the genus and Euler characteristic are calculated per unit cell. There are two common choices of unit cells, the lattice fundamental region and the crystallographic cell [83]. The lattice fundamental region contains the smallest region of the surface that reproduces the complete surface upon translation of this unit cell alone. The crystallographic cell is the smallest cube generating space by the lattice and can contain many lattice fundamental regions. We give our data for the crystallographic cell, simply called the unit cell from now on.

The topology of a TPMS can be determined in different ways: (1) by means of the genus calculated by making use of the labyrinth graphs [84, 85], (2) by means of the Euler characteristic determined with the aid of any tiling on the surface [86], (3) by means of the genus computed making use of the flat points of the surface [85], (4) by means of the simplex decomposition method [87], (5) by means of the Euler characteristic obtained with MIA. In previous work we analyzed the topology (via the computation of the Euler characteristic) and the geometry of the P (primitive), the D (double diamond) and the G (gyroid) surfaces [84, 88] by means of integral-geometry-based MIA [29, 89].

Here we use the same method to characterize in addition the topology of the minimal balance surfaces S [82], C(P) [90], C(Y) [82],  $^{\pm}Y$  [82],  $C(^{\pm}Y)$  [91] and the minimal nonbalance surfaces I-WP [84] and F-RD [84]. These structures serve as a good test case for integral-geometry-based MIA because compared to the P, D and G surfaces these minimal surfaces typically have a more complicated structure per unit cell.

TPMS, as well as other periodic surfaces, such as equipotential (and zero potential) and Fermi surfaces, can be approximated by periodic *nodal surfaces* [49, 52, 92–94]. These can be obtained from the roots of the series

$$\sum_{hkl} |F(hkl)| \cos(2\pi(hx + ky + lz) - \alpha_{hkl}) = 0 \quad , \quad (60)$$

where  $\alpha_{hkl}$  and  $F(hkl)$  denote a phase shift and the structure factor, respectively. Truncating the series to the leading term determines the principal nodal surfaces

of a given symmetry [94]. The nodal P surface is given by

$$\cos X + \cos Y + \cos Z = 0 \quad , \quad (61)$$

where  $X = 2\pi x/L_0$ ,  $Y = 2\pi y/L_0$ ,  $Z = 2\pi z/L_0$  and  $L_0$  denotes the length of the crystallographic unit cell. The nodal primitive P surface is shown in Fig.19 together with the nodal double diamond D surface. The latter is defined by

$$\sin X \sin Y \sin Z + \sin X \cos Y \cos Z + \cos X \sin Y \cos Z + \cos X \cos Y \sin Z = 0 \quad . \quad (62)$$

The nodal gyroid surface is shown in Fig.20 and is defined by

$$\sin X \cos Y + \sin Y \cos Z + \cos X \sin Z = 0 \quad . \quad (63)$$

Fig.20 also shows the nodal S surface given by

$$\cos 2X \sin Y \cos Z + \cos X \cos 2Y \sin Z + \sin X \cos Y \cos 2Z = 0 \quad . \quad (64)$$

The nodal Neovius surface C(P) and the nodal C(Y) surface are depicted in Fig.21. Their representations read

$$\cos X + \cos Y + \cos Z + 4 \cos X \cos Y \cos Z = 0 \quad , \quad (65)$$

and

$$\begin{aligned} & -\sin X \sin Y \sin Z + \sin 2X \sin Y + \sin 2Y \sin Z + \sin X \sin 2Z \\ & -\cos X \cos Y \cos Z + \sin 2X \cos Z + \cos X \sin 2Y + \cos Y \sin 2Z = 0 \quad , \quad (66) \end{aligned}$$

respectively. The nodal  $\pm Y$  surface is given by

$$2 \cos X \cos Y \cos Z + \sin 2X \sin Y + \sin X \sin 2Z + \sin 2Y \sin Z = 0 \quad , \quad (67)$$

and is shown in Fig.22 together with the nodal surface for its complementary surface  $C(\pm Y)$  which is given by

$$-2 \cos X \cos Y \cos Z + \sin 2X \sin Y + \sin X \sin 2Z + \sin 2Y \sin Z = 0 \quad . \quad (68)$$

Finally, the minimal nonbalance surfaces I-WP and F-RD are depicted in Fig.23. They are represented by

$$2(\cos X \cos Y + \cos Y \cos Z + \cos X \cos Z) - \cos 2X - \cos 2Y - \cos 2Z = 0 \quad , \quad (69)$$

and

$$4 \cos X \cos Y \cos Z - \cos 2X \cos 2Y - \cos 2Y \cos 2Z - \cos 2X \cos 2Z = 0 \quad , \quad (70)$$

respectively.

It is known that the properties of the nodal approximations can differ considerably from those of real TPMS [53]. The quality of the nodal approximation depends on the number of terms in the Fourier series and varies considerably for different structures [95, 96].

Table.VIII Minimal surfaces, group-subgroup pairs  $\mathcal{H}$ - $\mathcal{I}$  and the Euler characteristic.  $\chi^{(a)}(\partial\mathcal{P})$  denotes the Euler characteristic per lattice fundamental region of the minimal surfaces obtained by means of labyrinth graphs and surface tilings [86],  $\chi^{(b)}(\partial\mathcal{P})$  denotes the Euler characteristic per unit cell of the nodal approximations calculated by triangulating the surface with the marching cube algorithm [95],  $\chi^{MIA}(\partial\mathcal{P}) = 2\chi^{MIA}(\mathcal{P})$  denotes the Euler characteristic per unit cell of the nodal approximations as obtained by means of the integral-geometry-based MIA.

Minimal surface	$\mathcal{H}$	$\mathcal{I}$	$\chi^{(a)}(\partial\mathcal{P})$	$\chi^{(b)}(\partial\mathcal{P})$	$\chi^{MIA}(\partial\mathcal{P})$
P	$Im\bar{3}m$	$Pm\bar{3}m$	-4	-4	-4
D	$Pn\bar{3}m$	$Fd\bar{3}m$	-4	-16	-16
G	$Ia\bar{3}d$	$I4_132$	-4	-8	-8
S	$Ia\bar{3}d$	$I43d$	-20	-40	-40
C(P)	$Im\bar{3}m$	$Pm\bar{3}m$	-16	-16	-16
C(Y)	$I4_132$	$P4_332$	-24	-24	-24
$\pm Y$	$Ia\bar{3}$	$Pa\bar{3}$	-40	-	-40
C( $\pm Y$ )	$Ia\bar{3}$	$Pa\bar{3}$	-24	-	-24
I-WP	$Im\bar{3}m$	$Im\bar{3}m$	-6	-12	-12
F-RD	$Fm\bar{3}m$	$Fm\bar{3}m$	-10	-40	-40

Table VIII gives our results for the Euler characteristic of the nodal surfaces for one unit cell of length  $L_0 = 128$  together with the numbers found in literature [86, 95]. As seen from Table VIII the values calculated using the integral-geometry approach are in good agreement with the numbers found in literature.

In conclusion, integral-geometry-based MIA is a convenient tool to study the topology of challenging surfaces such as some TPMS. In particular, to study the topology of the TPMS, MIA does not require the use of labyrinth graphs or surface tilings [86].

## 5. Computer tomography images of metal foams

Metal foams have recently become a popular topic of research interest in the

materials science community although these materials have existed for over almost fifty years [97]. At present metal foams containing up to 95% porosity are being explored for applications that require a high specific stiffness and strength, high mechanical energy absorption and for heat exchangers [98]. Various studies on open-cell foams have shown that both the stiffness and the strength are dominated by bending, the former of which scales with  $\rho^2$  and the latter with  $\rho^{3/2}$  (with  $\rho$  the relative density) [99]. In Fig.24 the bending of a strut in an open-cell foam (Duocel) at an early and a later stage is shown as observed by in-situ tensile experiments in a Philips-XL30-FEG-ESEM. The mechanical response of closed-cell foams is more complicated because the deformation of the cell faces, as well as the edges must be included to give a complete description. In metallic foams both size effects [100] and topology play a crucial role. However, only a few studies are devoted to investigate topological criteria that control the deformation mechanism by analyzing the rigidity of frameworks comprising of inextensional struts [101]. The commercially available metal foams have random microstructures but also microstructures of periodic architectures can be constructed with topologies that lead to properties superior to their stochastic analogues [102].

For materials scientists it is of interest to investigate the topology of the metal foams without destroying the sample. Using a computer tomograph (CT) scanner makes it possible to visualize the interior of a foam in a non-destructive manner and to produce a 3D image of the sample.

Information about the morphological properties of the foams can be obtained from the computation of the Minkowski functionals for the 3D CT images. In this section we first explain how we calculate the 3D Minkowski functionals from the CT images. Then we apply the technique to two aluminium foam samples of a different type. We demonstrate that using the morphological image analysis technique to analyse the 3D CT images gives information about the morphological properties of the foam and might be used to classify the metal foams.

### *5.1 Computation of 3D Minkowski functionals*

High resolution CT scanners can produce huge data sets of 2D slices (of typically 1Mb each). These 2D slices are used to reconstruct the 3D image [3]. Our 3D images are cubes cut out from the complete CT image. Before we compute the Minkowski functionals we first set a threshold to the 3D image. The program to calculate the Minkowski functionals for the 3D images always holds four slices in memory at a time. Basically we use the same method and program as discussed in section 3.2 and appendix B, i.e. we add active (black) pixels to an initially empty (white) image one by one. Before we add the pixel we check if the pixel-to-be-added has active nearest neighbors and/or next-nearest neighbors and count the number of faces, edges and vertices accordingly. At the onset of the computation the first

three slices are completely empty (all pixels are white) and the fourth slice contains the pixels of the first slice of the CT scan. We remove the pixels from the fourth slice (one by one, from left to right and from front to back) and add them to the second slice after checking its nearest neighbors and/or next nearest neighbors in all directions (bottom direction is first slice and top direction is third slice) and counting the number of faces, edges and vertices. We calculate the changes to  $V$ ,  $S$ ,  $B$  and  $\chi$  and proceed. If the fourth slice is emptied we make a copy of the second slice in the first slice and load the second CT slice in the fourth slice. We now proceed in the same way as for the first step. We continue until all CT slices are processed. The number of arithmetic operations required to calculate the Minkowski functionals scales linearly with the number of active pixels in the image. The memory needed equals four times the memory required to store one CT slice.

The computational and memory demands can be slightly reduced. The method described above uses the program given in appendix B. This program is written for more general applications than the one we need here. The program can handle the situation in which we remove one pixel from an image of which we already calculated the Minkowski functionals and compute the change in the Minkowski functionals. This requires the check of all nearest and next-nearest neighbors (26 in total). In the CT case we build up the image by adding pixel by pixel. Then only half of the neighbors need to be checked. Moreover, only storage for three slices is required.

The procedure to calculate the Minkowski functionals in this more economic way is as follows. At startup of the computation the first two slices are completely empty (all pixels are white) and the third slice contains the pixels of the first slice of the CT scan. We remove the pixels from the third slice (one by one, from left to right and from front to back) and add them to the second slice after checking its nearest neighbors and/or next nearest neighbors to the left, front and bottom (first slice) and counting the number of faces, edges and vertices. We calculate the changes to  $V$ ,  $S$ ,  $B$  and  $\chi$  and proceed. If the third slice is emptied we make a copy of the second slice in the first slice and load the second CT slice in the third slice. We now proceed in the same way as for the first step. We continue until all CT slices are processed.

## 5.2 Aluminium foams with closed-cell and open-cell structure

An example of a 2D CT image of a closed-cell (left) and open-cell (right) aluminium foam is shown in Fig.25. We used hundreds of these 2D slices to reconstruct the 3D image of a closed-cell and open-cell aluminium foam. Fig.26 shows the 3D images of the two different aluminium foam samples. The image on the left corresponds to a closed-cell foam and the one on the right to a foam with a more open structure. In order to study the Minkowski functionals for these aluminium foams we first put a threshold to the cubic image. For the given images only very small thresholds are relevant. Considering medium to large thresholds ( $q > 50$ ) leads to loose parts and completely disconnected structures in the image. For these large thresholds the resulting image no longer resembles the real foam structure.

In Fig.27 and Fig.28 we depict the Minkowski functionals as a function of the threshold  $q$  for the closed-cell and open-cell structure, respectively. For the analysis of the foam structures we only consider  $0 < q < 50$  because for larger  $q$  the image is almost completely empty. The covered volume for the closed-cell foam is much larger (four times) than the covered volume for the foam with the more open structure. The surface areas of the coverages show a similar feature. This suggests that in the aluminium foam with open structure, large open structures (cavities and tunnels) filled with air are present and that the closed-cell aluminium foam contains many small cavities and tunnels filled with air. This can also be seen from the structure images in Fig.26. For the open-cell aluminium foam the mean breadth is positive and rather constant for  $0 < q < 50$ . In the case of the closed-cell foam the mean breadth changes from negative to positive values for  $0 < q < 50$ . This indicates that in the closed-cell foam more tunnels are present. For both foams the Euler characteristic is negative which means that on the average the surface is hyperbolic and contains a lot of tunnels. For the foam with the closed-cell structure the Euler characteristic is much more negative than the Euler characteristic for the foam with the more open structure. The more negative  $\chi$  becomes, the more tunnels in the structure and the more complex the structure is [103].

The analysis of the 3D Minkowski functionals clearly indicates that the two aluminium foams have a different internal structure. A more detailed morphological characterization of the foams can be made by investigating local instead of averaged Minkowski functionals. Additional information can also be obtained from the computation of the 2D Minkowski functionals of various slices.

We have demonstrated that the morphological image analysis technique is useful in giving information of the 3D morphological properties of metal foams. Although the amount of data obtained by CT scans is huge, the memory and computation time requirements for the calculation of the Minkowski functionals are low. In order to study the morphological properties of various metal foams in more detail more samples need to be analysed and compared with each other. This challenging



problem is left for future research.

## 6. Summary

Integral-geometry morphological image analysis characterizes patterns in terms of numerical quantities, called Minkowski functionals. These morphological descriptors have an intuitively clear geometrical and topological interpretation. Integral-geometry morphological image analysis yields information on structure in patterns. In most cases this information is complementary to the one obtained from two-point correlation functions.

A remarkable feature of MIA is the big contrast between the level of sophistication of the underlying mathematics and the ease with which MIA can be implemented and used. MIA does not require the surface to be regular, nor is there any need to introduce labyrinth graphs or surface tilings to compute derivatives. MIA is applied directly to the digitized representation of the patterns, it can be implemented with a few lines of computer code, is computationally inexpensive and is easy to use in practice. Therefore we believe it should be part of everyone’s toolbox for analyzing geometrical objects and patterns.

## 7. Acknowledgements

The authors thank Freek Pasop of SkyScan for providing us the micro-CT images of Aluminum foam, our master student Rutger van Merkerk for the SEM images and Patrick Onck for discussions on modeling studies of the mechanical properties of metallic foams.

Part of this research has been financially supported by the “Stichting Nationale Computer Faciliteiten (NCF)”.

## Appendix A: Algorithm

We describe a procedure to determine how the number of open bodies of each type changes when one adds (removes) one black pixel to (from) a given pattern. Using this procedure it is easy to compute the Minkowski functionals for a given pattern, namely by adding the black pixels one-by-one to an initially empty (white) image.

In 2D, the number  $n_2(\mathcal{P})$  of open squares building up the objects in the  $L_x \times L_y$  image  $\mathcal{P}(\mathbf{x}, q) = \mathcal{P}(i, j, q)$ ; ( $i = 1, \dots, L_x, j = 1, \dots, L_y$ ) increases (decreases) with one if one adds (removes) one black pixel at the position  $\mathbf{x} = (i, j)$  to (from) the image. Therefore, if we add an black pixel,

$$\Delta n_2(\mathcal{P}) = 1 \quad , \quad (A.1)$$

where we introduce the symbol  $\Delta$  to indicate that we compute the difference. Similarly the change in the number of open edges,  $\Delta n_1(\mathcal{P})$  is given by

$$\Delta n_1(\mathcal{P}) = \sum_{\alpha=\pm 1} [\mathcal{Q}(i + \alpha, j, q) + \mathcal{Q}(i, j + \alpha, q)] \quad , \quad (A.2)$$

where  $\mathcal{Q}(\mathbf{x}, q) = 1 - \mathcal{P}(\mathbf{x}, q)$ . For the change in the number of vertices,  $n_0(\mathcal{P})$ , we find

$$\Delta n_0(\mathcal{P}) = \sum_{\alpha, \beta=\pm 1} \mathcal{Q}(i + \alpha, j, q) \mathcal{Q}(i + \alpha, j + \beta, q) \mathcal{Q}(i, j + \beta, q) \quad . \quad (A.3)$$

In 3D, the number  $n_3(\mathcal{P})$  of open cubes building up the objects in the  $L_x \times L_y \times L_z$  image  $\mathcal{P}(\mathbf{x}, q) = \mathcal{P}(i, j, k, q)$ ; ( $i = 1, \dots, L_x, j = 1, \dots, L_y, k = 1, \dots, L_z$ ) increases (decreases) with one if one adds (removes) one black pixel to (from) the image at the position  $\mathbf{x} = (i, j, k)$ , i.e  $\Delta n_3(\mathcal{P}) = 1$ . The change in  $n_2(\mathcal{P})$ , the number of open faces, may be computed from

$$\Delta n_2(\mathcal{P}) = \sum_{\alpha=\pm 1} [\mathcal{Q}(i + \alpha, j, k, q) + \mathcal{Q}(i, j + \alpha, k, q) + \mathcal{Q}(i, j, k + \alpha, q)] \quad . \quad (A.4)$$

The change in  $n_1(\mathcal{P})$ , the number of open edges, reads

$$\begin{aligned} \Delta n_1(\mathcal{P}) = & \sum_{\alpha, \beta=\pm 1} [\mathcal{Q}(i + \alpha, j, k, q) \mathcal{Q}(i + \alpha, j + \beta, k, q) \mathcal{Q}(i, j + \beta, k, q) \\ & + \mathcal{Q}(i, j + \alpha, k, q) \mathcal{Q}(i, j + \alpha, k + \beta, q) \mathcal{Q}(i, j, k + \beta, q) \\ & + \mathcal{Q}(i + \alpha, j, k, q) \mathcal{Q}(i + \alpha, j, k + \beta, q) \mathcal{Q}(i, j, k + \beta, q)] \quad . \quad (A.5) \end{aligned}$$

For the change in  $n_0(\mathcal{P})$ , the number of vertices, we find

$$\begin{aligned} \Delta n_0(\mathcal{P}) = & \sum_{\alpha, \beta, \gamma=\pm 1} \mathcal{Q}(i + \alpha, j, k, q) \mathcal{Q}(i + \alpha, j + \beta, k, q) \mathcal{Q}(i, j + \beta, k, q) \\ & \mathcal{Q}(i + \alpha, j, k + \gamma, q) \mathcal{Q}(i + \alpha, j + \beta, k + \gamma, q) \\ & \mathcal{Q}(i, j + \beta, k + \gamma, q) \mathcal{Q}(i, j, k + \gamma, q) \quad . \quad (A.6) \end{aligned}$$

## Appendix B: Programming example (Fortran 90)

```
!
! Minkowski_functionals_3D computes the Minkowski functionals
! (volume,surface,integral mean curvature,euler) for a 3D image,
! represented by the 1D array LATTICE(.). A pixel at (jx,jy,jz) is
! black if LATTICE(jx+Lx*(jy+Ly*jz))=1, otherwise LATTICE(jx+Lx*(jy+Ly*jz))=0.
! Here 0 < jx < Lx, 0 < jy < Ly, and 0 < jz < Lz. The array TMP(.)
! is used as work space.
! Putting FREE_BOUNDARIES = 0 returns Minkowski functionals for
! periodic boundary conditions, other values return Minkowski functionals
! for the image on in a infinitely large empty background.

      subroutine minkowski_functionals(Lx,Ly,Lz,free_boundaries,tmp, &
                                     lattice,volume,surface,curvature,euler)

      implicit integer (a-z)
      integer lattice(0:*),tmp(0:*)

      vol=0
      sur=0
      cur=0
      eul=0

      if(free_boundaries.eq.0) then ! periodic boundary conditions
        tmp(0:Lx*Ly*Lz-1)=0
      else
        tmp(0:(Lx+2)*(Ly+2)*(Lz+2)-1)=0
      endif

      do jz=0,Lz-1
      do jy=0,Ly-1
      do jx=0,Lx-1
        i=jx+Lx*(jy+Ly*jz)
        if( lattice(i) > 0 ) then ! black pixel
          if(free_boundaries.eq.0) then ! periodic boundary conditions
            call minko_3D_periodic(Lx,Ly,Lz,jx,jy,jz,tmp,v,s,c,e)
            tmp(i)=1 ! can only be 0 or 1 in minko_3D_periodic
          else
            call minko_3D_free(Lx+2,Ly+2,Lz+2,jx+1,jy+1,jz+1,tmp,v,s,c,e)
            tmp(jx+1+(Lx+2)*(jy+1+(Ly+2)*(jz+1)))=1
          endif
        endif
        vol=vol+v
      do jx=0,Lx-1
      do jy=0,Ly-1
      do jz=0,Lz-1
```

```

        sur=sur+s
        cur=cur+c
        eul=eul+e
    endif

enddo
enddo
enddo

volume=vol
surface=sur
curvature=cur
euler=eul

end

subroutine minko_3D_periodic(Lx,Ly,Lz,jx,jy,jz,lattice, &
                           volume,surface,curv,euler3D)

implicit integer (a-z)
integer lattice(0:Lx*Ly*Lz-1)
parameter(
    &
    volume_body=1 , &      !(a*a*a, where a is lattice displacement)
    surface_body=-6 , &    !(-6*a*a, open body)
    surface_face=2 , &    !(2*a*a, open face)
    curv_body=3 , &      !(3*a, open body)
    curv_face=-2 , &     !(-2*a, open face)
    curv_edge=1 , &      !(a, open line)
    euler3D_body=-1 , &   !(open body)
    euler3D_face=1 , &   !(open face)
    euler3D_edge=-1 , &  !(open line)
    euler3D_vertex=1)      !(vertices)

nfaces=0
nedges=0
nvert=0

do i0=-1,1,2
jxi=jx+i0
if(jxi.lt.0) then
jxi=Lx+jxi
else if(jxi.ge.Lx) then
jxi=jxi-Lx
endif

```

```

jyi=jy+i0
if(jyi.lt.0) then
jyi=Ly+jyi
else if(jyi.ge.Ly) then
jyi=jyi-Ly
endif
jzi=jz+i0
if(jzi.lt.0) then
jzi=Lz+jzi
else if(jzi.ge.Lz) then
jzi=jzi-Lz
endif
kc1=1-lattice(jxi+Lx*(jy+Ly*jz))
kc2=1-lattice(jx+Lx*(jyi+Ly*jz))
kc3=1-lattice(jx+Lx*(jy+Ly*jzi))
nfaces=nfaces+kc1+kc2+kc3
do j0=-1,1,2
jyj=jy+j0
if(jyj.lt.0) then
jyj=Ly+jyj
else if(jyj.ge.Ly) then
jyj=jyj-Ly
endif
jzj=jz+j0
if(jzj.lt.0) then
jzj=Lz+jzj
else if(jzj.ge.Lz) then
jzj=jzj-Lz
endif
k4=Lx*(jyj+Ly*jz)
k7=Lx*(jy+Ly*jzj)
kc7=1-lattice(jx+k7)
kc1kc4kc5=kc1*(1-lattice(jxi+k4))*(1-lattice(jx+k4))
nedges=nedges+kc1kc4kc5+kc2*(1-lattice(jx+Lx*(jyi+Ly*jzj)))*kc7 &
+kc1*(1-lattice(jxi+k7))*kc7
if(kc1kc4kc5.ne.0) then
do k0=-1,1,2
jzk=jz+k0
if(jzk.lt.0) then
jzk=Lz+jzk
else if(jzk.ge.Lz) then
jzk=jzk-Lz
endif

```

```

k9=Lx*(jy+Ly*jzk)
k10=Lx*(jyj+Ly*jzk)
nvert=nvert+(1-lattice(jxi+k9))*(1-lattice(jxi+k10)) &
          *(1-lattice(jx+k10))*(1-lattice(jx+k9))
enddo ! k0
endif ! kc1kc4kc5
enddo ! j0
enddo ! i0

volume=volume_body
surface=surface_body+surface_face*nfaces
curv=curv_body+curv_face*nfaces+curv_edge*nedges
euler3D=euler3D_body+euler3D_face*nfaces &
        +euler3D_edge*nedges+euler3D_vertex*nvert

return
end

subroutine minko_3D_free(Lx,Ly,Lz,jx,jy,jz,lattice, &
                      volume,surface,curvature,euler3D)

implicit integer (a-z)
integer lattice(0:LX*LY*Lz-1)
parameter(
      &
      volume_body=1 , &      !(a*a*a, where a is lattice displacement)
      surface_body=-6 , &      !(-6*a*a, open body)
      surface_face=2 , &      !(2*a*a, open face)
      curv_body=3 , &      !(3*a, open body)
      curv_face=-2 , &      !(-2*a, open face)
      curv_edge=1 , &      !(a, open line)
      euler3D_body=-1 , &      !(open body)
      euler3D_face=1 , &      !(open face)
      euler3D_edge=-1 , &      !(open line)
      euler3D_vertex=1)      !(vertices)

nfaces=0
nedges=0
nvert=0

do i0=-1,1,2
  jxi=jx+i0
  jyi=jy+i0
  jzi=jz+i0

```

```

kc1=1-lattice(jxi+Lx*(jy+Ly*jz))
kc2=1-lattice(jx+Lx*(jyi+Ly*jz))
kc3=1-lattice(jx+Lx*(jy+Ly*jzi))
nfaces=nfaces+kc1+kc2+kc3
do j0=-1,1,2
jyj=jy+j0
jzj=jz+j0
k4=Lx*(jyj+Ly*jz)
k7=Lx*(jy+Ly*jzj)
kc7=1-lattice(jx+k7)
kc1kc4kc5=kc1*(1-lattice(jxi+k4))*(1-lattice(jx+k4))
nedges=nedges+kc1kc4kc5+kc2*(1-lattice(jx+Lx*(jyi+Ly*jzj)))*kc7 &
+kc1*(1-lattice(jxi+k7))*kc7
if(kc1kc4kc5.ne.0) then
do k0=-1,1,2
jzk=jz+k0
k9=Lx*(jy+Ly*jzk)
k10=Lx*(jyj+Ly*jzk)
nvert=nvert+(1-lattice(jxi+k9))*(1-lattice(jxi+k10)) &
*(1-lattice(jx+k10))*(1-lattice(jx+k9))
enddo ! k0
endif ! kc1kc4kc5
enddo ! j0
enddo ! i0

volume=volume_body
surface=surface_body+surface_face*nfaces
curvature=curv_body+curv_face*nfaces+curv_edge*nedges
euler3D=euler3D_body+euler3D_face*nfaces &
+euler3D_edge*nedges+euler3D_vertex*nvert

end

```

Table.IX Quantities used to determine the coefficients  $c_{\mu\nu}$  in Eq.(C.1).

$A$	$B$	$F_0(A)$	$F_0(B)$	$F_1(A)$	$F_1(B)$	$F_2(A)$	$F_2(B)$	$\sum_{s \in \mathcal{S}'} (A \cap sB)$
$S_2$	$S_2$	4	4	4	4	1	1	$8\{4\{S_0\}, 4\{S_1\}, \{S_2\}\}$
$S_2$	$S_1$	4	2	4	1	1	0	$16\{2\{S_0\}, \{S_1\}\}$
$S_2$	$S_0$	4	1	4	0	1	0	$32\{S_0\}$
$S_1$	$S_1$	2	2	1	1	0	0	$4\{6\{S_0\}, \{S_1\}\}$
$S_1$	$S_0$	2	1	1	0	0	0	$16\{S_0\}$
$S_0$	$S_0$	1	1	0	0	0	0	$8\{S_0\}$

## Appendix C: Derivation of Eq.(36)

We sketch the procedure to compute the coefficients  $c_{\mu\nu}$  by considering the case  $d = 2$ . From Eq.(35) it follows that

$$\begin{aligned}
 \frac{1}{8} \sum_{s \in \mathcal{S}'} F_\mu(A \cap sB) = & c_{00} F_0(A) F_0(B) + c_{11} F_1(A) F_1(B) + c_{22} F_2(A) F_2(B) \\
 & + c_{01} (F_0(A) F_1(B) + F_1(A) F_0(B)) \\
 & + c_{02} (F_0(A) F_2(B) + F_2(A) F_0(B)) \\
 & + c_{12} (F_1(A) F_2(B) + F_2(A) F_1(B)) \quad . \quad (C.1)
 \end{aligned}$$

In order to obtain values for the constants  $c_{\kappa\nu}$  ( $\kappa = 0, 1, 2$  ;  $\nu = \kappa, 2$ ) we take for  $A$  and/or  $B$  the simplexes  $S_\nu$  for  $\nu = 0, 1, 2$ . For all cases the values for  $F_\mu(A)$  and  $F_\mu(B)$  are given in Table IX. Computation of the left hand side of (C.1) requires an evaluation of all possible intersections of  $A$  and  $B$ . Fig.29 and Fig.30 show schematically how the intersections (in grey) may be obtained for the cases  $A = B = S_1$  and  $A = B = S_2$ , respectively. The ninth column of Table IX summarizes the results for  $\sum_{s \in \mathcal{S}'} (A \cap sB)$  for all possible combinations of  $A$  and  $B$ .

Once all the elements of the intersection are obtained it is straightforward to compute the left hand side of (C.1) for  $\mu = 0, 1, 2$ . From (C.1) and the entries in Table IX we obtain for  $\mu = 0$  the following set of equations

$$\left\{ \begin{array}{l}
 16 = 16c_{00} + 16c_{11} + c_{22} + 32c_{01} + 8c_{02} + 8c_{12} \\
 8 = 8c_{00} + 4c_{11} + 12c_{01} + 2c_{02} + c_{12} \\
 4 = 4c_{00} + 4c_{01} + c_{02} \\
 4 = 4c_{00} + c_{11} + 4c_{01} \\
 2 = 2c_{00} + c_{01} \\
 1 = c_{00}
 \end{array} \right. \quad . \quad (C.2)$$

Straightforward algebra then shows that



$$\frac{1}{8} \sum_{s \in \mathcal{S}'} F_0(A \cap sB) = F_0(A)F_0(B) \quad . \quad (C.3)$$

Similarly, for  $\mu = 1$  and  $\mu = 2$  we obtain

$$\frac{1}{8} \sum_{s \in \mathcal{S}'} F_1(A \cap sB) = \frac{1}{2} F_1(A)F_1(B) \quad , \quad (C.4)$$

and

$$\frac{1}{8} \sum_{s \in \mathcal{S}'} F_2(A \cap sB) = F_2(A)F_2(B) \quad , \quad (C.5)$$

in agreement with Eq.(36) .

## Appendix D: Proof of Eq.(56)

We will use the kinematic formulae (27) to compute the configurational average of the Minkowski functionals  $V_\nu^{(d)}$  for a system of grains that are distributed randomly (and uniformly) in a hypercubic domain  $Z \subset \mathbb{Z}^d$  of volume  $|Z|$ . The grains are assumed to be either identical or, in the case that they have random shapes and size, have the same shape-and-size probability distribution. In this appendix we will adopt the lattice version of integral geometry. Results for Euclidean space can be found elsewhere [29, 33].

First, the aim is to compute the mean value of  $V_\nu^{(d)}(\mathcal{A}_N)$ , i.e. the average over all configurations, grain sizes and shapes. We first consider the configurational average of a single grain. Let us write the image  $\mathcal{A}_N$  formed by all grains as

$$\mathcal{A}_N = \mathcal{A}_{N-1} \cup s_N A_N \quad . \quad (D.1)$$

We will sum over all possible symmetry operations  $s_N$  of the grain  $A_N$  on the cubic lattice. With some misuse of notation we will write  $\int$  for this sum and define  $\int ds_i = 2^d d! |Z| \equiv \Omega$ . Making use of the properties of additivity and motion invariance of the Minkowski functionals, application of kinematic formulae (27) yields

$$\begin{aligned} \int V_\mu^{(d)}(\mathcal{A}_N) \frac{ds_N}{\Omega} &= V_\mu^{(d)}(\mathcal{A}_{N-1}) + V_\mu^{(d)}(A_N) - \int V_\mu^{(d)}(\mathcal{A}_{N-1} \cap s_N A_N) \frac{ds_N}{\Omega} \\ &= V_\mu^{(d)}(\mathcal{A}_{N-1}) + V_\mu^{(d)}(A_N) \\ &\quad - \frac{1}{|Z|} \sum_{\nu=0}^{\mu} \sum_{\kappa=0}^{\nu} \binom{\mu}{\nu} \binom{\nu}{\kappa} V_\nu^{(d)}(\mathcal{A}_{N-1}) V_{\mu-\kappa}^{(d)}(A_N) \quad , \end{aligned} \quad (D.2)$$

for the configurational average over the single grain  $A_N$ . It is clear that we can repeat this procedure, i.e. sum over all translations, rotations and reflections of grain  $A_{N-1}$  and so on. The mathematical structure of this recursive procedure is most easily seen by introducing a matrix notation. With the shorthand  $V_\mu \equiv V_\mu^{(d=3)}$ , (D.2) reads

$$\int \mathbf{V}_N \frac{ds_N}{\Omega} = \mathbf{Q}_N \mathbf{V}_{N-1} + \mathbf{R}_N \quad , \quad (D.3)$$

where the matrices  $\mathbf{V}_N$ ,  $\mathbf{Q}_N$  and  $\mathbf{R}_N$  are given by

$$\mathbf{V}_N = \begin{pmatrix} V_0(\mathcal{A}_N) \\ V_1(\mathcal{A}_N) \\ V_2(\mathcal{A}_N) \\ V_3(\mathcal{A}_N) \end{pmatrix} \quad , \quad \mathbf{R}_N = \begin{pmatrix} V_0(A_N) \\ V_1(A_N) \\ V_2(A_N) \\ V_3(A_N) \end{pmatrix} \quad , \quad (D.4a)$$

$$\mathbf{Q}_N = \begin{pmatrix} \alpha_N & 0 & 0 & 0 \\ a_N & \beta_N & 0 & 0 \\ b_N & c_N & \gamma_N & 0 \\ d_N & 3e_N & f_N & \delta_N \end{pmatrix} \quad , \quad (D.4b)$$

with

$$\begin{aligned} \alpha_N &= 1 - \frac{V_0(A_N)}{|Z|} \quad , \quad \beta_N = 1 - \frac{V_0(A_N) + V_1(A_N)}{|Z|} \quad , \\ \gamma_N &= 1 - \frac{V_0(A_N) + 2V_1(A_N) + V_2(A_N)}{|Z|} \quad , \\ \delta_N &= 1 - \frac{V_0(A_N) + 3V_1(A_N) + 3V_2(A_N) + V_3(A_N)}{|Z|} \quad , \\ a_N &= \beta_N - \alpha_N \quad , \quad b_N = \alpha_N - 2\beta_N + \gamma_N \quad , \\ c_N &= 2(\gamma_N - \beta_N) \quad , \quad d_N = \alpha_N - 3\beta_N + 3\gamma_N - \delta_N \quad , \\ e_N &= 3(\beta_N - 2\gamma_N - \delta_N) \quad , \quad f_N = 3(\alpha_N - 2\gamma_N + \delta_N) \quad . \end{aligned} \quad (D.5)$$

Repeating the steps that lead to (D.3) the configurational average over two grains  $A_N$  and  $A_{N-1}$  reads

$$\begin{aligned} \int \int \mathbf{V}_N \frac{ds_N ds_{N-1}}{\Omega^2} &= \int \mathbf{Q}_N \mathbf{V}_{N-1} \frac{ds_{N-1}}{\Omega} + \mathbf{R}_N \\ &= \mathbf{Q}_N \mathbf{Q}_{N-1} \mathbf{V}_{N-2} + \mathbf{V}_N \mathbf{R}_{N-1} + \mathbf{R}_N \quad , \end{aligned} \quad (D.6)$$

and the average over all possible configurations can be written as

$$\int \dots \int \mathbf{V}_N \frac{ds_N \dots ds_1}{\Omega^N} = \mathbf{Q}_N \dots \mathbf{Q}_2 \mathbf{R}_1 + \mathbf{Q}_N \dots \mathbf{Q}_3 \mathbf{R}_2 + \dots + \mathbf{Q}_N \mathbf{R}_{N-1} + \mathbf{R}_N \quad . \quad (D.7)$$

We now use the assumptions about the properties of the individual grains. If all grains are identical we have  $\mathbf{Q} = \mathbf{Q}_i$  and  $\mathbf{R} = \mathbf{R}_i$  for  $i = 1, \dots, N$ . Likewise if the distribution of size and shape of the grains is the same for all grains, averaging (D.7) over this distribution also yields  $\mathbf{Q} = \overline{\mathbf{Q}_i}$  and  $\mathbf{R} = \overline{\mathbf{R}_i}$  for all  $i$ . Evidently the latter case contains the former. Thus, we can simplify the notation by dropping the subscript of  $\alpha_N$  etc. Averaging (D.7) over the size and shape of the grains yields

$$\langle \mathbf{V} \rangle_N \equiv \int \dots \int \mathbf{V}_N \frac{ds_N \dots ds_1}{\Omega^N} = (\mathbf{1} + \mathbf{Q} + \dots + \mathbf{Q}^{N-1})\mathbf{R} \quad . \quad (D.8)$$

By mathematical induction it can be shown that

$$\mathbf{Q}^n = \begin{pmatrix} \alpha^n & 0 & 0 & 0 \\ aU_n(\alpha, \beta) & \beta^n & 0 & 0 \\ Q_{1,3}^{(n)} & cU_n(\beta, \gamma) & \gamma^n & 0 \\ Q_{1,4}^{(n)} & Q_{2,4}^{(n)} & fU_n(\gamma, \delta) & \delta^n \end{pmatrix} \quad , \quad (D.9)$$

where

$$\begin{aligned} Q_{1,3}^{(n)} &= bU_n(\alpha, \gamma) + acV_{n-1}(\alpha, \beta, \gamma), \\ Q_{1,4}^{(n)} &= dU_n(\alpha, \delta) + aeV_{n-1}(\alpha, \beta, \delta) + bfV_{n-1}(\alpha, \gamma, \delta) + acfW_{n-2}(\alpha, \beta, \gamma, \delta), \\ Q_{2,4}^{(n)} &= eU_n(\beta, \delta) + cfV_{n-1}(\beta, \gamma, \delta) \quad , \end{aligned} \quad (D.10)$$

and

$$\begin{aligned} U_n(x, y) &= xU_{n-1} + y^n = \frac{x^n - y^n}{x - y}, \\ V_n(x, y, z) &= xV_{n-1}(x, y, z) + U_n(y, z) = \frac{U_{n+1}(x, y) - U_{n+1}(x, z)}{y - z}, \\ W_n(x, y, z, t) &= xW_{n-1}(x, y, z, t) + V_n(y, z, t) \quad . \end{aligned} \quad (D.11)$$

Let us write  $v_\nu \equiv \overline{V_\nu(A_i)}$  for the average over size and shape of the Minkowski functionals for each single grain  $A_i$ . We have

$$\begin{aligned} \alpha &= 1 - \frac{v_0}{|Z|}, \\ \beta &= 1 - \frac{v_0 + v_1}{|Z|}, \\ \gamma &= 1 - \frac{v_0 + 2v_1 + v_2}{|Z|}, \\ \delta &= 1 - \frac{v_0 + 3v_1 + 3v_2 + v_3}{|Z|} \quad , \end{aligned} \quad (D.12)$$

and somewhat tedious but straightforward algebra yields

$$\langle \mathbf{V} \rangle_N = |Z| \begin{pmatrix} 1 - \alpha^N \\ \alpha^N - \beta^N \\ -\alpha^N + 2\beta^N - \gamma^N \\ \alpha^N - 3\beta^N + 3\gamma^N - \delta^N \end{pmatrix}. \quad (D.13)$$

In the bulk limit  $(N, |Z|) \rightarrow \infty$  with the density of particles  $\rho = N/|Z|$  fixed, we have

$$\lim_{N \rightarrow \infty} \alpha^N = \lim_{N \rightarrow \infty} \left(1 - \frac{v_0}{|Z|}\right)^N = \lim_{N \rightarrow \infty} \left(1 - \frac{v_0 \rho}{N}\right)^N = e^{-\rho v_0}, \quad (D.14)$$

and

$$\lim_{N \rightarrow \infty} \frac{\langle \mathbf{V} \rangle_N}{N} = \begin{pmatrix} (1 - e^{-\rho v_0})/\rho \\ e^{-\rho v_0}(1 - e^{-\rho v_1})/\rho \\ -e^{-\rho v_0}(1 - 2e^{-\rho v_1} + e^{-\rho(2v_1+v_2)})/\rho \\ e^{-\rho v_0}(1 - 3e^{-\rho v_1} + 3e^{-\rho(2v_1+v_2)} - e^{-\rho(3v_1+3v_2+v_3)})/\rho \end{pmatrix}. \quad (D.15)$$

Expressions (D.15) agree with those of Ref. [33].

## Appendix E: Proof of Eq.(57)

Here we start from the alternative formulation of integral geometry on a lattice (see section 2.9) and use kinematic formulae (36) to compute the configurational average of the functionals  $F_\nu$ . We adopt the same strategy as in appendix D to compute the mean value of  $F_\nu(\mathcal{A}_N)$ . Making use of the properties of additivity and motion invariance of the functionals  $F_\nu$ , application of kinematic formulae (36) yields for the configurational average over the single grain  $A_N$

$$\begin{aligned} \frac{1}{\Omega} \sum_{s_N \in \mathcal{S}'} F_\mu(\mathcal{A}_N) &= F_\mu(\mathcal{A}_{N-1}) + F_\mu(A_N) - \frac{1}{\Omega} \sum_{s_N} F_\mu(\mathcal{A}_{N-1} \cap s_N A_N) \\ &= F_\mu(\mathcal{A}_{N-1}) + F_\mu(A_N) - \frac{1}{|Z|} \binom{d}{\mu}^{-1} F_\mu(\mathcal{A}_{N-1}) F_\mu(A_N) \end{aligned} \quad (E.1)$$

where  $\Omega \equiv \sum_{s_N \in \mathcal{S}'} 1 = 2^d d! |Z|$  and  $|Z|$  denotes the number of lattice points of the finite lattice  $\mathbb{Z}^d$ . As in appendix D, it is convenient to write (E.1) in matrix notation. We have

$$\frac{1}{\Omega} \sum_{s_N \in \mathcal{S}'} \mathbf{F}_N = \mathbf{Q}_N \mathbf{F}_{N-1} + \mathbf{R}_N, \quad (E.2)$$

where, for  $d = 3$ , the matrices  $\mathbf{F}_N$ ,  $\mathbf{Q}_N$  and  $\mathbf{R}_N$  are given by

$$\mathbf{F}_N = \begin{pmatrix} F_0(\mathcal{A}_N) \\ F_1(\mathcal{A}_N) \\ F_2(\mathcal{A}_N) \\ F_3(\mathcal{A}_N) \end{pmatrix}, \quad \mathbf{R}_N = \begin{pmatrix} F_0(A_N) \\ F_1(A_N) \\ F_2(A_N) \\ F_3(A_N) \end{pmatrix}, \quad (E.3a)$$

$$\mathbf{Q}_N = \begin{pmatrix} 1 - \frac{F_0(A_N)}{|Z|} & 0 & 0 & 0 \\ 0 & 1 - \frac{F_1(A_N)}{3|Z|} & 0 & 0 \\ 0 & 0 & 1 - \frac{F_2(A_N)}{3|Z|} & 0 \\ 0 & 0 & 0 & 1 - \frac{F_3(A_N)}{|Z|} \end{pmatrix}. \quad (E.3b)$$

Note that in contrast to Eq.(D.4b), (E.3b) is a diagonal matrix, leading to considerable simplification of the subsequent algebra.

Repeated use of recursion (E.2) and averaging over all configurations, grain sizes and shapes yields

$$\langle \mathbf{F} \rangle_N \equiv \frac{1}{\Omega^N} \sum_{s_1, \dots, s_N \in \mathcal{S}'} \mathbf{F}_N \frac{ds_N \dots ds_1}{\Omega^N} = (\mathbf{1} + \mathbf{Q} + \dots + \mathbf{Q}^{N-1}) \mathbf{R}. \quad (E.4)$$

It is easy to show that

$$\mathbf{1} + \mathbf{Q} + \dots + \mathbf{Q}^{N-1} = \begin{pmatrix} \frac{1-\alpha^N}{1-\alpha} & 0 & 0 & 0 \\ 0 & \frac{1-\beta^N}{1-\beta} & 0 & 0 \\ 0 & 0 & \frac{1-\gamma^N}{1-\gamma} & 0 \\ 0 & 0 & 0 & \frac{1-\delta^N}{1-\delta} \end{pmatrix}, \quad (E.5)$$

where

$$\alpha = 1 - f_0/|Z|, \quad \beta = 1 - f_1/3|Z|, \quad \gamma = 1 - f_2/3|Z|, \quad \delta = 1 - f_3/|Z| \quad (E.6)$$

and  $f_\nu \equiv \overline{F_\nu(A_i)}$  denotes the average over size and shape of the functional  $F_\nu$  for a single grain  $A_i$ . Straightforward algebra yields

$$\langle \mathbf{F} \rangle_N = |Z| \begin{pmatrix} 1 - \alpha^N \\ 3(1 - \beta^N) \\ 3(1 - \gamma^N) \\ 1 - \delta^N \end{pmatrix}. \quad (E.7)$$

In the bulk limit  $(N, |Z|) \rightarrow \infty$  with the density of particles  $\rho = N/|Z|$  fixed, we have

$$\lim_{N \rightarrow \infty} \alpha^N = \lim_{N \rightarrow \infty} \left(1 - \frac{f_0}{|Z|}\right)^N = \lim_{N \rightarrow \infty} \left(1 - \frac{f_0 \rho}{N}\right)^N = e^{-\rho f_0}, \quad (E.8)$$

and

$$\lim_{N \rightarrow \infty} \frac{\langle \mathbf{F} \rangle_N}{N} = \begin{pmatrix} (1 - e^{-\rho f_0})/\rho \\ 3(1 - e^{-\rho f_1/3})/\rho \\ 3(1 - e^{-\rho f_2/3})/\rho \\ (1 - e^{-\rho f_3})/\rho \end{pmatrix} . \quad (E.9)$$

In general, for any  $d > 0$  we find

$$\lim_{N \rightarrow \infty} \frac{\langle F_\nu \rangle_N}{N} = \binom{d}{\nu} \left[ 1 - \exp \left( -\rho f_\nu \binom{d}{\nu}^{-1} \right) \right] / \rho ; \quad \nu = 0, \dots, d . \quad (E.10)$$

## 1. Figure Captions

- Fig.1 Minkowski sum of a line segment  $L$  (black area) of length  $a$  and a line segment  $S_r^{(1)}$  of length  $2r$  yields the parallel set  $L_r$  (black and grey area) at a distance  $r$ .
- Fig.2 Minkowski sum of a disc  $S_r^{(2)}$  of radius  $r$  and a circular disk  $D$  of radius  $a$ , a square  $Q$  of edge length  $a$  and an equilateral triangle  $T$  of side length  $a$  yields the parallel sets (union of the black and grey area)  $D_r$ ,  $Q_r$  and  $T_r$  respectively.
- Fig.3 Two- and three-dimensional figures with various connectivity numbers (Euler characteristics)  $\chi$ .
- Fig.4 Decomposition of the pixels of a two-dimensional black-and-white pattern (left) into squares, edges and vertices (right).
- Fig.5  $4 \times 4$  checkerboard pattern. The black line denotes the boundary. Left: Free boundaries; right: Periodic boundaries.
- Fig.6 Basic elements of integral geometry in  $\mathbb{Z}^2$ : An elementary square (a), two connected elementary squares (b), two 0-dimensional planes (lattice points)  $E_0$  and two 1-dimensional planes (horizontal and vertical lines through the lattice points)  $E_1$ .
- Fig.7 A two-dimensional lattice  $\mathbb{Z}^2$  decomposed into disjoint sets of vertices  $O_0$ , edges  $O_1$ , and faces  $O_2$  (black objects). The simplexes  $S_0$ ,  $S_1$  and  $S_2$  and 2-cubes  $E_2(1)$  and  $E_2(3)$  are shown in gray.
- Fig.8 Graining procedure of a point pattern in two dimensions. Left: The grains are discrete approximations to a sphere with radius three in the Euclidean space. Right: The grains are squares of edge length seven. The light grey pixels indicate the positions of the germs.
- Fig.9 Schematic representation of how to use MIA to analyze the morphological properties of (patterns that can be interpreted in terms of) 2D point patterns.
- Fig.10 Schematic representation of how to use MIA to analyze the morphological properties of 2D digitized images.
- Fig.11 Graining procedure for the SC lattice with periodic boundary conditions and  $L_0 = 4$ . The thick solid line indicates the dimensions of the unit cell.
- Fig.12 Minkowski functionals as a function of  $r$  for the perfect SC (dotted curve), FCC (solid curve) and BCC (dashed curve) lattice with  $M = 1$  and  $L_0 = 32$  with periodic boundary conditions.

Fig.13 Minkowski functionals as a function of  $r$  for BCC lattice structures with  $M = 8$  and  $L_0 = 16$  with periodic boundary conditions. Solid line: Perfect BCC lattice; dashed line: BCC lattice to which  $\pm 30\%$  of impurities have been added at randomly chosen positions; dotted line: BCC lattice of which  $\pm 30\%$  of randomly chosen basic lattice points have been moved over a randomly chosen distance 0 or 1; dash-dotted line: BCC lattice of which all the basic lattice points have been moved over a randomly chosen distance 0 or 1.

Fig.14 Euler characteristic as a function of  $r$  for FCC lattice structures with  $M = 5$  and  $L_0 = 16$  with free boundary conditions. (a): Perfect FCC lattice, grains are spheres; (b): FCC lattice with screw dislocation at the centre, grains are spheres; (c): FCC lattice with edge dislocation at the centre, grains are spheres; (d): Perfect FCC lattice, grains are cubes; (e): FCC lattice with screw dislocation at the centre; grains are cubes; (f): FCC lattice with edge dislocation at the centre; grains are cubes.

Fig.15 Euler characteristic as a function of  $r$  for BCC lattice structures with  $M = 5$  and  $L_0 = 16$  with free boundary conditions. (a): Perfect BCC lattice, grains are spheres; (b): BCC lattice with screw dislocation at the centre, grains are spheres; (c): BCC lattice with edge dislocation at the centre, grains are spheres; (d): Perfect BCC lattice, grains are cubes; (e): BCC lattice with screw dislocation at the centre; grains are cubes; (f): BCC lattice with edge dislocation at the centre; grains are cubes.

Fig.16 Minkowski functionals for random point sets as a function of the radius  $r$  of the “spherical” grains. Periodic boundary conditions have been employed. Solid lines: 1024 points in a cubic box of edge length 128; dash-dotted lines: Fit to this data, using the expressions given by Eq. (55) . Dashed lines: 512 points in a cubic box of edge length 128; dotted lines: Fit to this data, using the expressions given by Eq. (55) .

Fig.17 Minkowski functionals for random point sets on a square lattice subject to periodic boundary conditions. The grains are squares of linear size  $r$ . Markers:  $N = 10240$  points in a square of edge length  $L = 1024$ ; solid lines: Analytical result for the infinite system, as obtained from the lattice formulation of integral geometry.

Fig.18 Minkowski functionals for random point sets on a cubic lattice subject to periodic boundary conditions. The grains are cubes of linear size  $r$ . Markers:  $N = 1024$  points in a cube of size  $L = 128$ ; solid lines: Analytical result for the infinite system, as obtained from the lattice formulation of integral geometry.



- Fig.19 Unit cube for the nodal primitive P surface (a) and the nodal double diamond D surface (b). The surfaces are generated from Eqs. (61) and (62) respectively.
- Fig.20 Unit cube for the nodal gyroid G surface (a) and the nodal S surface (b). The surfaces are generated from Eqs. (63) and (64) respectively.
- Fig.21 Unit cube for the nodal Neovius C(P) surface (a) and the nodal C(Y) surface (b). The surfaces are generated from Eqs. (65) and (66) respectively.
- Fig.22 Unit cube for the nodal  $\pm Y$  surface (a) and the nodal C( $\pm Y$ ) surface (b). The surfaces are generated from Eqs. (67) and (68) respectively.
- Fig.23 Unit cube for the nodal I-WP surface (a) and the nodal F-RD surface (b). The surfaces are generated from Eqs. (69) and (70) respectively.
- Fig.24 In-situ deformation in a Philips XL30-FEG-ESEM of Duocel 40 PPI foam with a relative density of approximately 7%. The alloy composition is A6101.
- Fig.25 2D computer tomography image of a closed-cell (left) and open-cell (right) aluminium foam.
- Fig.26 3D computer tomography images of two aluminium foams of different type. Left: Closed-cell aluminium foam; right: Open-cell aluminium foam.
- Fig.27 Minkowski functionals as a function of the threshold  $q$  as obtained from a 3D CT image of a dense aluminium foam.
- Fig.28 Minkowski functionals as a function of the threshold  $q$  as obtained from a 3D CT image of an open aluminium foam.
- Fig.29 Intersections (in gray) of the simplexes  $A = S_1$  and  $B = S_1$  that appear in the expression of the kinematic formula Eq.(36) . Because of the rotational and reflection symmetry of  $B$ , each intersection contributes to Eq.(36) with a weight of four.
- Fig.30 Intersections (in gray) of the simplexes  $A = S_2$  and  $B = S_2$  that appear in the expression of the kinematic formula Eq.(36) . Because of the rotational and reflection symmetry of  $B$ , each intersection contributes to Eq.(36) with a weight of eight.

## 2. References

1. P. Ball, *The Self-Made Tapestry: Pattern Formation in Nature*, (Oxford University Press, Oxford, 1998).
2. S. Hyde, S. Andersson, K. Larsson, Z. Blum, T. Landh, S. Lidin, B.W. Ninham, *The Language of Shape; The role of curvature in condensed matter: Physics, Chemistry and Biology*, (Elsevier, Amsterdam, 1997).
3. J.C. Russ, *The Image Processing Handbook*, (CRC Press, Florida, 1995).
4. K.R. Castleman, *Digital Image Processing*, (Prentice Hall, New Jersey, 1996).
5. R.C. Gonzalez and R.E. Woods, *Digital Image Processing*, (Addison-Wesley, Massachusetts, 1993).
6. A. Rosenfeld, A.C. Kak, *Digital Picture Processing*, (Academic Press, New York, 1982).
7. Luciano da Fontoura Costa and Roberto Marcondes Cesar Jr., *Shape analysis and classification: Theory and Practice*, (CRC Press, Florida, 2001).
8. H. Hadwiger, *Vorlesungen über Inhalt, Oberfläche und Isoperimetrie*, (Springer Verlag, Berlin, 1957).
9. L.A. Santaló, *Integral Geometry and Geometric Probability*, (Addison-Wesley, Reading, Massachusetts, 1976).
10. D. Stoyan, W.S. Kendall, J. Mecke, *Stochastic Geometry and its Applications*, (Akademie Verlag, Berlin, 1989).
11. K.R. Mecke, H. Wagner, Euler Characteristic and Related Measures for Random Geometric Sets, *J. Stat. Phys.* 64 (1991) 843 – 850 .
12. K.R. Mecke, A morphological model for complex fluids, *J. Phys.: Condens. Matter* 8 (1996) 9663 – 9667.
13. K.R. Mecke, Morphological thermodynamics of composite media, *Fluid Phase Equilibria* 150 – 151 (1998) 591 – 598.
14. K.R. Mecke, Integral geometry in statistical physics, *Int. J. Mod. Phys. B12* (1998) 861 – 899 .
15. A.L. Mellot, The topology of large-scale structure in the universe, *Phys. Rep.* 193 (1990) 1 – 39.
16. K.R. Mecke, T. Buchert, H. Wagner, Robust morphological measures for large-scale structure in the Universe, *Astron. Astrophys.* 288 (1994) 697 – 704.
17. N.G. Makarenko, L.M. Karimova, A.G. Terekhov, A.V. Kardashev, Minkowski Functionals and Comparison of Discrete Samples in Seismology, *Physics of the Solid Earth* 36 (2000) 305 – 309.
18. J.S. Kole, K. Michielsen, H. De Raedt, Morphological image analysis of quantum motion in billiards, *Phys. Rev.* E63 (2001) 016201.
19. C.N. Likos, K.R. Mecke, H. Wagner, Statistical morphology of random interfaces in microemulsions, *J. Chem. Phys.* 102 (1995) 9350 – 9361.
20. K.R. Mecke, Morphological characterization of patterns in reaction-diffusion

- systems, Phys. Rev. E53 (1996) 4794 – 4800.
21. K.R. Mecke, V. Sofonea, Morphology of spinodal decomposition, Phys. Rev. E56 (1997) R3761 – R3764.
  22. V. Sofonea, K.R. Mecke, Morphological characterization of spinodal decomposition kinetics, Eur. Phys. J. B8 (1999) 99 – 112.
  23. S. Herminghaus, K. Jacobs, K. Mecke, J. Bischof, A. Fery, M. Ibn-Elhaj, S. Schlagowski, Spinodal Dewetting in Liquid Crystal and Liquid Metal Films, Science 282 (1998) 916 – 919.
  24. K. Jacobs, S. Herminghaus, K.R. Mecke, Thin Liquid Polymer Films Rupture via Defects, Langmuir 14 (1998) 965 – 969.
  25. G. Matheron, *Random Sets and Integral Geometry*, (John Wiley and Sons, New York, 1975).
  26. J. Serra, *Image Analysis and Mathematical Morphology*, (Academic Press, London, 1982).
  27. C.R. Giardina, E.R. Dougherty, *Morphological Methods in Image and Signal Processing*, (Prentice Hall, New Jersey, 1988).
  28. Ivan R. Terol-Villalobos, Morphological Image Enhancement and Segmentation, Advances in Imaging and Electron Physics 118 (2001) 208 – 273.
  29. K. Michielsen and H. De Raedt, Integral-Geometry Morphological Image Analysis, Phys. Rep. 347 (2001) 461 - 538.
  30. D.A. Klain, Kinematic formulas for finite vector spaces, Discr. Math. 179 (1998) 121 - 132.
  31. D.A. Klain, Kinematic formulas for finite lattices, Annals of Combinatorics 1 (1997) 353 – 366.
  32. K. Voss, *Discrete Images, Objects and Functions in  $Z^n$* , Algorithms and Combinatorics 11, (Springer, Berlin, 1992).
  33. K.R. Mecke, in: *Statistical Physics and Spatial Statistics*, K.R. Mecke and D. Stoyan (Eds.), Lecture Notes in Physics 554 (Springer, Berlin, 2000).
  34. D.A. Klain and G.-C. Rota, *Introduction to Geometric Probability*, (Cambridge University Press, Cambridge UK, 1997).
  35. G. Matheron, *Random Sets and Integral Geometry*, (John Wiley and Sons, New York, 1975).
  36. A.P. Gast, W.B. Russel, Simple Ordering in Complex Fluids. Colloidal particles suspended in solution provide intriguing models for studying phase transitions, Physics Today 51 (1998) 24 – 30.
  37. J.Th.M. De Hosson, O. Kanert, A.W. Sleswyck, Dislocations in solids investigated by means of nuclear magnetic resonance, in *Dislocations in Solids*, ed. F.R.N. Nabarro, (North-Holland, Amsterdam, 1983), p. 441–534.
  38. J.D. Eshelby, F.C. Frank, F.R.N. Nabarro, The equilibrium of linear arrays of dislocations, Phil. Mag. 42 (1951) 351 – 364.
  39. G. Leibfried, Verteilung von Versetzungen im statischen Gleichgewicht, Z.

- Phys. 130 (1951) 214–226.
40. R.W. Lardner, *Mathematical theory of dislocations and fracture*, (Toronto Univ. Press, Toronto, 1974).
  41. J. Weertman, *Dislocation based fracture mechanics*, (World Scientific, Singapore, 1996).
  42. J.P. Hirth, J. Lothe, *Theory of dislocations*, (Mc Graw Hill, New York, 1968).
  43. J.Th.M. De Hosson, A. Roos, E.D. Metselaar, Temperature rise due to fast-moving dislocations, *Philos. Magazine* 81 (2001) 1099–1120.
  44. A. Roos, J.Th.M. De Hosson, E. van der Giessen, A two-dimensional computational methodology for high-speed dislocations in high strain-rate deformation, *Comput. Mat. Sci.* 20 (2001) 1–18.
  45. A. Roos, J.Th.M. De Hosson, E. van der Giessen, High-speed dislocations in high strain rate deformations, *Comput. Mat. Sci.* 20 (2001) 19–27.
  46. P. Davy, Projected thick sections through multi-dimensional particle aggregates, *J. Appl. Prob.* 13 (1976) 714 – 722.
  47. H.G. Kellerer, Minkowski Functionals of Poisson Processes, *Z. Wahrscheinlichkeitstheorie verw. Gebiete* 67 (1984) 63 – 84.
  48. J. Klinowski, A.L. Mackay, H. Terrones, Curved surfaces in chemical structure, *Phil. Trans. R. Soc. Lond.* A354 (1996) 1975 – 1987.
  49. H.G. von Schnering, R. Nesper, How Nature Adapts Chemical Structures to Curved Surfaces, *Angew. Chem.* 26 (1987) 1059 – 1080.
  50. St. Andersson, S.T. Hyde, H.G. von Schnering, The intrinsic curvature of solids, *Z. Kristallogr.* 168 (1984) 1 – 17.
  51. A.L. Mackay, Periodic minimal surfaces, *Nature* 314 (1985) 604 – 606.
  52. A.L. Mackay, Equipotential Surfaces in Periodic Charge Distributions, *Angew. Chem.* 27 (1988) 849 – 850.
  53. I.S. Barnes, S.T. Hyde, B.W. Ninham, The caesium chloride zero potential surface is not the Schwarz P-surface, *Colloque de Physique C7* (1990) 19 – 24.
  54. V. Luzzati, A. Tardieu, T. Gulik-Krzywicki, E. Rivas, F. Reiss-Husson, Structure of the Cubic Phases of Lipid-Water Systems, *Nature* 220 (1968) 485 – 488.
  55. W. Longley, T.J. McIntosh, A bicontinuous tetrahedral structure in a liquid-crystalline lipid, *Nature* 304 (1983) 612 – 614.
  56. K. Larsson, Two cubic phases in monoolein-water system, *Nature* 304 (1983) 664 – 664.
  57. K. Fontell, Cubic phases in surfactant and surfactant-like lipid systems, *Colloid. Polym. Sci.* 268 (1990) 264 – 285.
  58. V. Luzzati, R. Vargas, P. Mariani, A. Gulik, H. Delacroix, Cubic phases of lipid-containing systems. Elements of a theory and biological connotations, *J. Mol. Biol.* 229 (1993) 540 – 551.
  59. P. Mariani, V. Luzzati, H. Delacroix, Cubic Phases of Lipid-containing Sys-

- tems, *J. Mol. Biol.* 204 (1999) 165 – 189.
60. E.L. Thomas, D.B. Alward, D.J. Kinning, D.C. Martin, D.L. Handlin Jr., L.J. Fetters, Ordered Bicontinuous Double-Diamond Structure of Star Block Copolymers: A New Equilibrium Microdomain Morphology, *Macromolecules* 19 (1986) 2197 – 2202.
  61. H. Hasegawa, H. Tanaka, K. Yamasaki, T. Hashimoto, Bicontinuous Microdomain Morphology of Block Copolymers. 1. Tetrapod-Network Structure of Polystyrene-Polyisopropene Diblock Polymers, *Macromolecules* 20 (1987) 1651 – 1662.
  62. D.M. Anderson, E.L. Thomas, Microdomain Morphology of Star Copolymers in the Strong-Segregation Limit, *Macromolecules* 21 (1988) 3221 – 3230.
  63. E.L. Thomas, D.M. Anderson, C.S. Henkee, D. Hoffman, Periodic area-minimizing surfaces in block copolymers, *Nature* 334 (1988) 598 – 601.
  64. Y. Mogi, K. Mori, Y. Matsushita, I. Noda, Tricontinuous Morphology of Triblock Copolymers of the ABC Type, *Macromolecules* 25 (1992) 5412 – 5415.
  65. R. Xie, B. Yang, B. Jiang, The ordered bicontinuous double-diamond morphology in triblock copolymer/homopolymer blends, *Macromolecules* 26 (1993) 7097 – 7099.
  66. Y. Matsushita, M. Tamura, I. Noda, Tricontinuous Double-Diamond Structure Formed by a Styrene-Isopropene-2-Vinylpyridine Triblock Copolymer, *Macromolecules* 27 (1994) 3680 – 3682.
  67. M.F. Schulz, F.S. Bates, K. Almdal, K. Mortensen, Epitaxial Relationship for Hexagonal-to-Cubic Phase transition in a Block Copolymer Mixture, *Phys. Rev. Lett.* 73 (1994) 86 – 89.
  68. D.A. Hajduk, P.E. Harper, S.M. Gruner, C.C. Honeker, G. Kim, E.L. Thomas, L.J. Fetters, The Gyroid: A New Equilibrium Morphology in Weakly Segregated Diblock Copolymers, *Macromolecules* 27 (1994) 4063 – 4075.
  69. D.A. Hajduk, P.E. Harper, S.M. Gruner, C.C. Honeker, E.L. Thomas, L.J. Fetters, A Reevaluation of bicontinuous cubic Phases in Starblock Copolymers, *Macromolecules* 28 (1995) 2570 – 2573.
  70. H. Jinnai, T. Hashimoto, D. Lee, S.-H. Chen, Morphological Characterization of Bicontinuous Phase-Separated Polymer Blends and One-Phase Microemulsions, *Macromolecules* 30 (1997) 130 – 136.
  71. S. Sakurai, H. Irie, H. Umeda, S. Nomura, H.H. Lee, J.K. Kim, Gyroid Structures and Morphological Control in Binary Blends of Polystyrene-*block*-polyisopropene Diblock Copolymers, *Macromolecules* 31 (1998) 336 – 343.
  72. M.W. Hamersky, M.A. Hillmeyer, M. Tirrell, F.S. Bates, T.P. Lodge, E.D. von Meerwall, Block Copolymer Self-Diffusion in the Gyroid and Cylinder Morphologies, *Macromolecules* 31 (1998) 5363 – 5370.
  73. M.E. Vigild, K. Almdal, K. Mortensen, I.W. Hamley, J.P.A. Fairclough, A.J. Ryan, Transformations to and from the Gyroid Phase in a Diblock Copolymer,

- Macromolecules 31 (1998) 5702 – 5716.
74. F.S. Bates, G.H. Fredrickson, Block Copolymers-Designer Soft Materials. Advances in synthetic chemistry and statistical theory provide unparalleled control over molecular scale morphology in this class of macromolecules, *Physics Today* 52 (1999) 32 – 38.
  75. H. Jinnai, T. Kajihara, H. Watashiba, Y. Nishikawa, R.J. Spontak, Interfacial and topological measurements of bicontinuous polymer morphologies, *Phys. Rev. E* 64 (2001) 010803.
  76. G. Donnay, D.L. Pawson, X-ray Diffraction Studies of Echinoderm Plates, *Science* 166 (1969) 1147 – 1150.
  77. H.-U. Nissen, Crystal Orientation and Plate Structure in Echinoid Skeletal Units, *Science* 166 (1969) 1150 – 1152.
  78. K. Larsson, Cubic Lipid-Water Phases: Structures and Biomembrane Aspects, *J. Phys. Chem.* 93 (1989) 7304 – 7314.
  79. R. Hołyst, D. Plewczyński, A. Aksimentiev, K. Burdzy, Diffusion on curved, periodic surfaces, *Phys. Rev. E* 60 (1999) 302 – 307.
  80. D. Plewczyński, R. Hołyst, Reorientational angle distribution and diffusion coefficient for nodal and cylindrical surfaces, *J. Chem. Phys.* 113 (2000) 9920 – 9929.
  81. D. Plewczyński, R. Hołyst, Approach to equilibrium of particles diffusing on curved surfaces, *Physica A* 295 (2001) 371 – 378.
  82. W. Fischer, E. Koch, On 3-periodic minimal surfaces, *Z. Kristallogr.* 179 (1987) 31 – 52.
  83. K. Grosse-Brauckmann, On Gyroid Interfaces, *J. Coll. Interf. Sci.* 187 (1997) 418 – 428 .
  84. A.H. Schoen, *Infinite periodic minimal surfaces without self-intersections*, (NASA Technical NOTE No. D-5541, 1970).
  85. S.T. Hyde, The topology and geometry of infinite periodic surfaces, *Z. Kristallogr.* 187 (1989) 165 – 185.
  86. W. Fischer, E. Koch, Genera of Minimal Balance Surfaces, *Act. Cryst.* A45 (1989) 726 – 732 .
  87. A. Aksimentiev, M. Fiałkowski, R. Hołyst, Morphology of surfaces in mesoscopic polymers, surfactants, electrons, or reaction-diffusion systems: Methods, simulations, and measurements, *Adv. in Chem. Phys.* 121 (2002), 141 – 239.
  88. H.A. Schwarz, *Gesammelte Mathematische Abhandlungen*, (Springer, Berlin, 1890).
  89. K. Michielsen, H. De Raedt, J.G.E.M. Fraaije, Morphological characterization of spatial patterns, *Prog. Theor. Phys. Supp.* 138 (2000) 543 - 548.
  90. E.R. Neovius, *Bestimmung zweier spezieller periodischer Minimalflächen* , (Akad. Abhandlungen, Helsingfors, 1883).

91. E. Koch, W. Fischer, On 3-periodic minimal surfaces with non-cubic symmetry, *Z. Krystallogr.* 183 (1988) 129 – 152.
92. D.J. Roaf, The Fermi surfaces of Cu, Ag, Au, *Phil. Trans. R. Soc. Lond.* A255 (1963) 135 – 152.
93. A.L. Mackay, Crystallographic surfaces, *Proc. R. Soc. Lond.* A442 (1993) 47 – 59.
94. H.G. von Schnering, R. Nesper, Nodal surfaces of Fourier series: fundamental invariants of structured matter, *Z. Phys.* B83 (1991) 407 – 412.
95. U.S. Schwarz, G. Gompper, Systematic approach to bicontinuous cubic phases in ternary amphiphilic systems, *Phys. Rev.* E59 (1999) 5528 – 5541.
96. P.J.F. Gandy, S. Bardhan, A.L. Mackay, J. Klinowski, Nodal surface approximations to the P, D, G and I-WP triply periodic minimal surfaces, *Chem. Phys. Lett.* 336 (2001) 187 – 195.
97. J.C. Elliot, *Method of producing metal foam*, US patent No. 2,751,289 (1956).
98. M.F. Ashby, A.G. Evans, J.W. Hutchinson, N.A. Fleck, *Metal foams: A design guide*, (University of Cambridge, Cambridge UK, 1998).
99. L. Gibson, M.F. Ashby, *Cellular solids*, 2nd edition, (Cambridge University Press, Cambridge UK, 1997).
100. E.W. Andrews, G. Gioux, P. Onck, L.J. Gibson, Size effects in ductile cellular solids, *Int. J. Mech. Sci.* 43 (2001) 701–713.
101. V.S. Deshpande, M.F. Ashby, N.A. Fleck, Foam topology bending versus stretching dominated architectures, *Acta Materialia* 49 (2001) 1035–1040.
102. A.G. Evans, J.W. Hutchinson, N.A. Fleck, M.F. Ashby, H.N.G. Wadley, The topological design of multifunctional cellular metals, *Prog. Mat. Sci.* 46 (2001) 309–327.
103. Y. Nishikawa, H. Jinnai, T. Koga, T. Hashimoto, S.T. Hyde, Measurements of interfacial curvatures of bicontinuous structure from three-dimensional digital images. 1. A parallel surface method, *Langmuir* 14 (1998) 1242 – 1249.

Fig.1

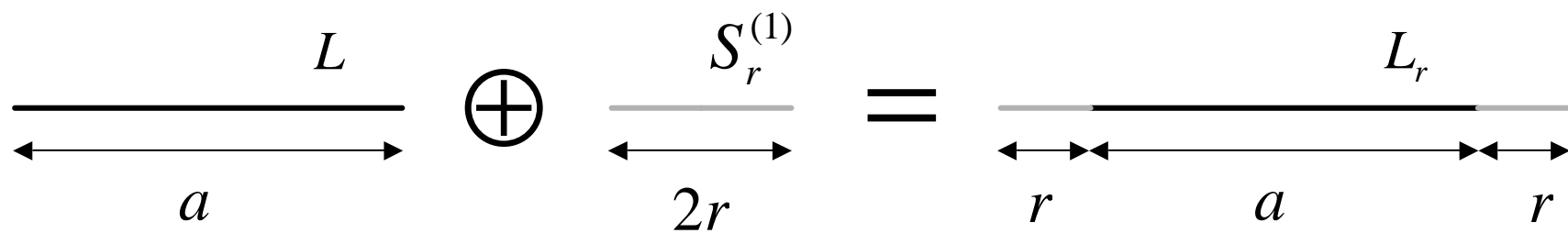




Fig.2

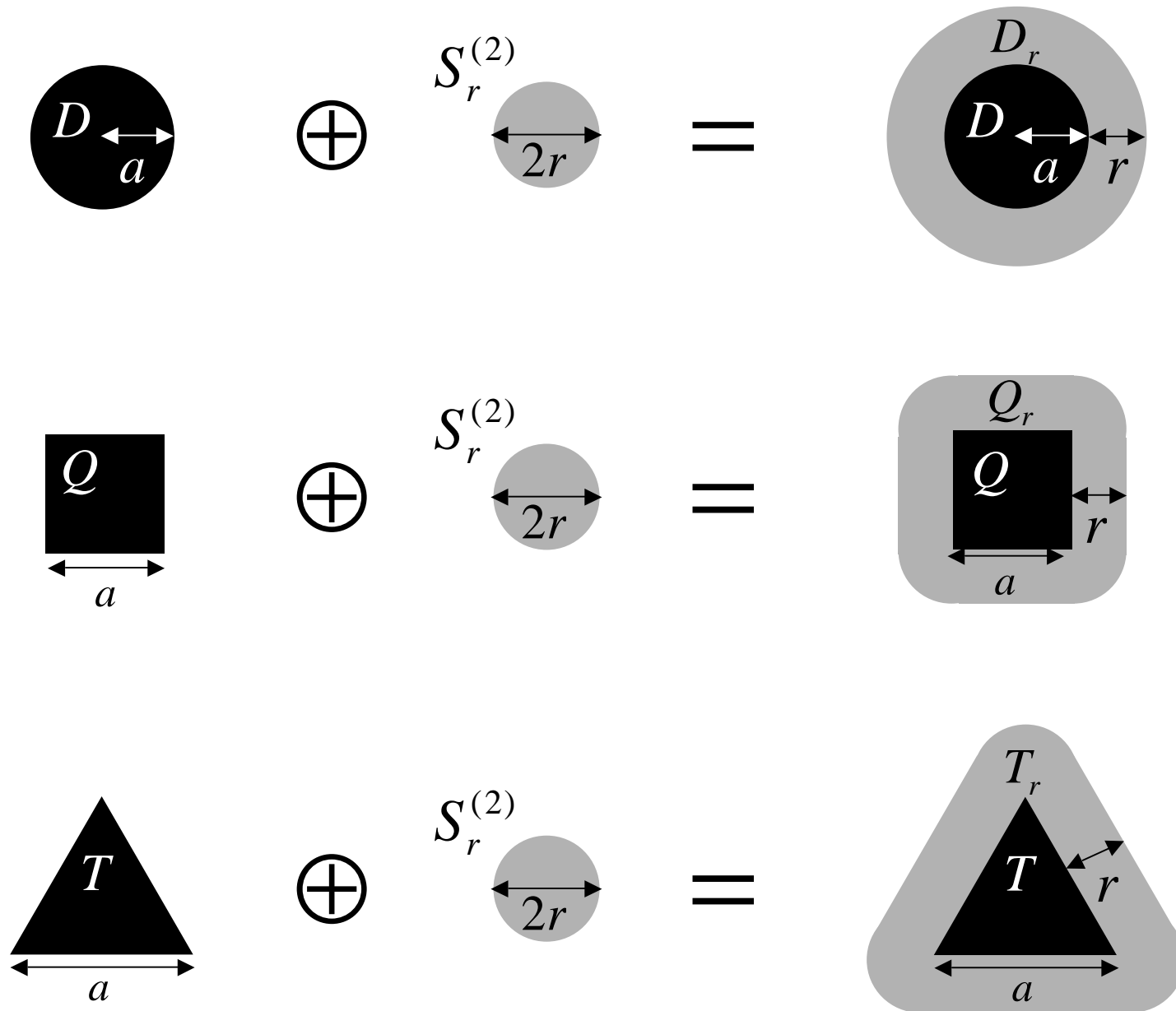
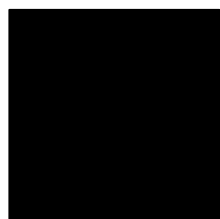
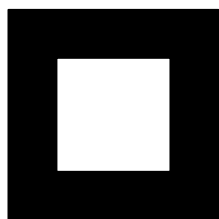


Fig.3

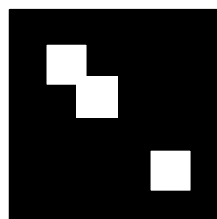
2D



$$\chi = 1$$

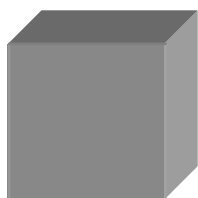


$$\chi = 0$$

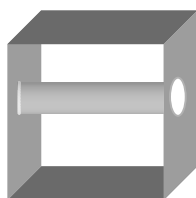


$$\chi = -1$$

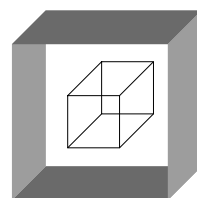
3D



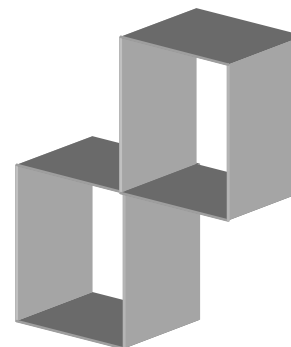
$$\chi = 1$$



$$\chi = 0$$



$$\chi = 2$$



$$\chi = -1$$

Fig.4

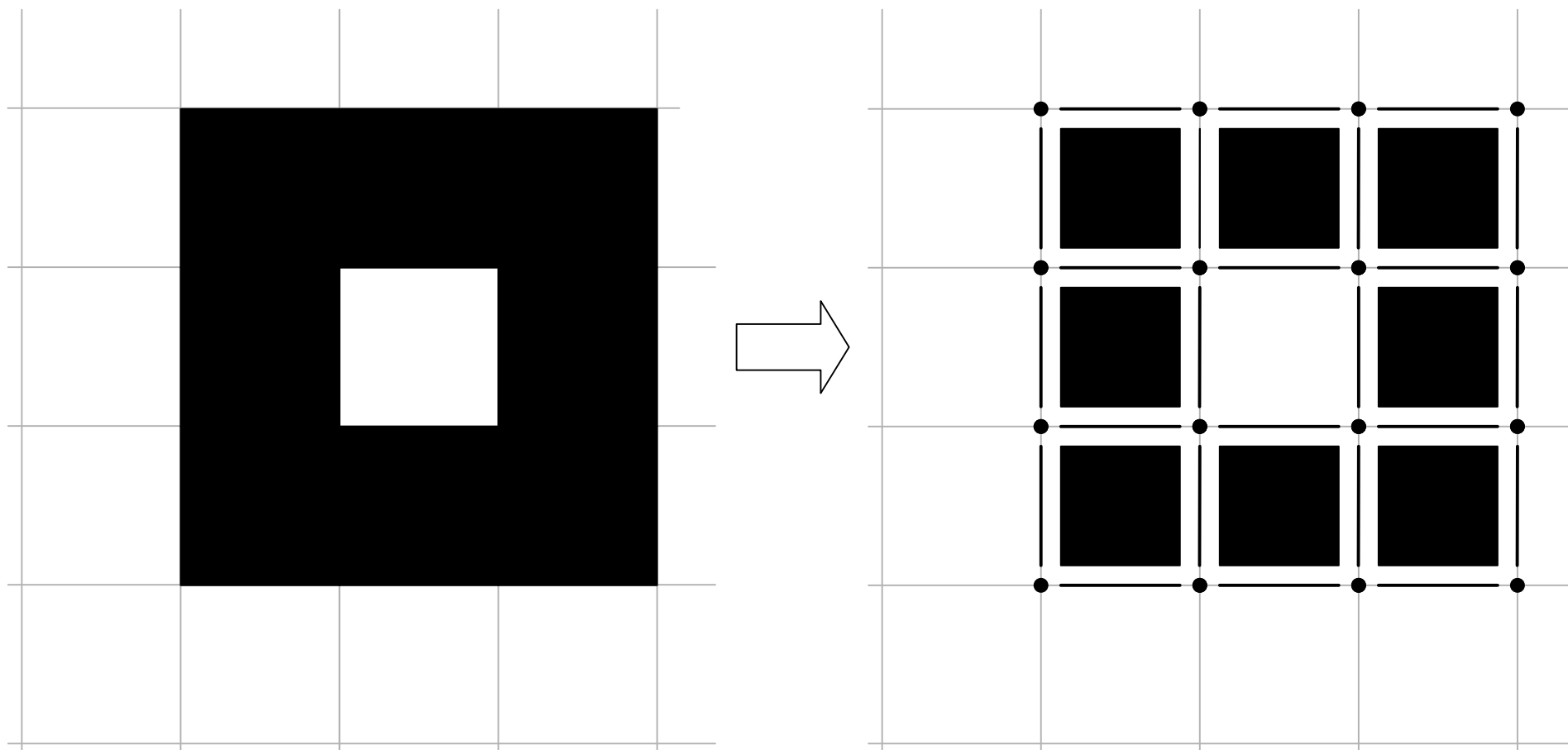


Fig.5

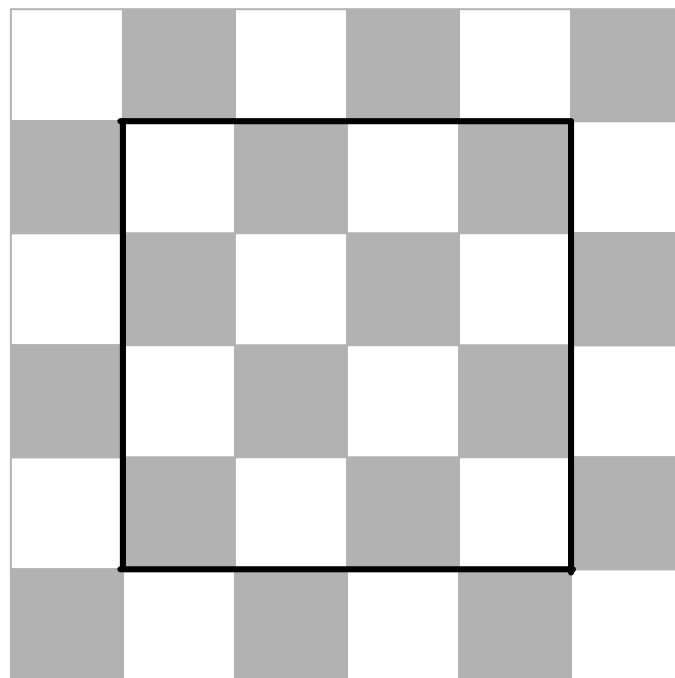
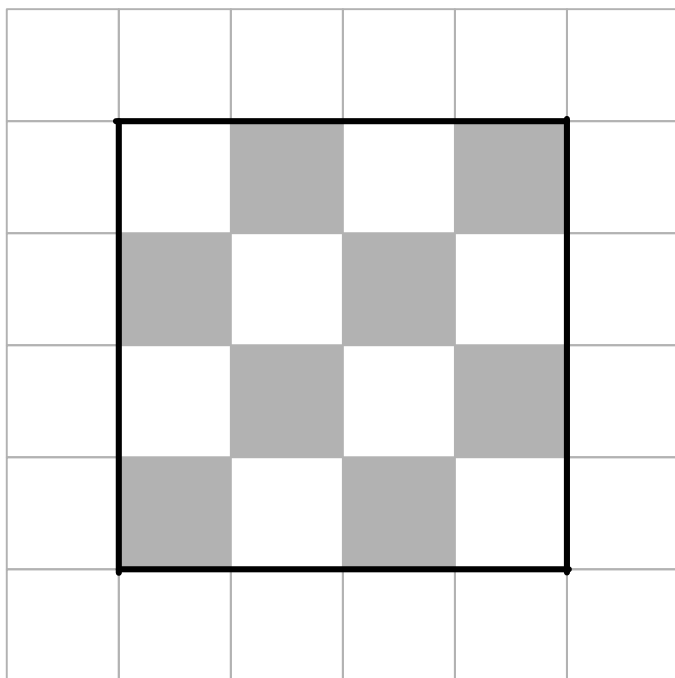


Fig.6

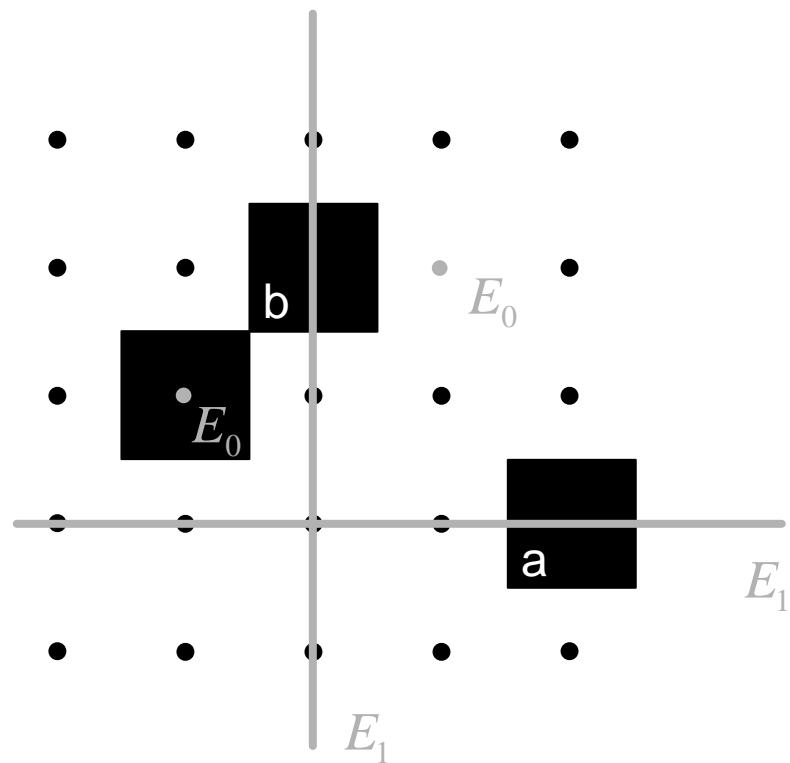


Fig.7

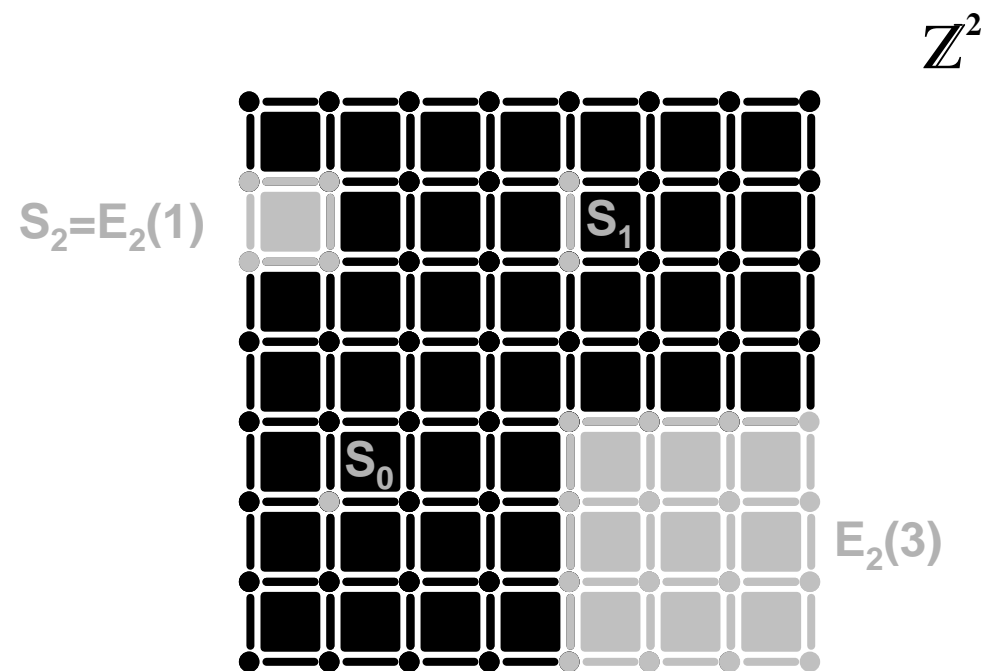


Fig.8

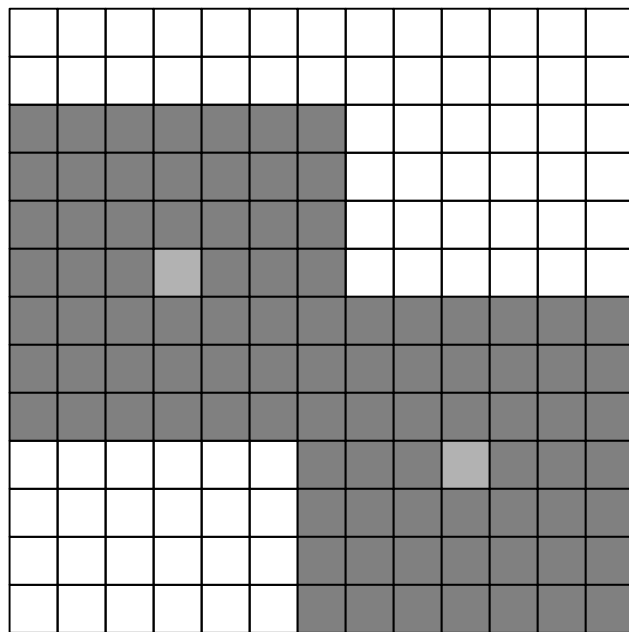
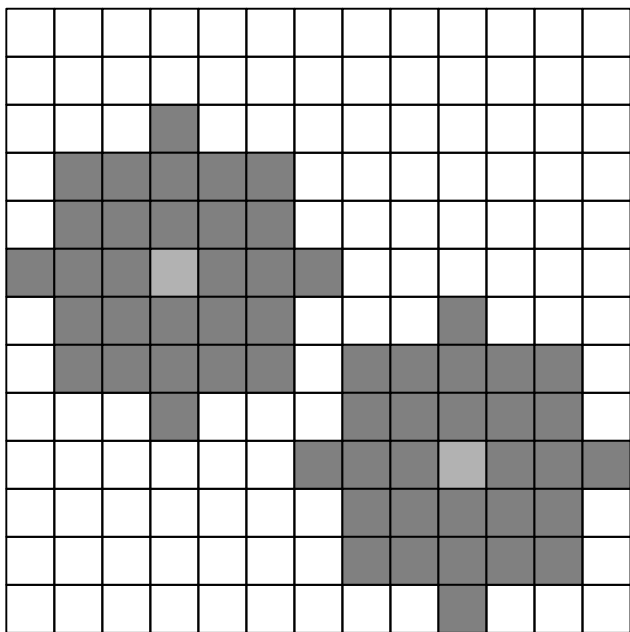


Fig.9

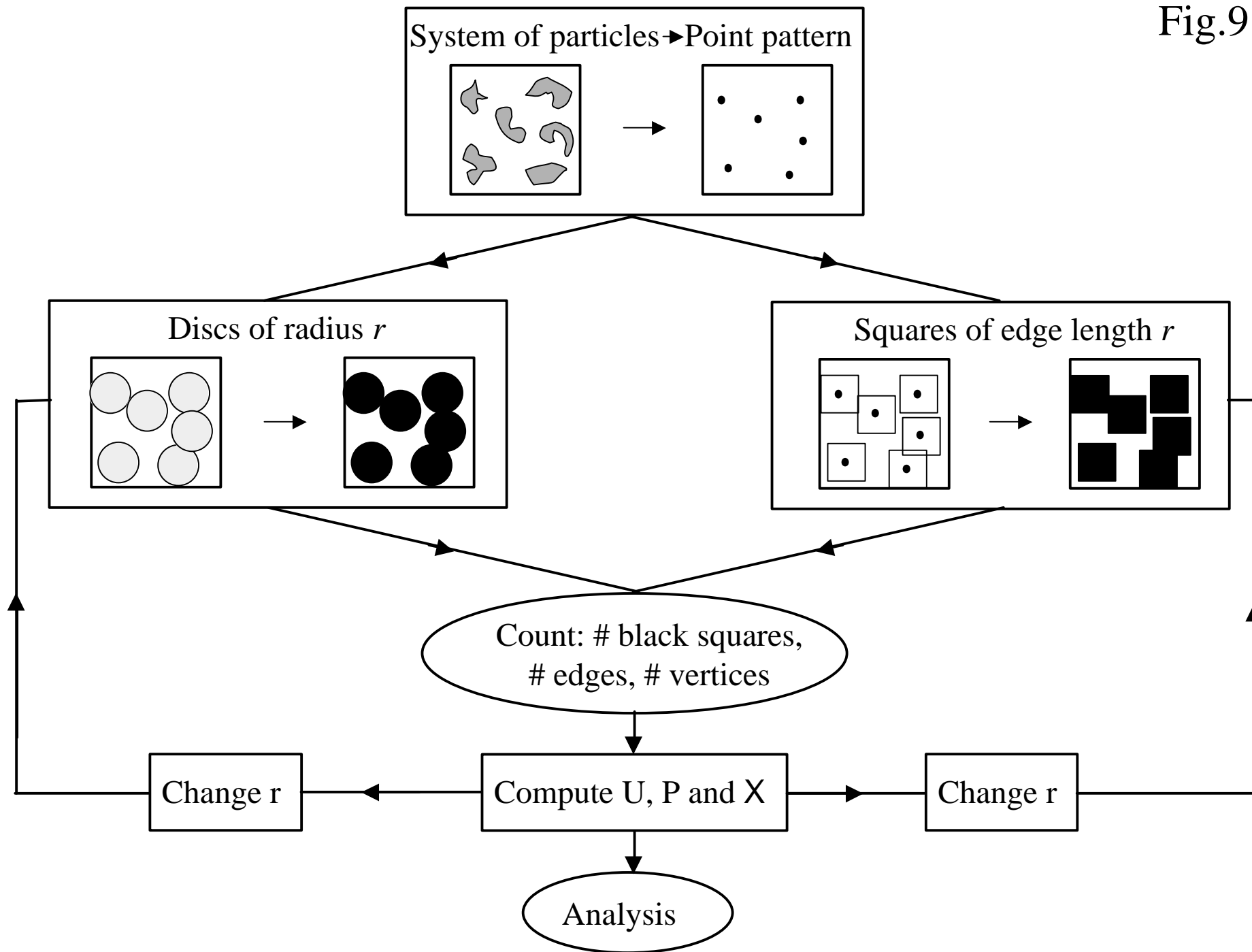




Fig.10

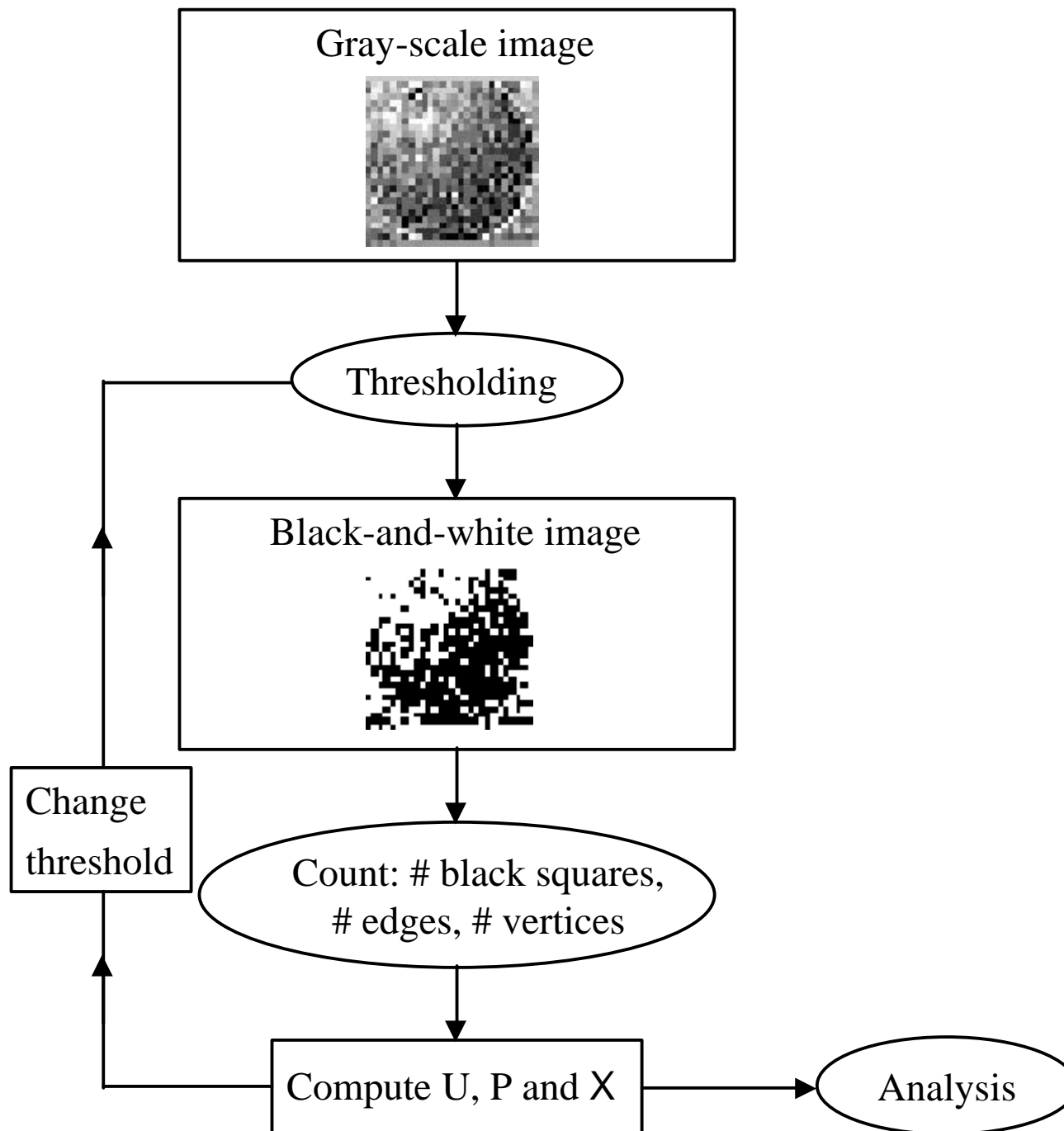


Fig.11

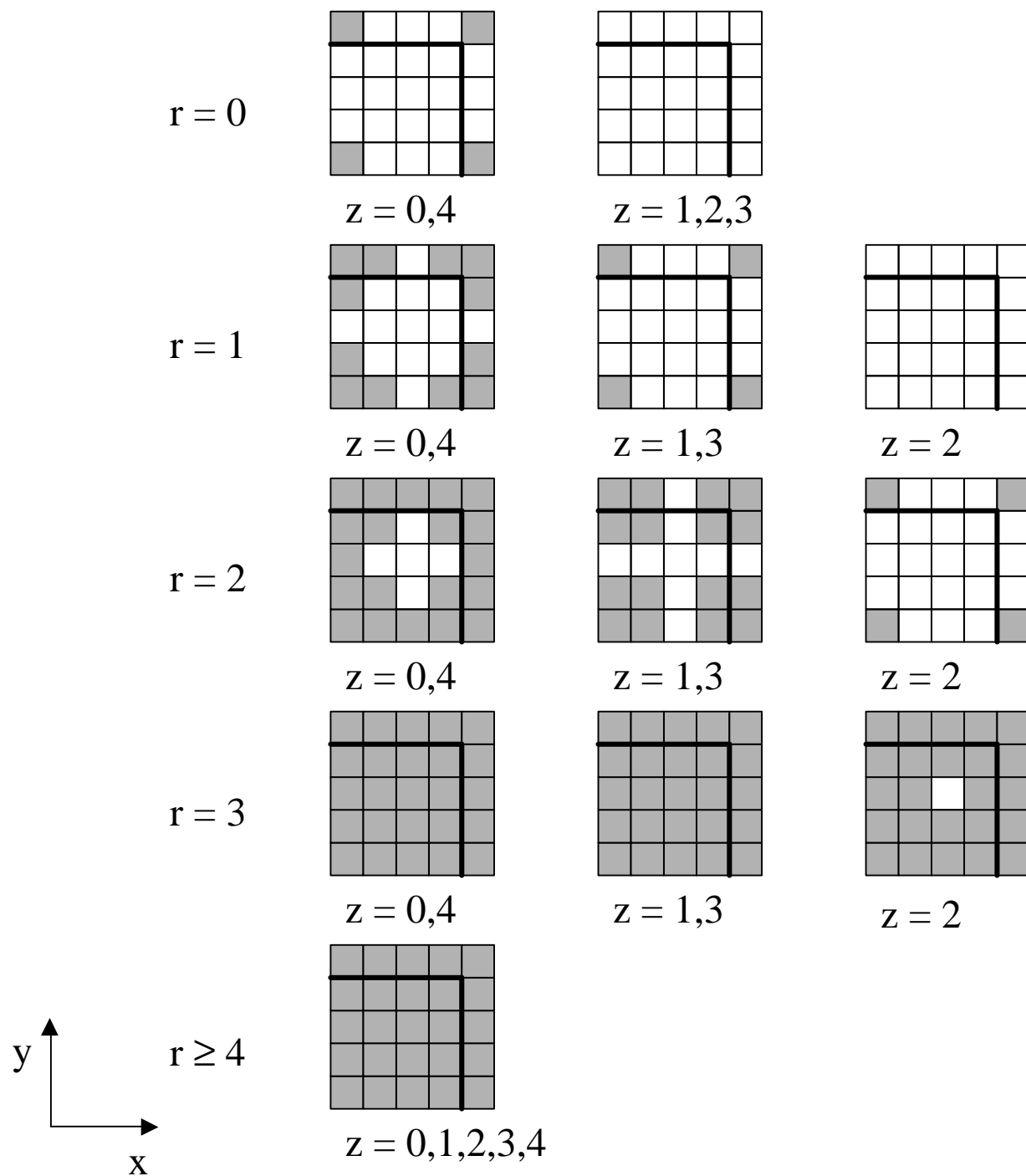


Fig.12

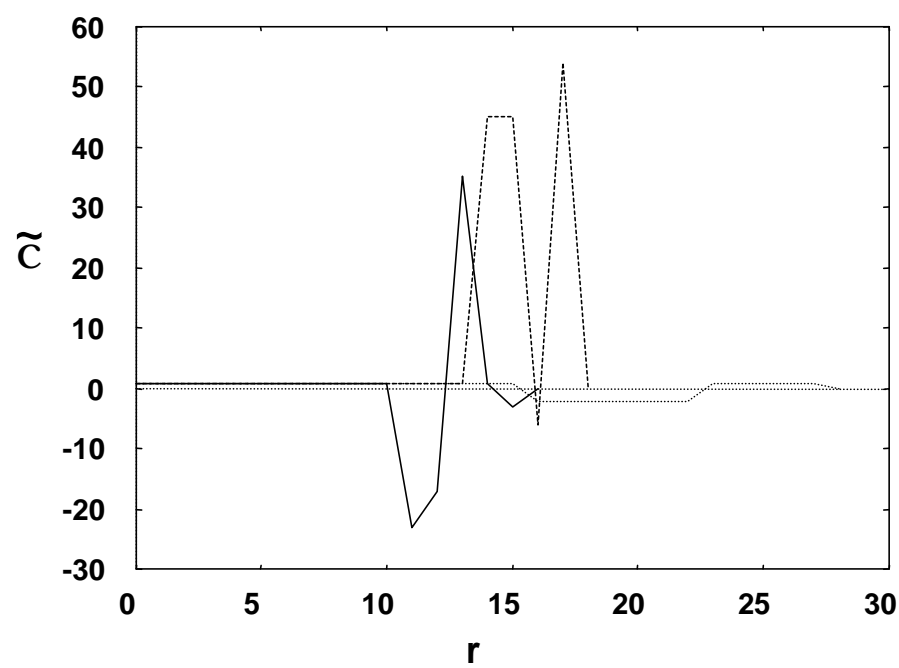
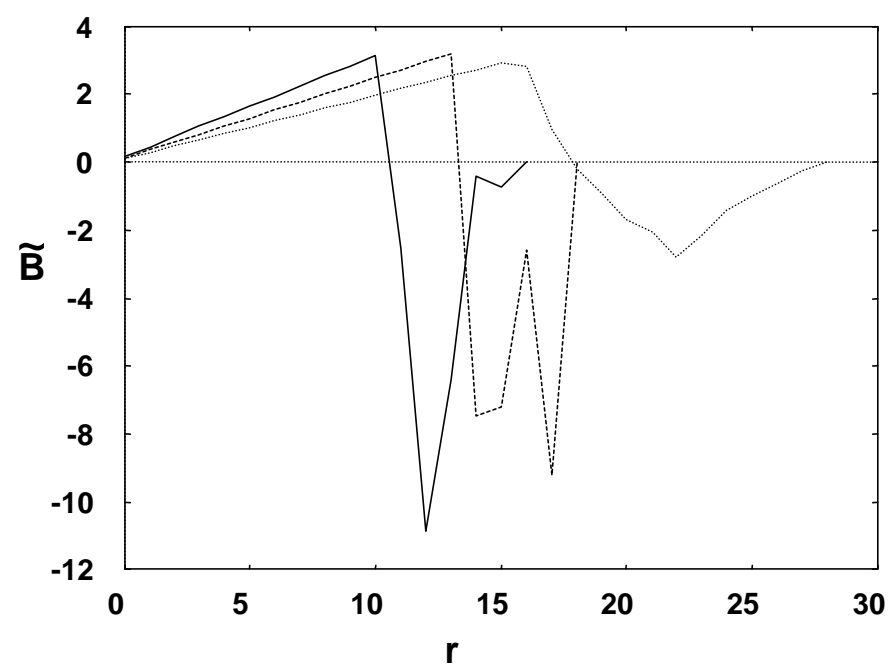
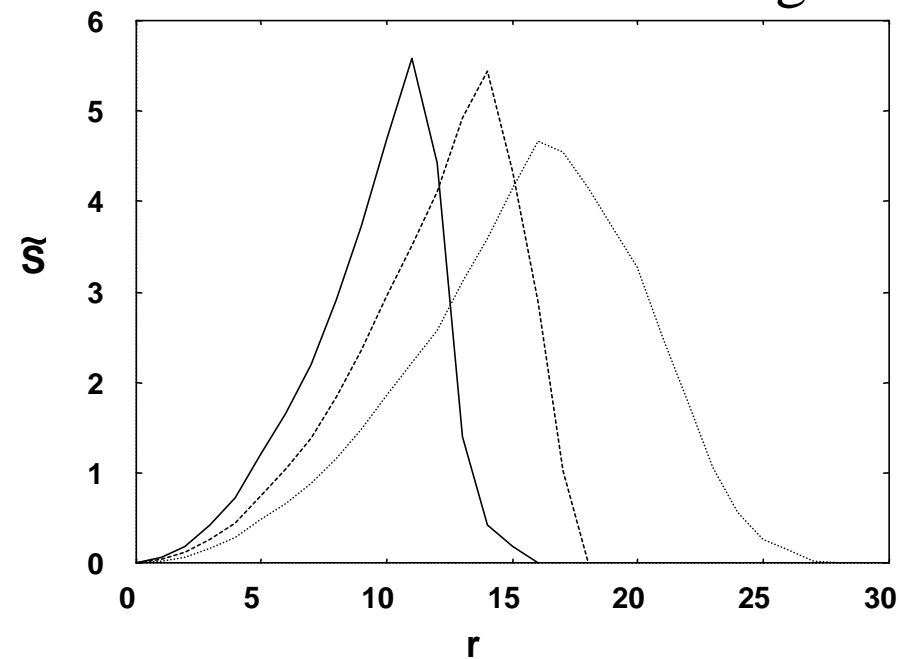
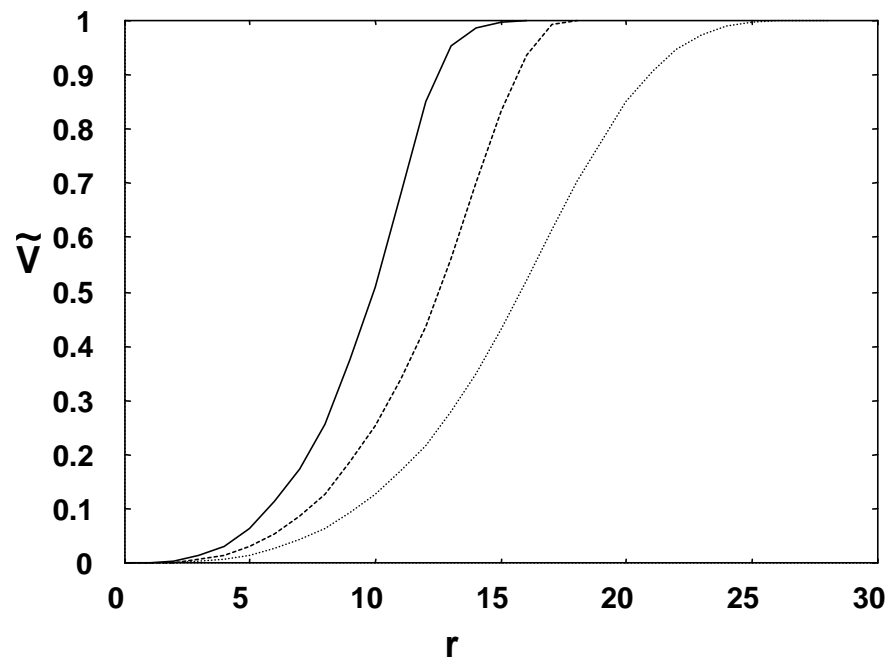


Fig.13

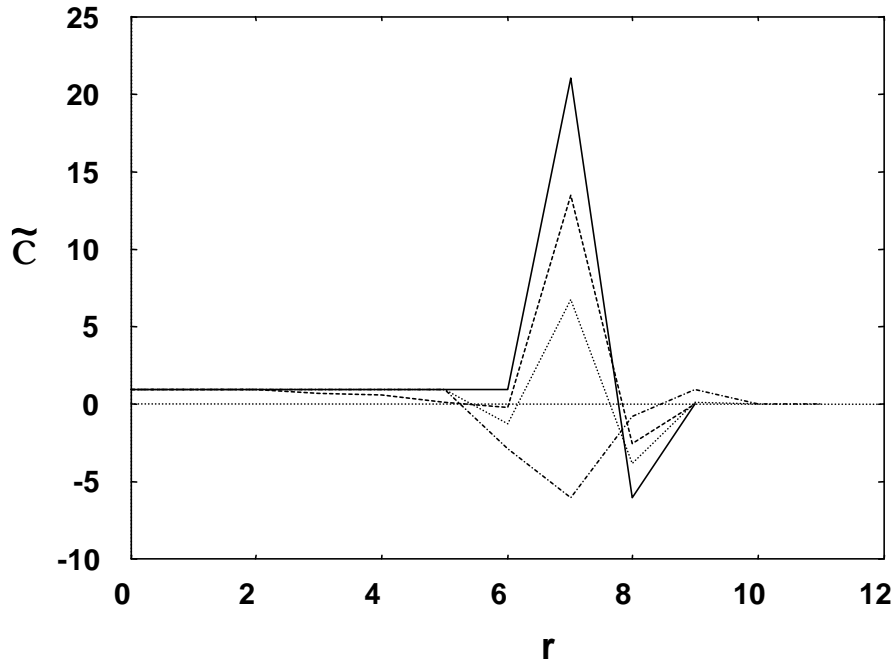
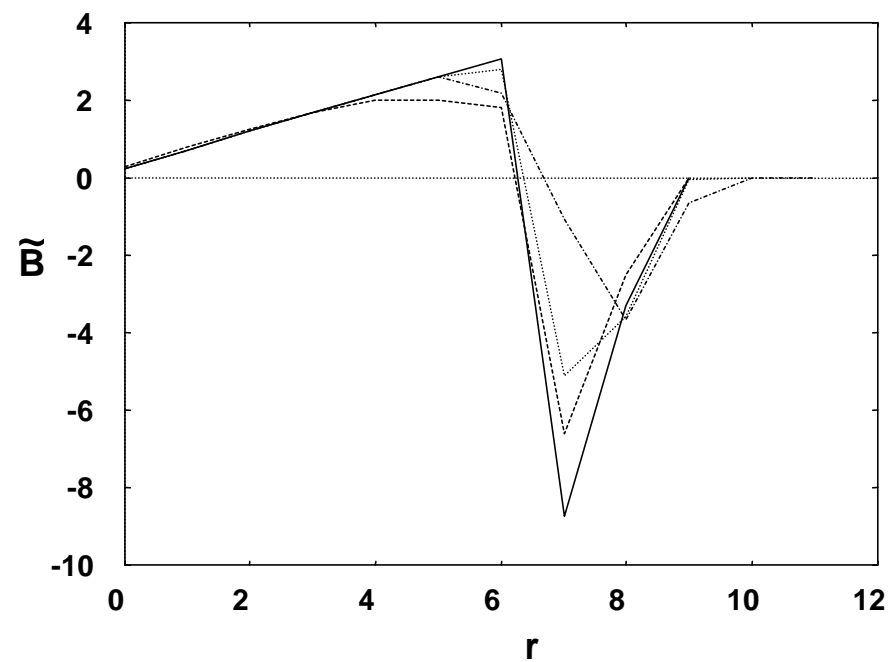
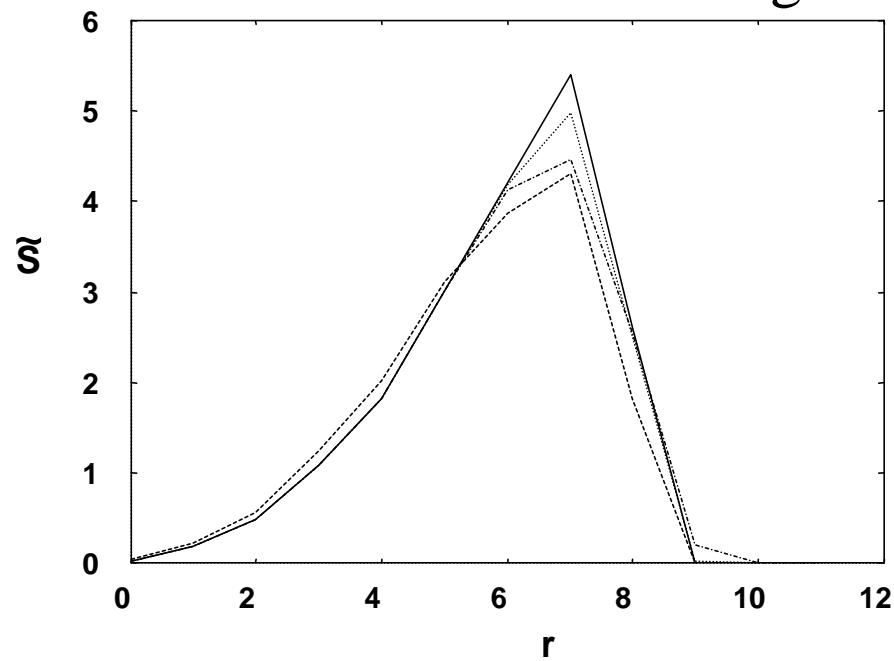
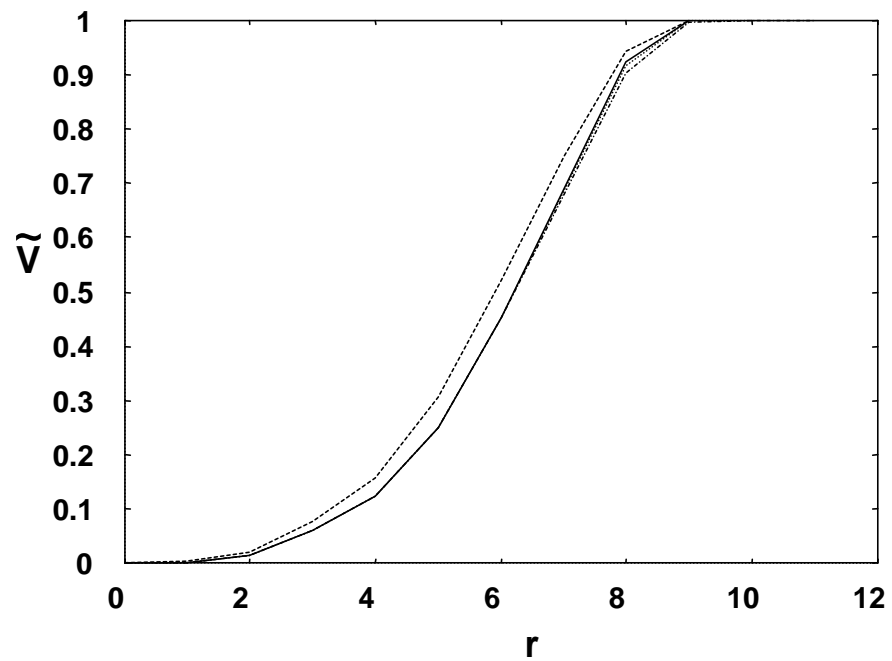


Fig.14

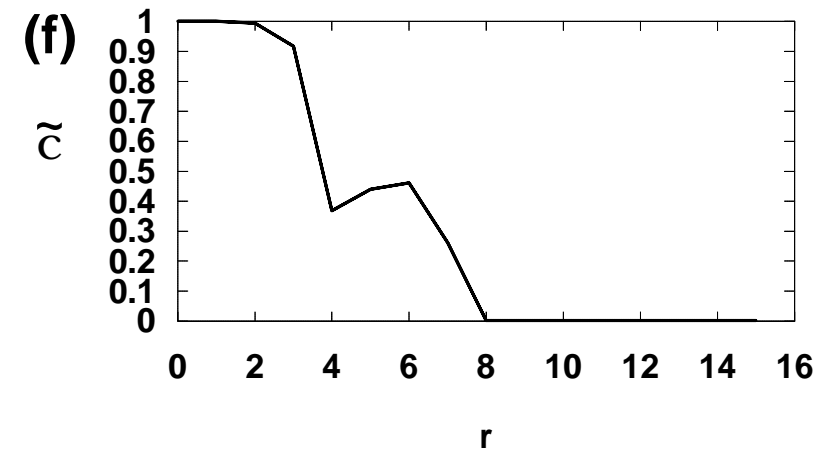
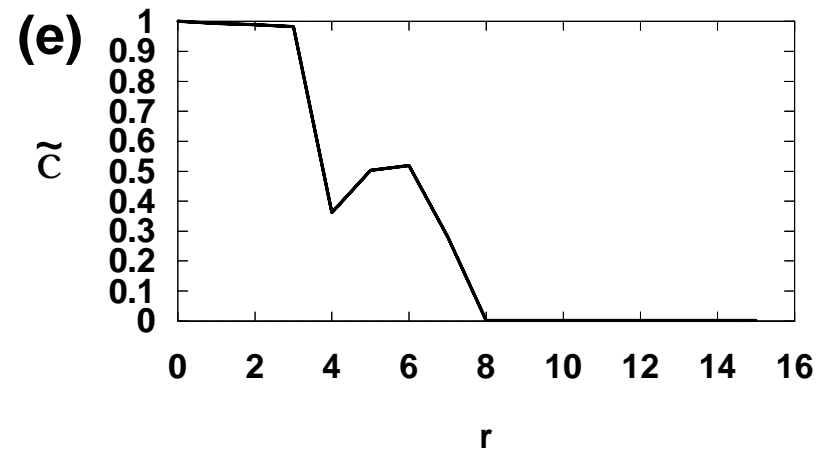
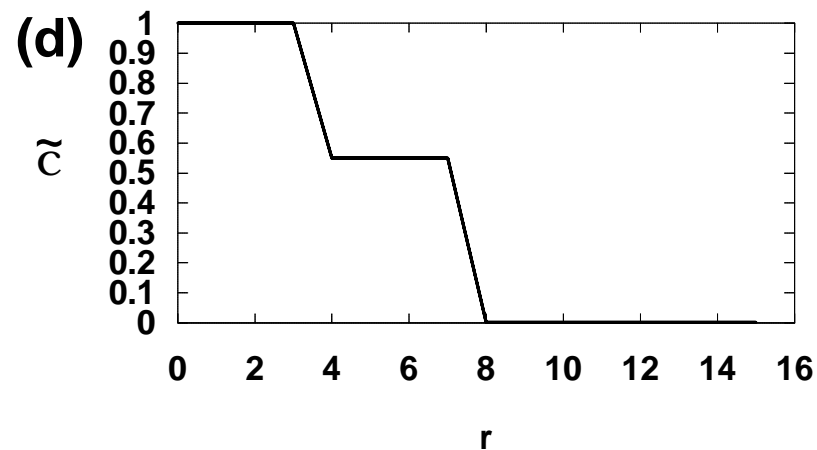
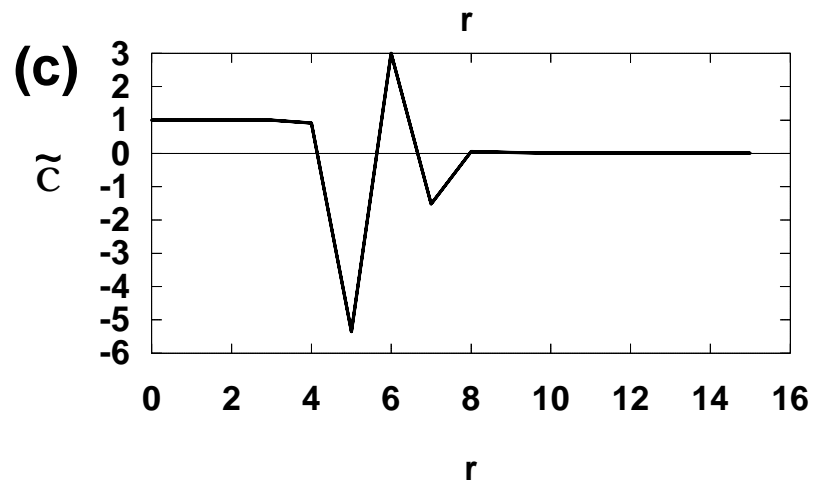
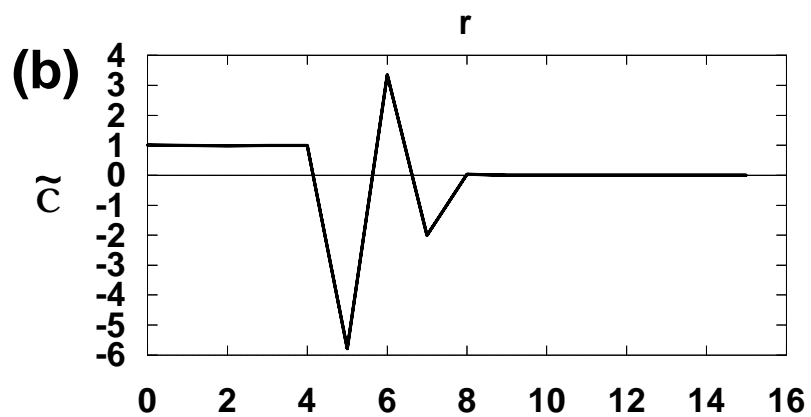
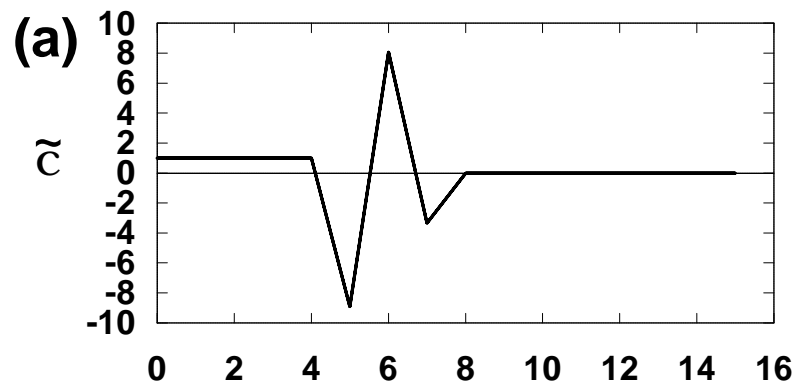


Fig.15

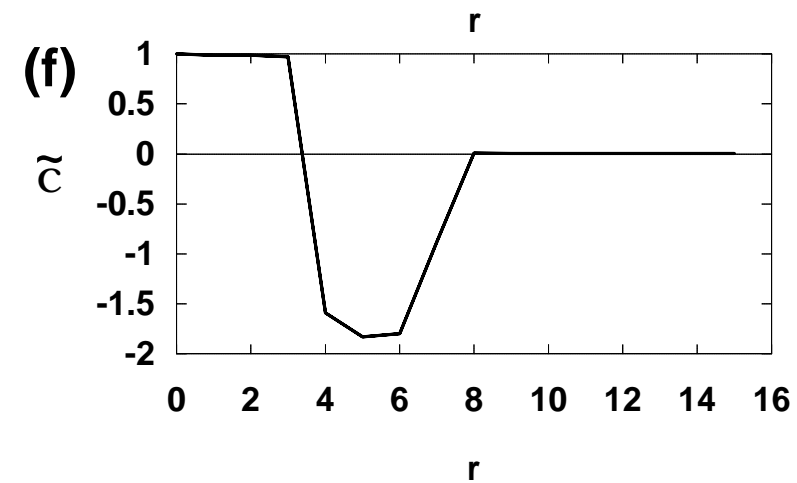
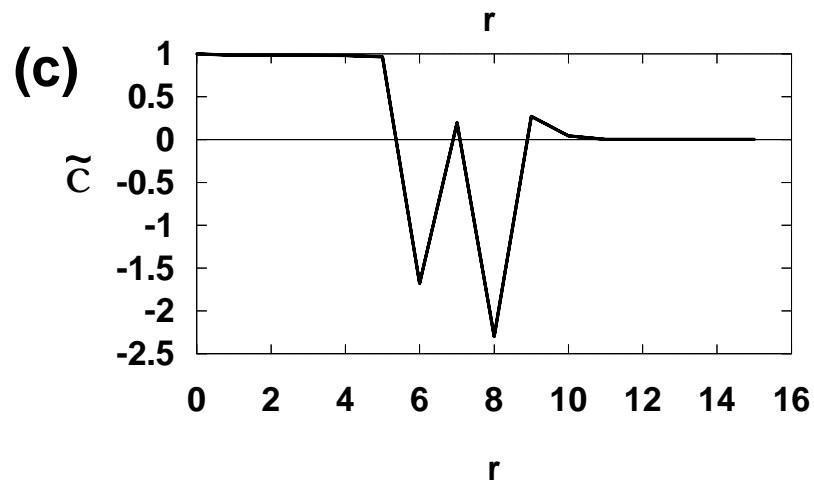
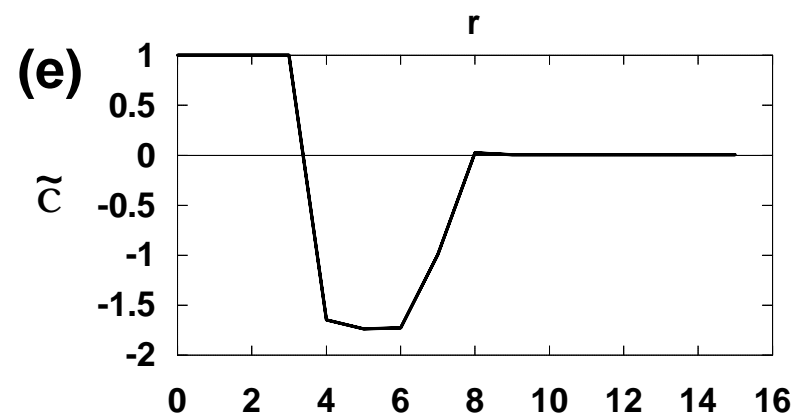
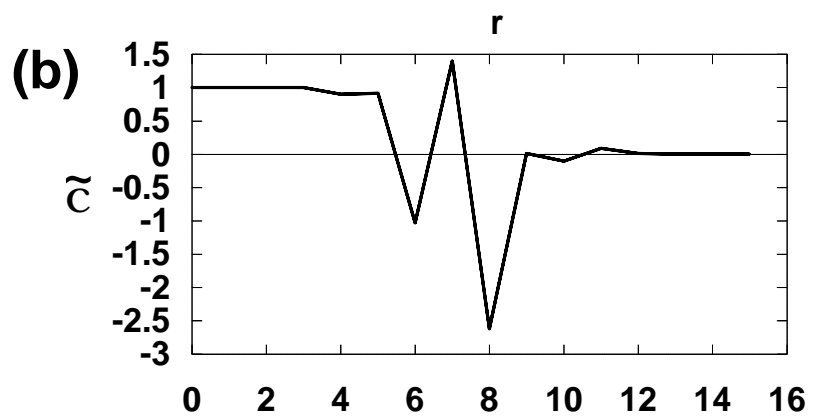
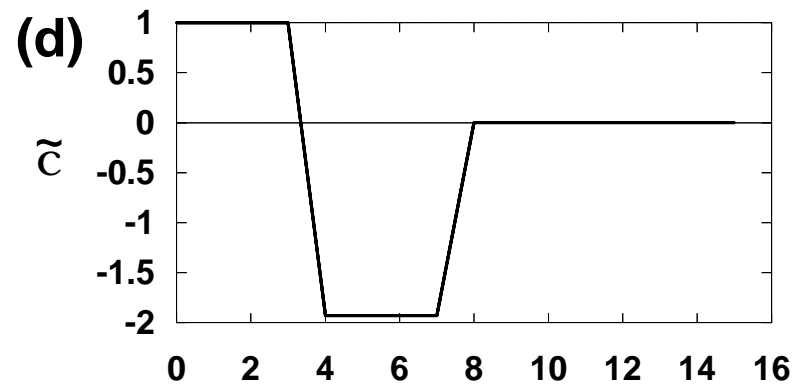
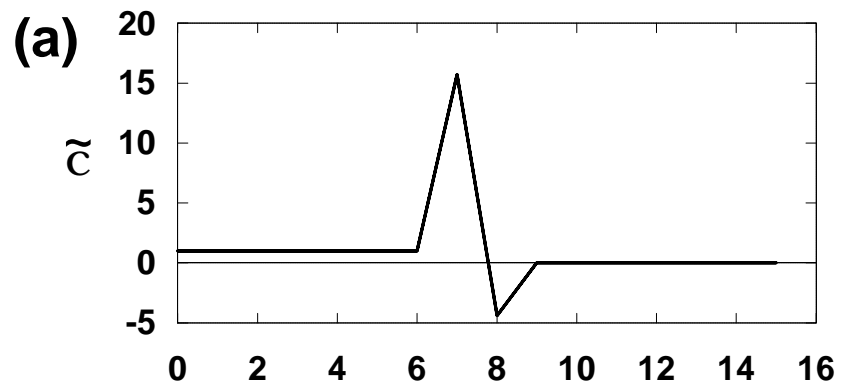


Fig.16

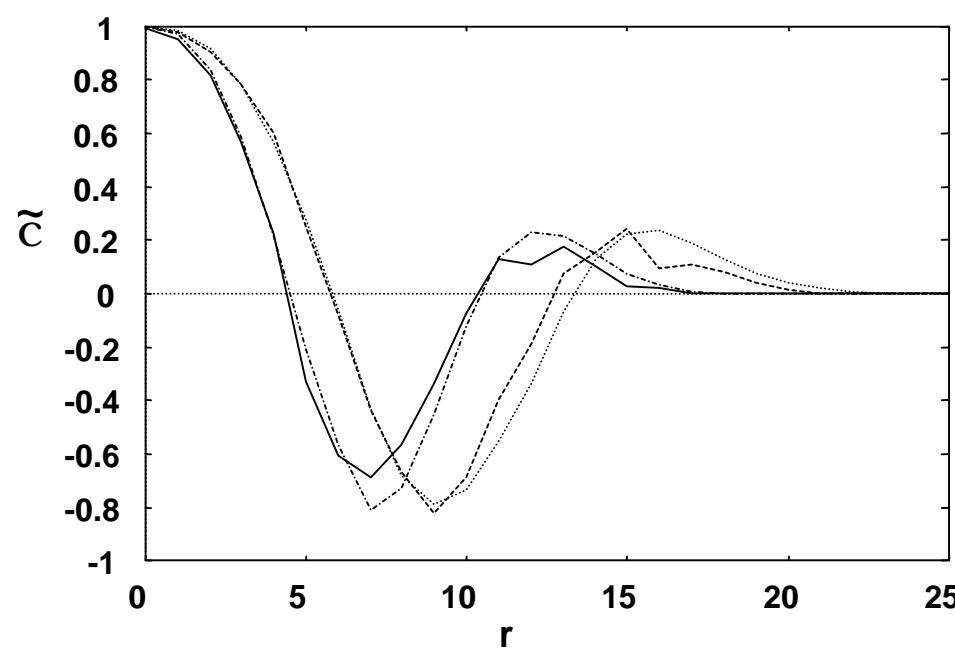
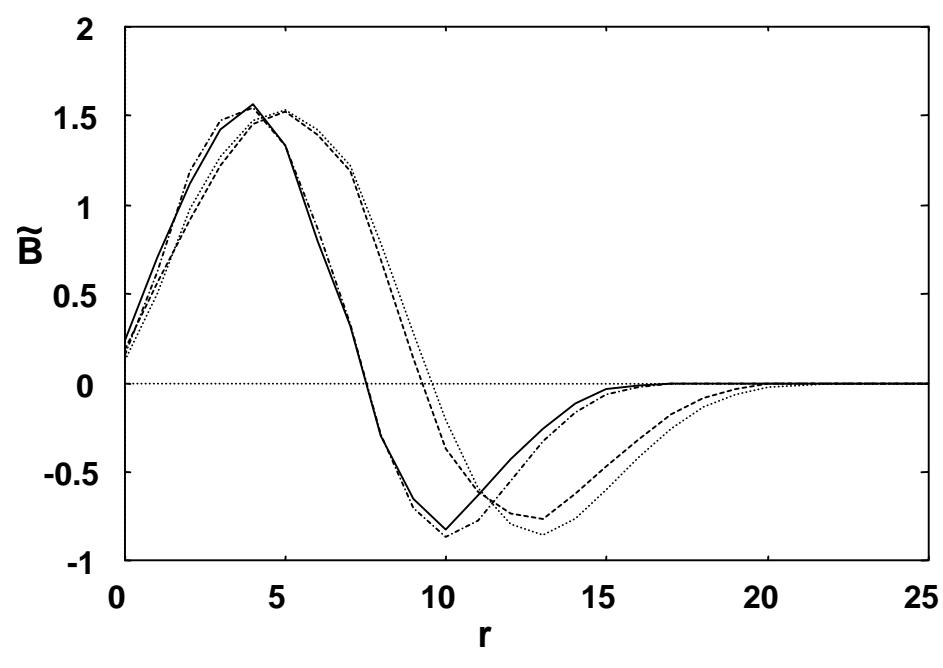
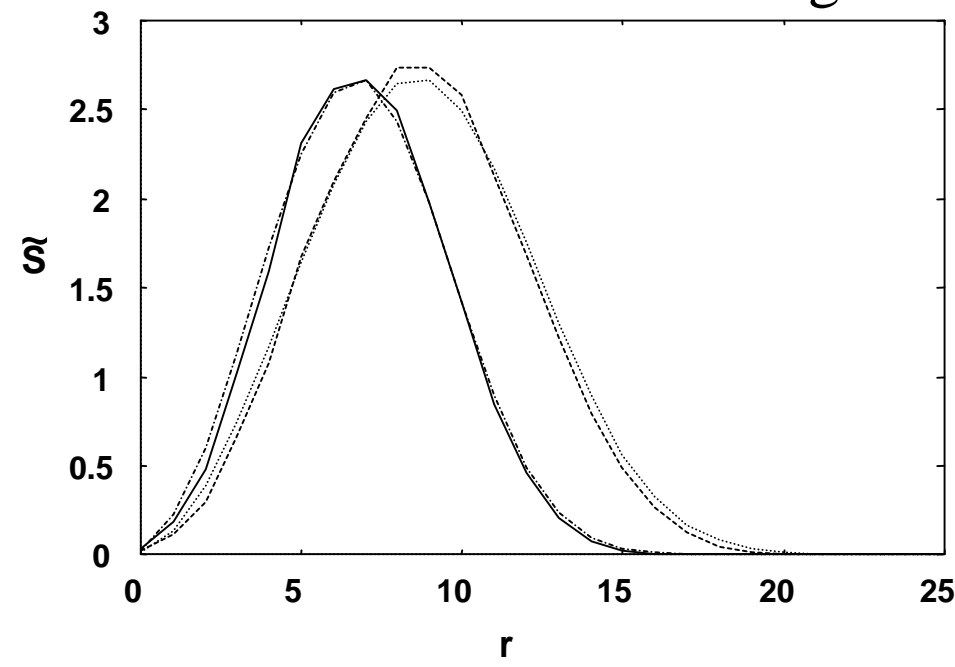
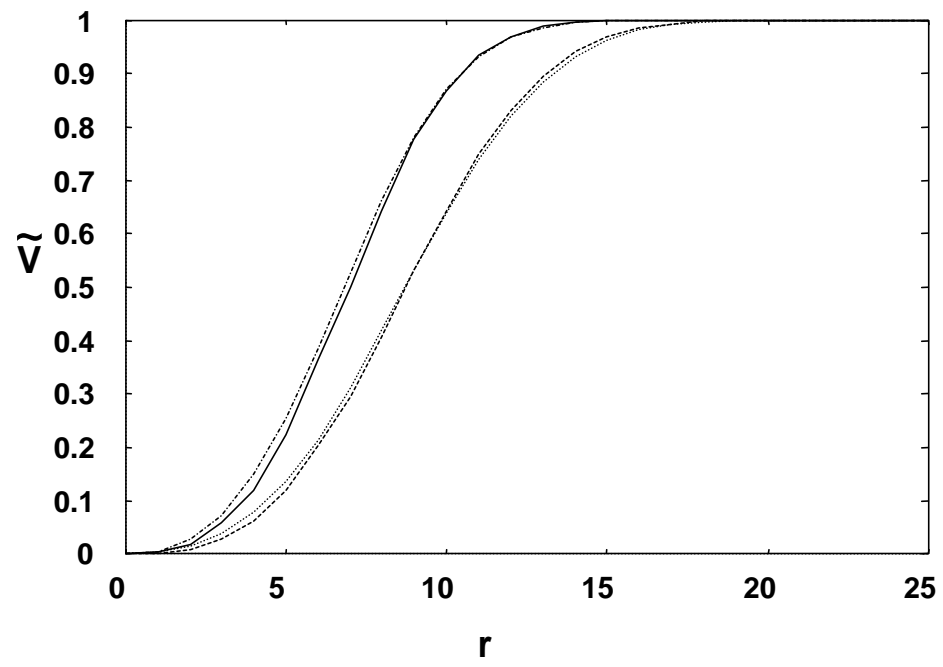


Fig.17

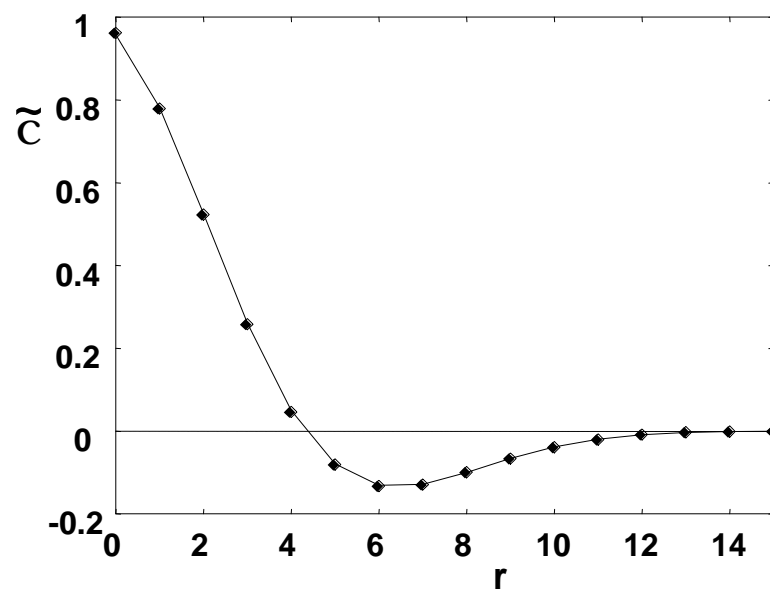
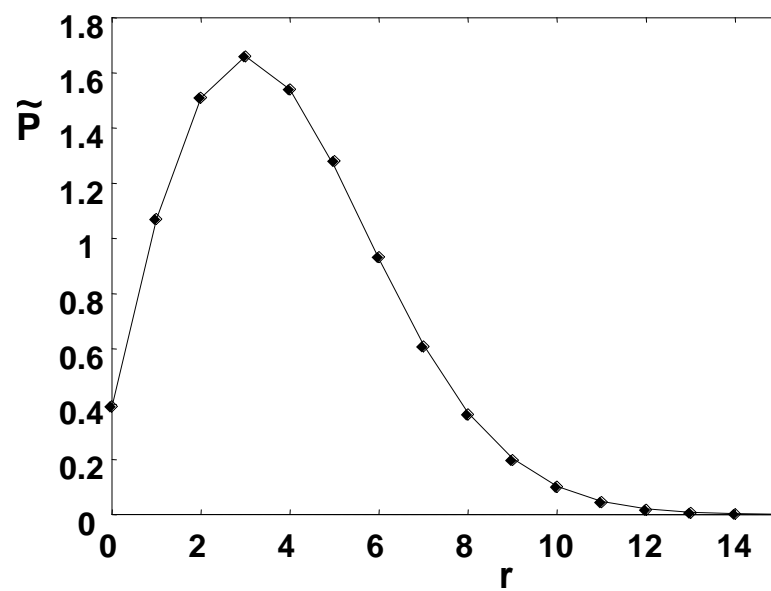
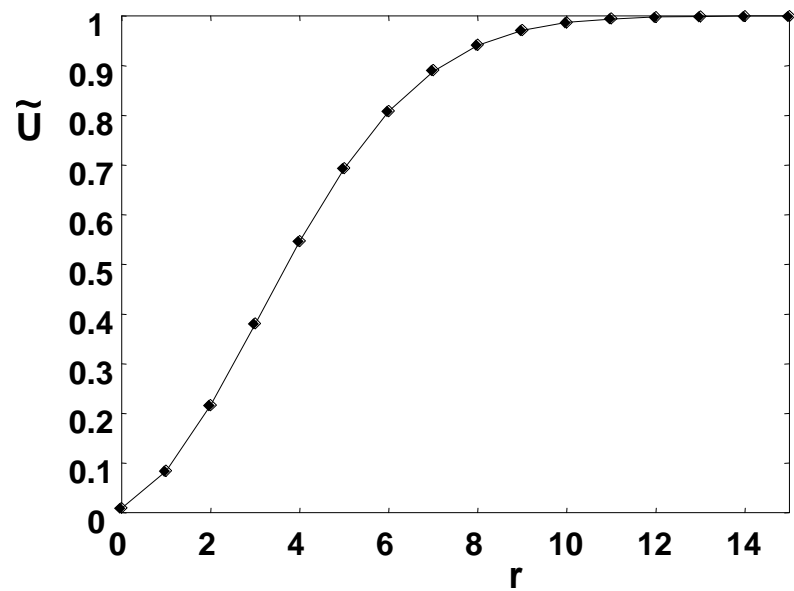




Fig.18

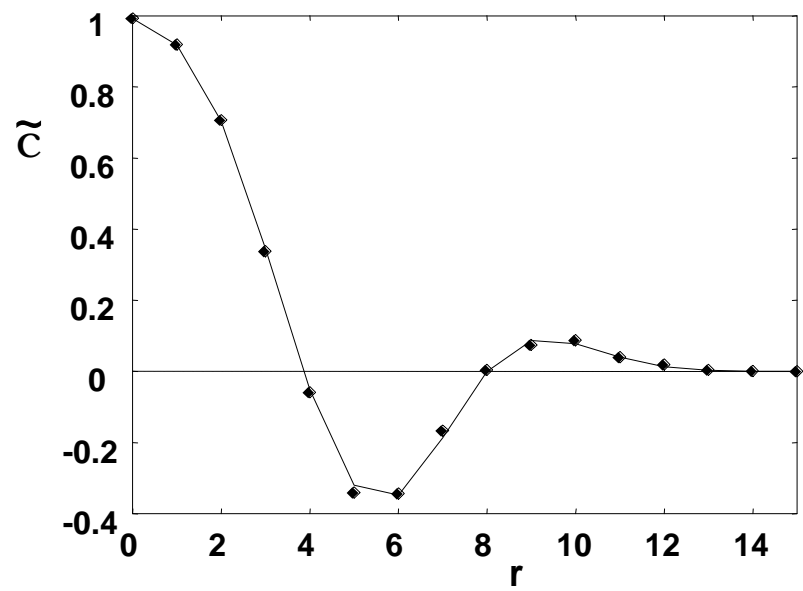
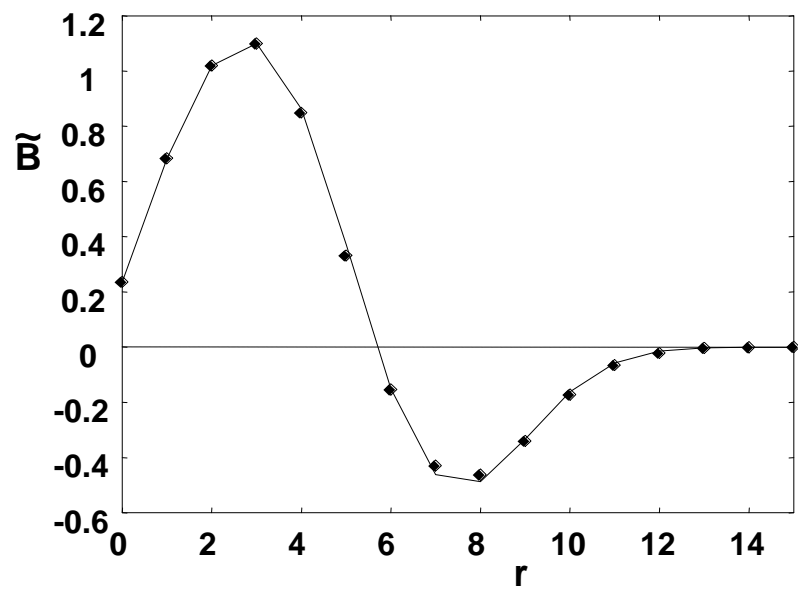
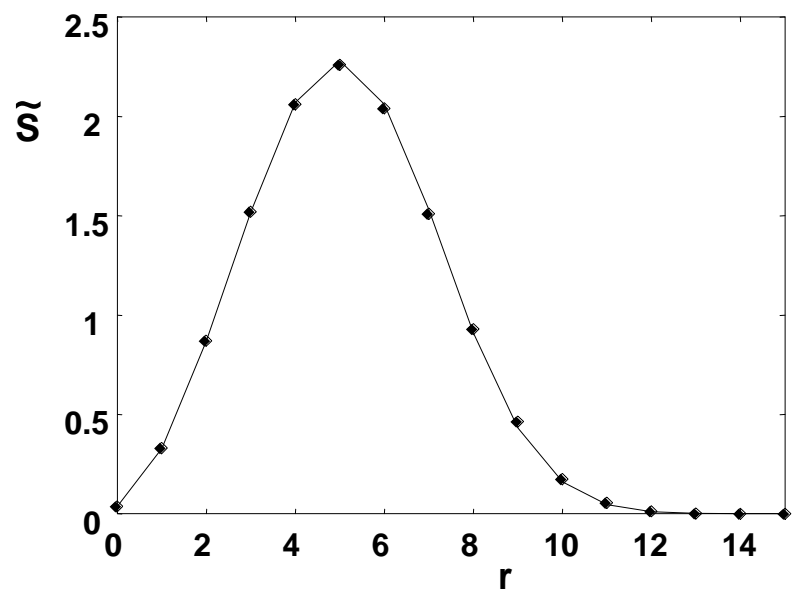
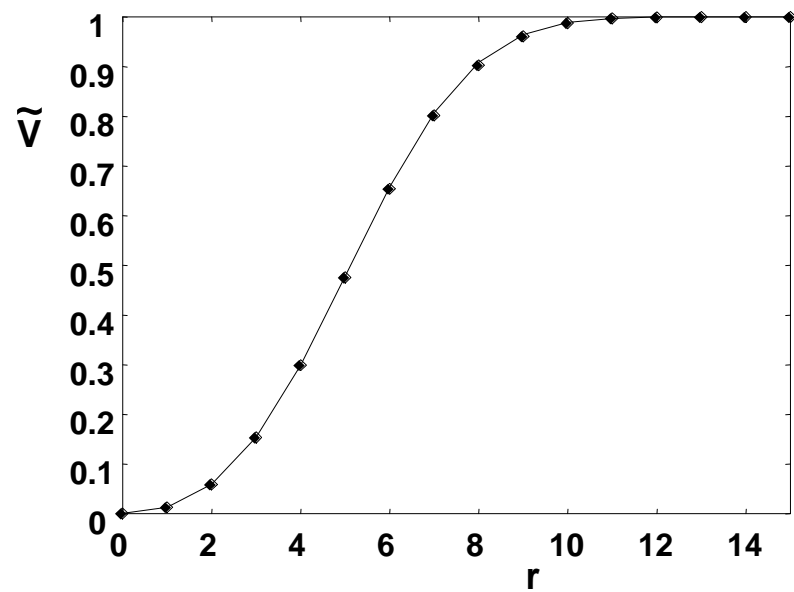
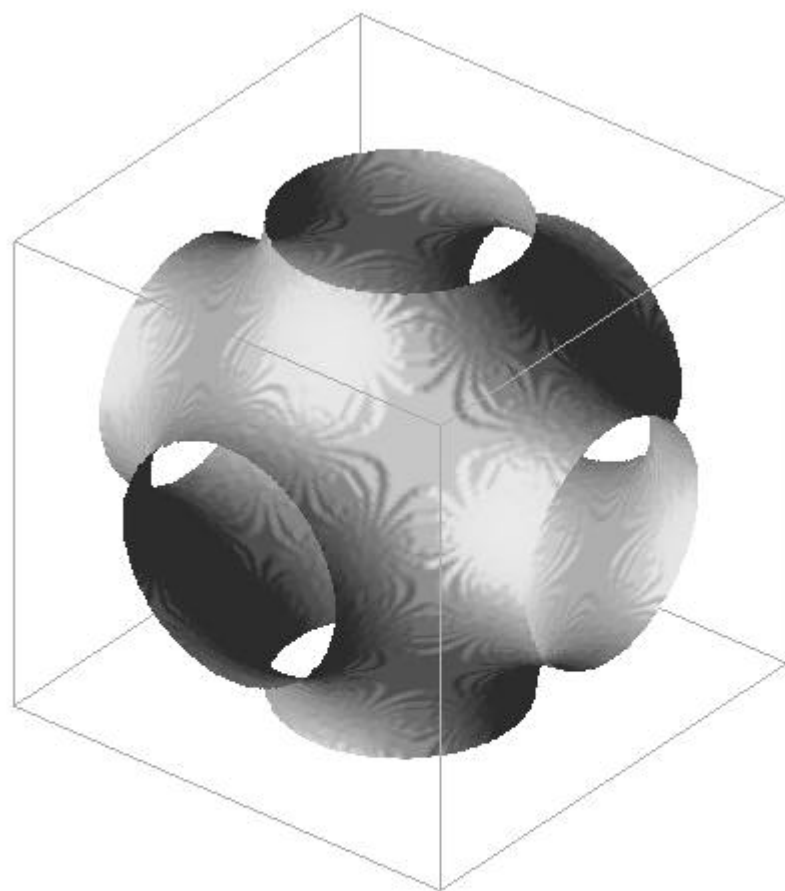
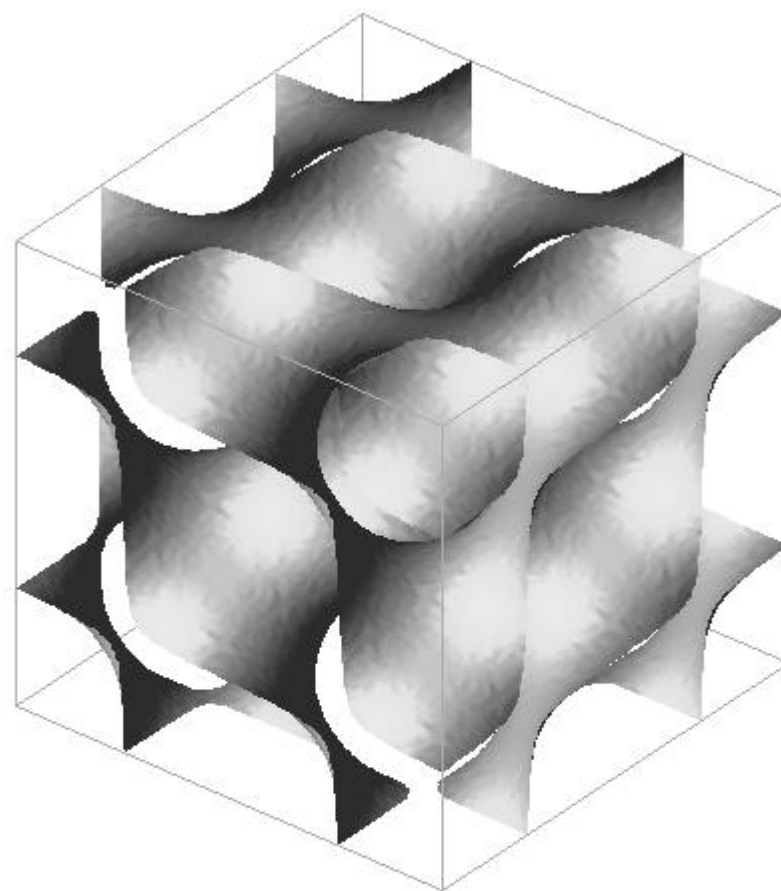


Fig.19

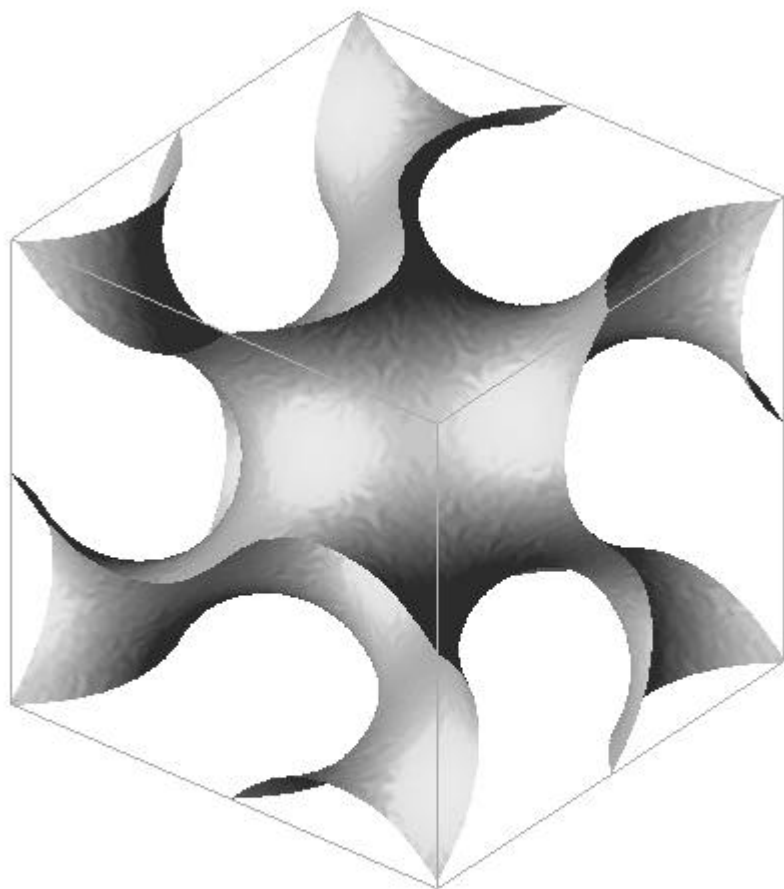


**(a)**

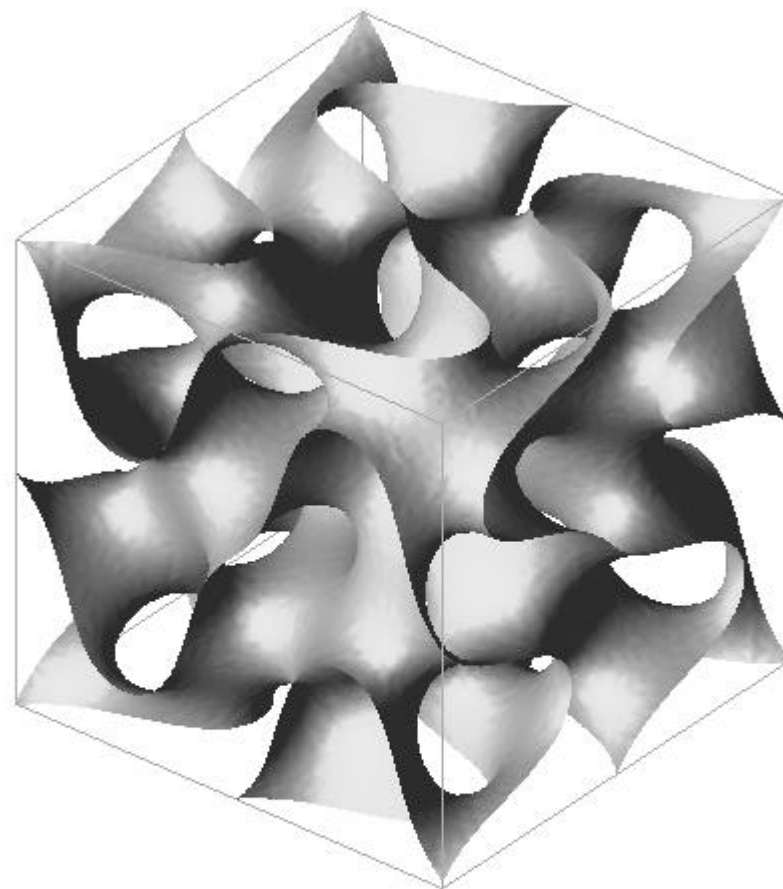


**(b)**

Fig.20

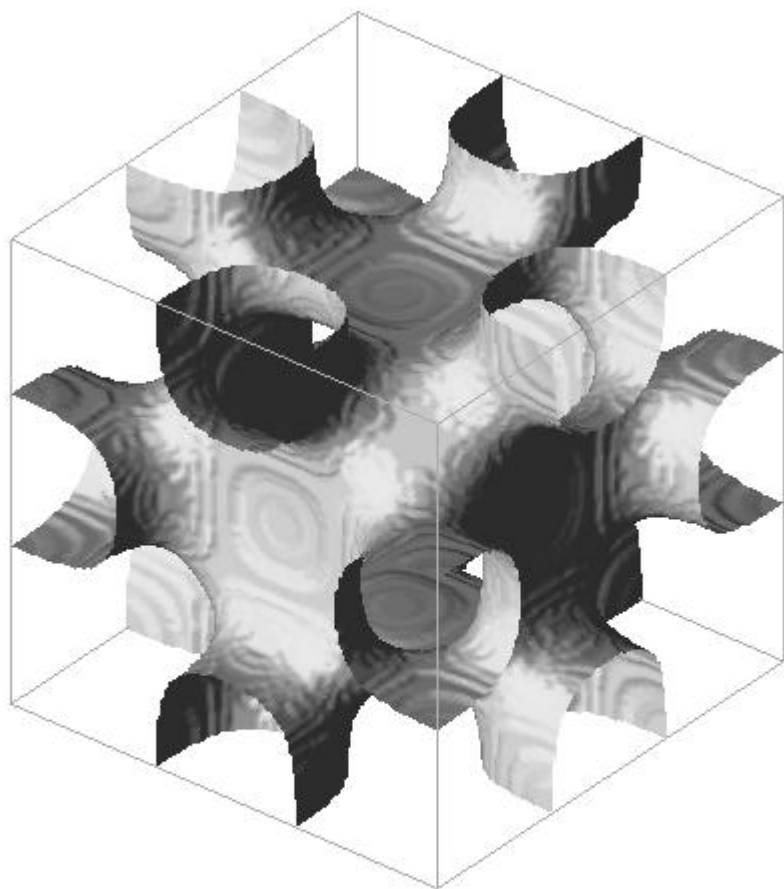


**(a)**

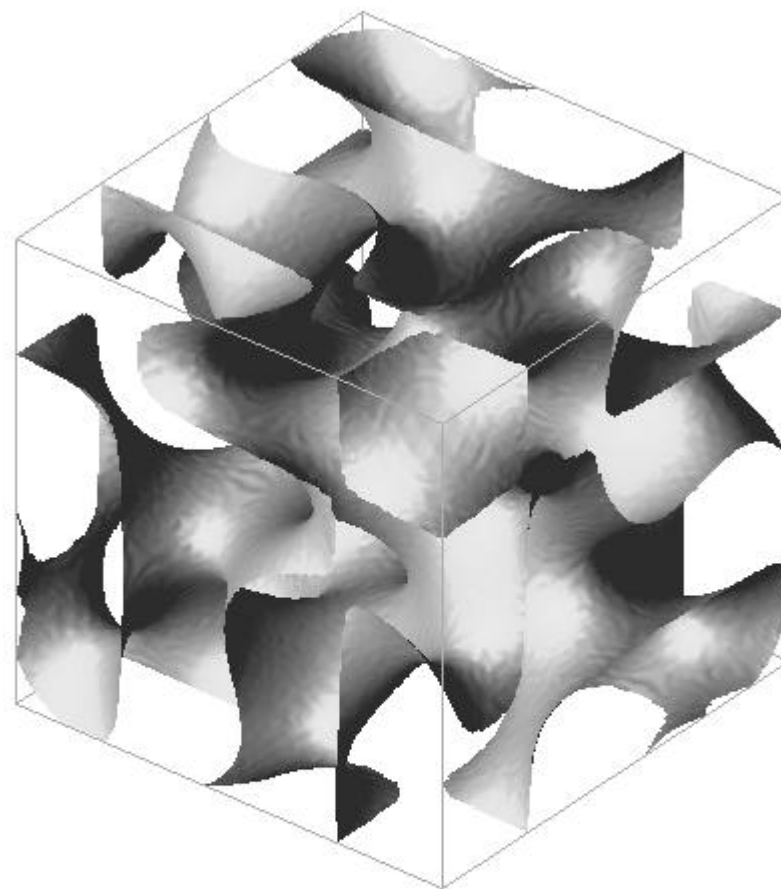


**(b)**

Fig.21

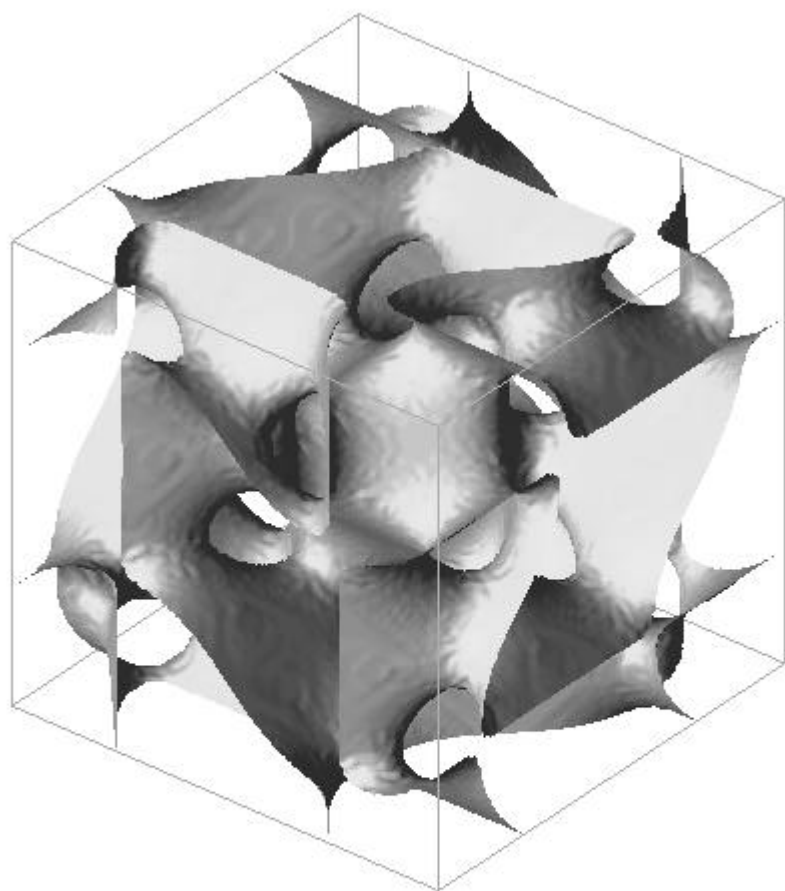


**(a)**

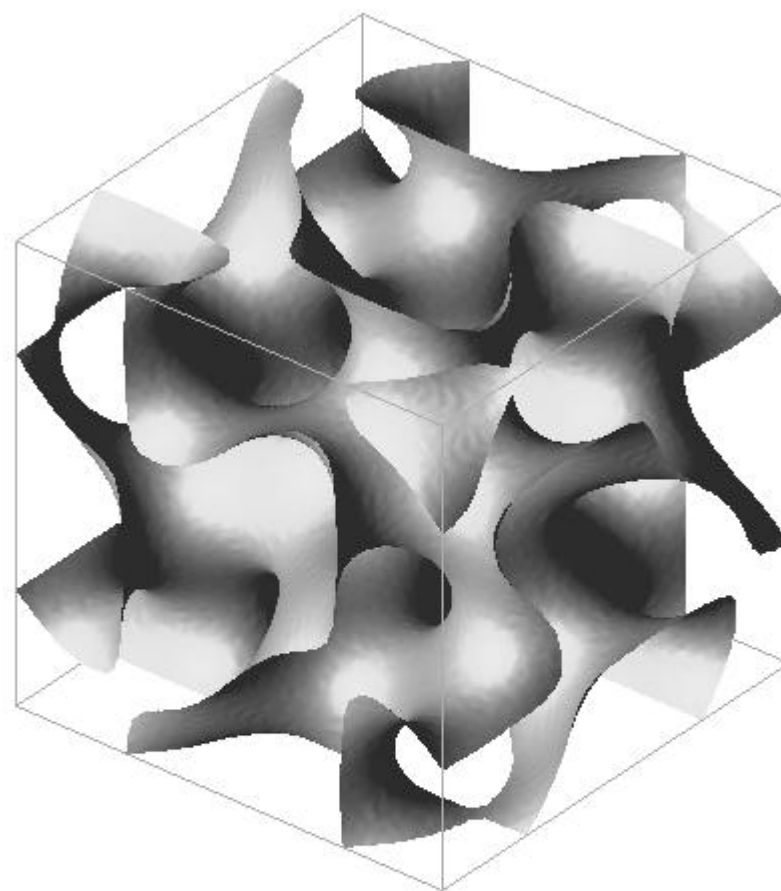


**(b)**

Fig.22

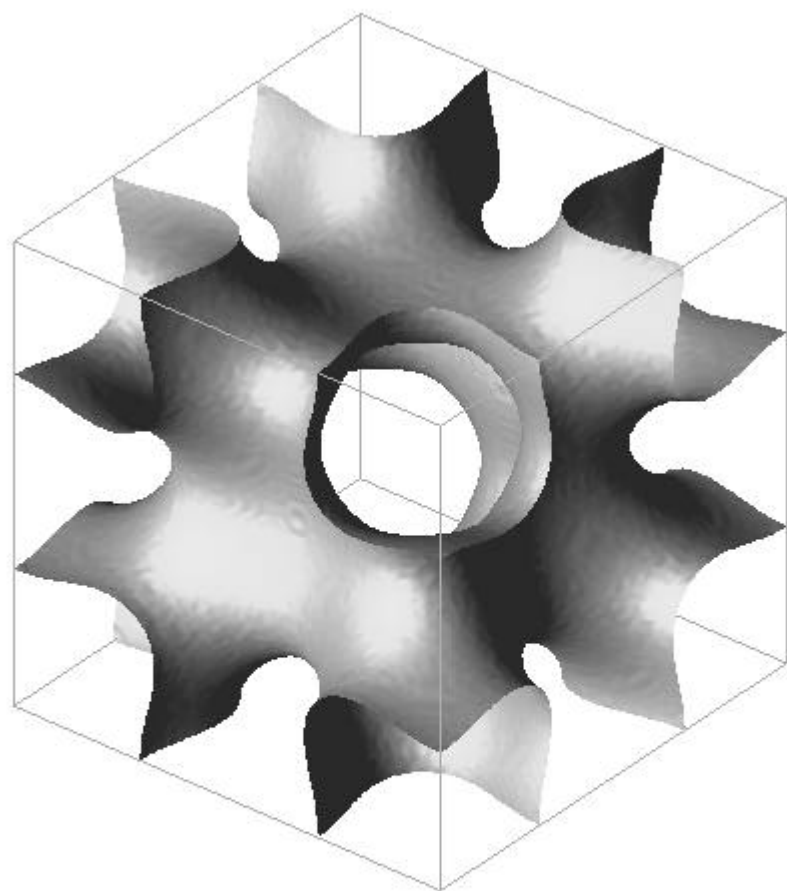


**(a)**

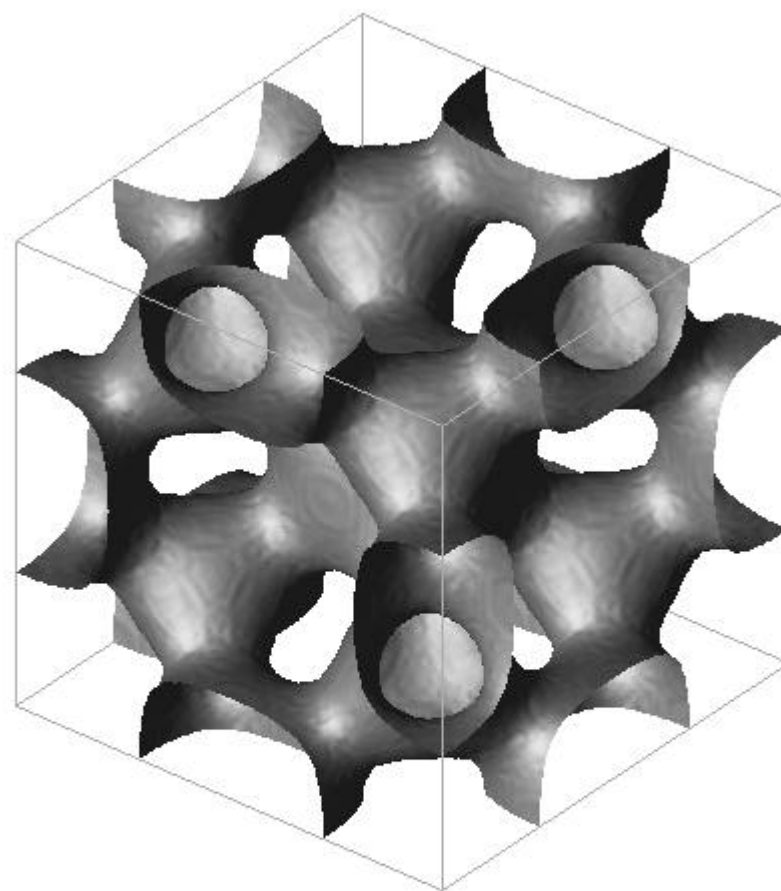


**(b)**

Fig.23



**(a)**



**(b)**

Fig.24

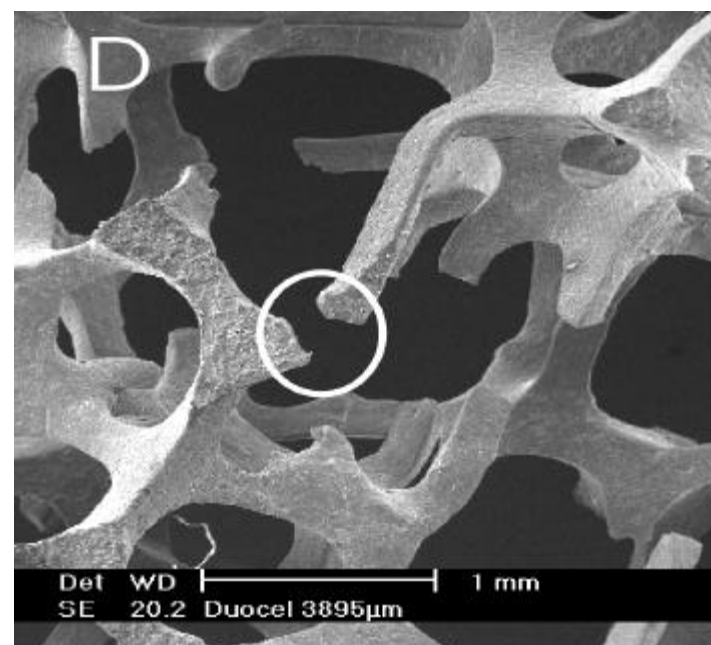
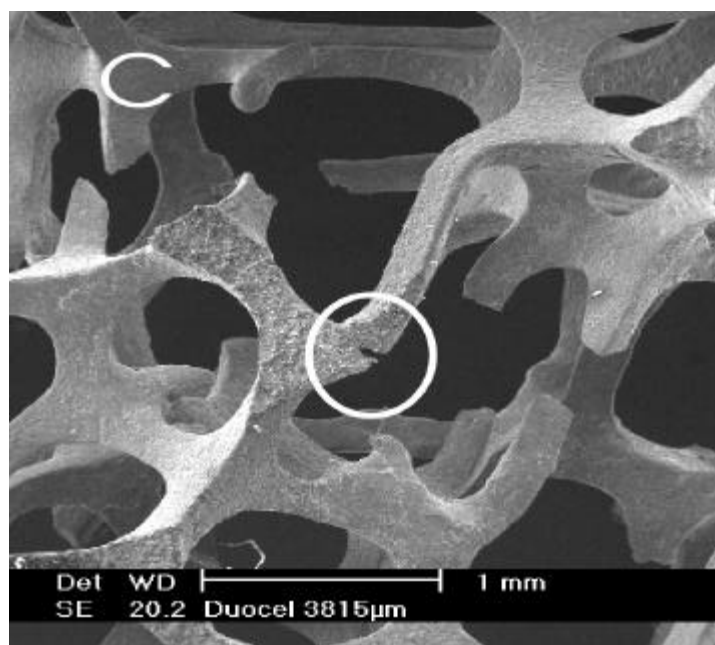
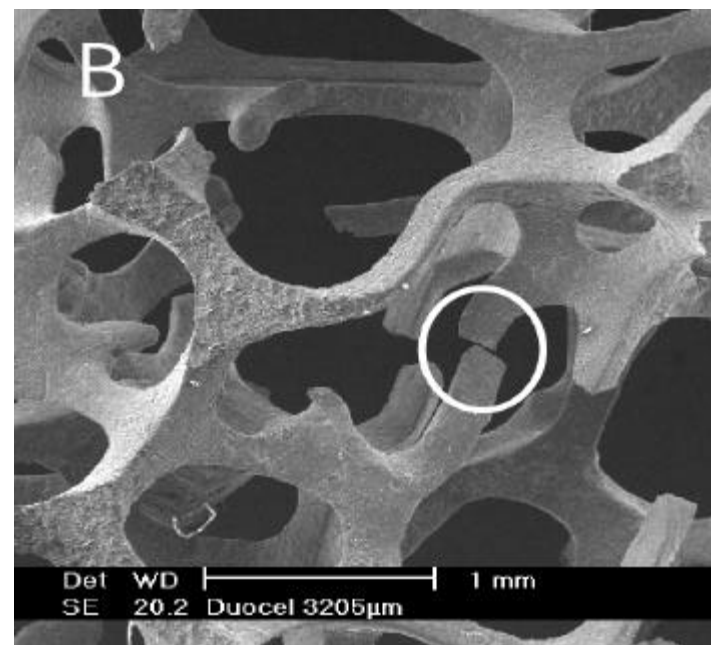
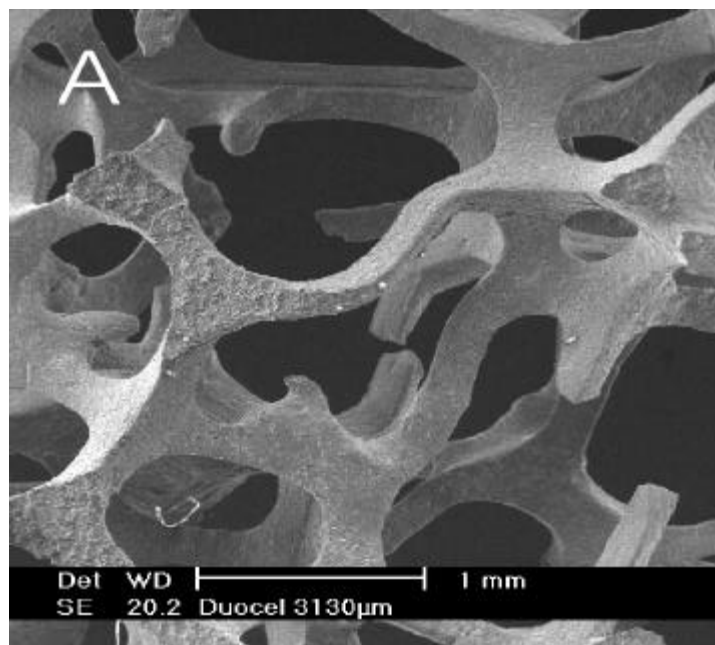


Fig.25

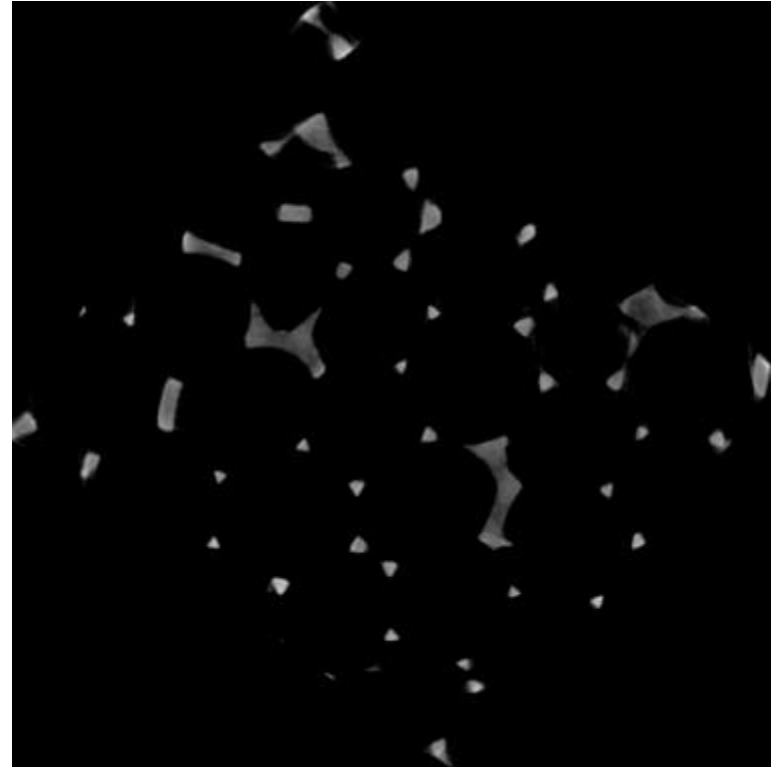
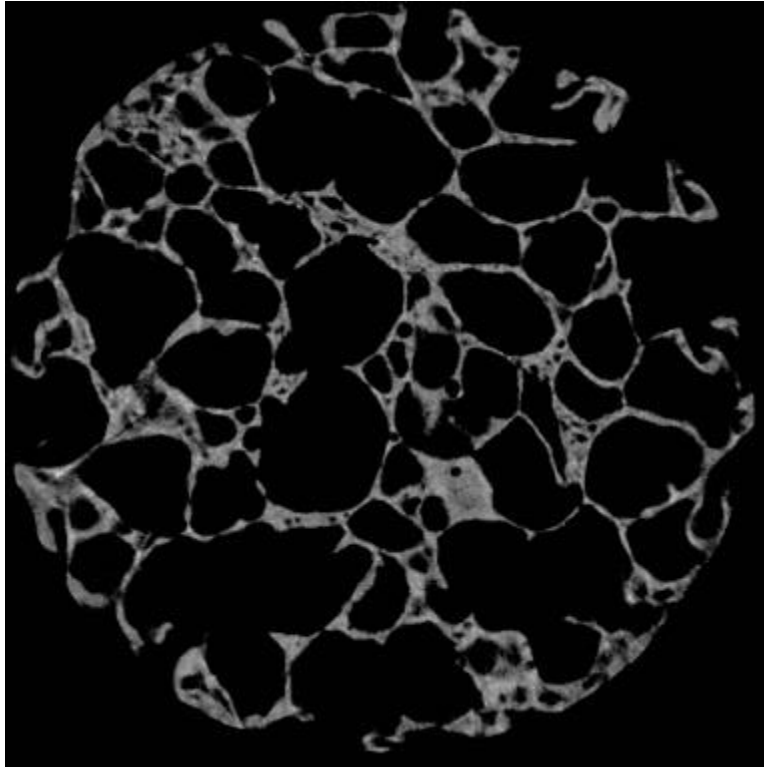




Fig.26

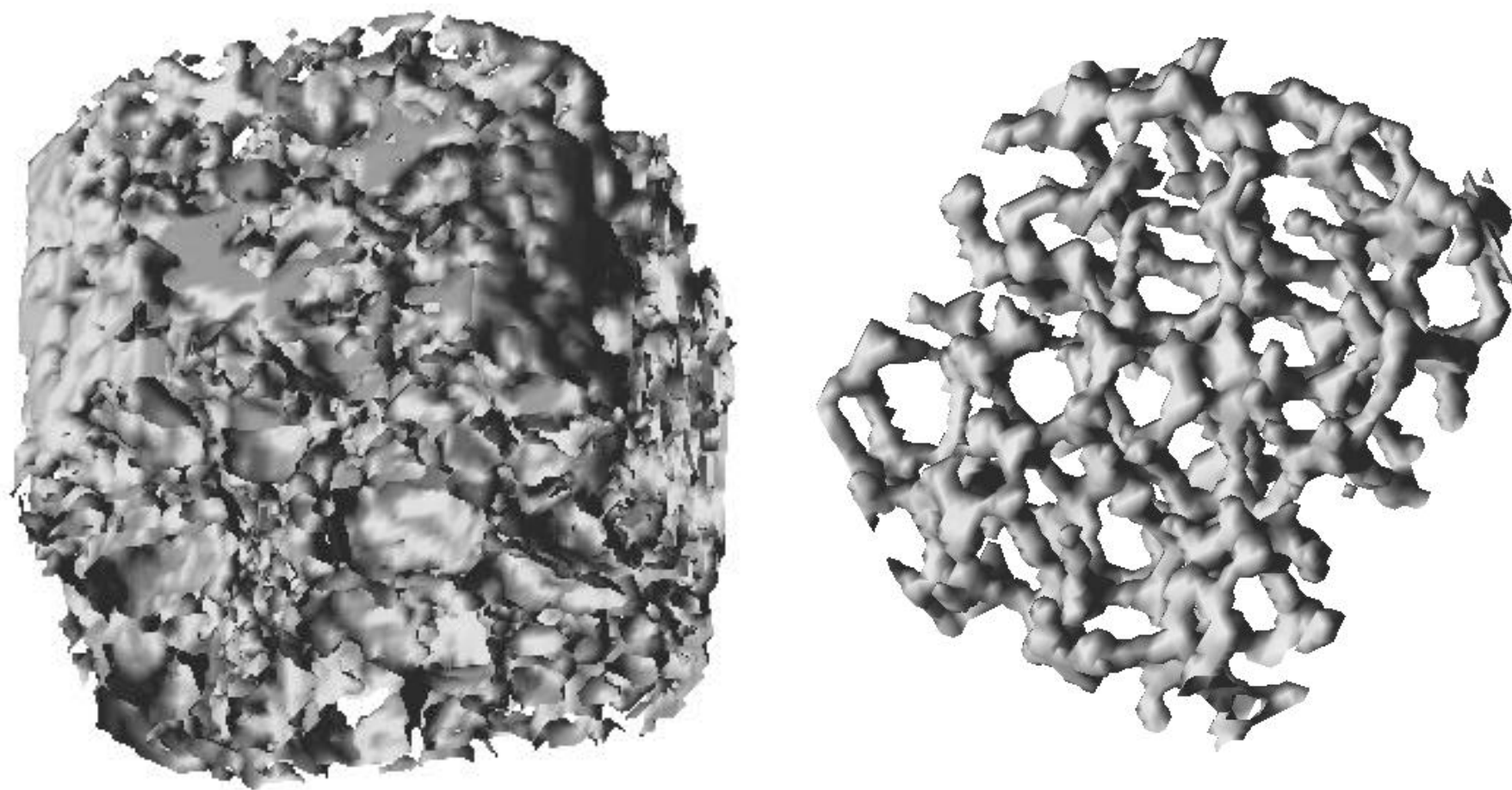


Fig.27

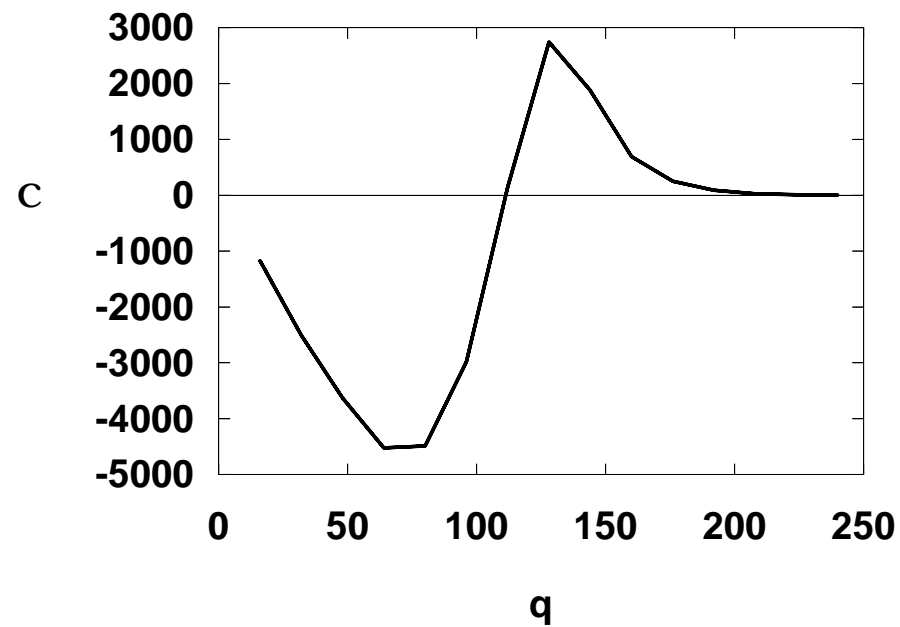
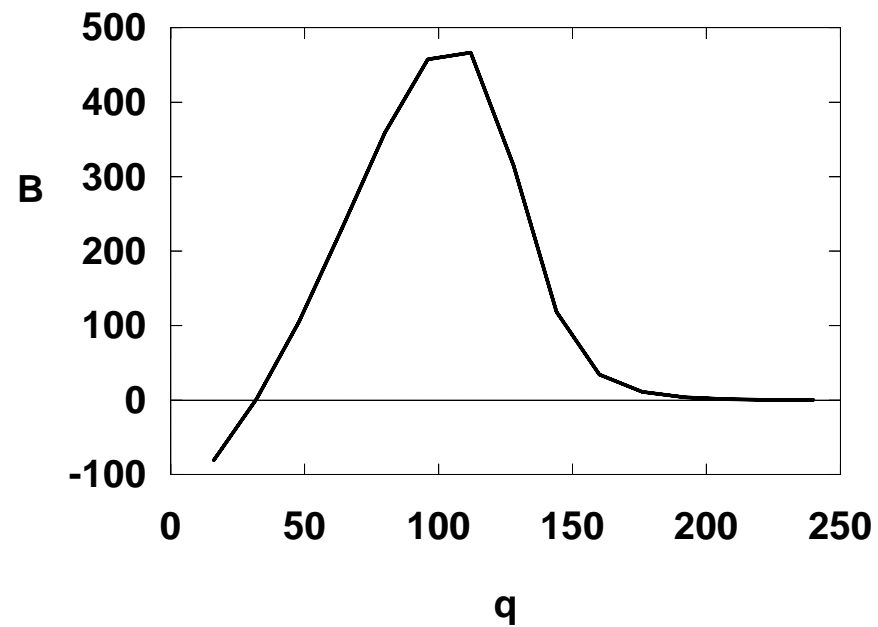
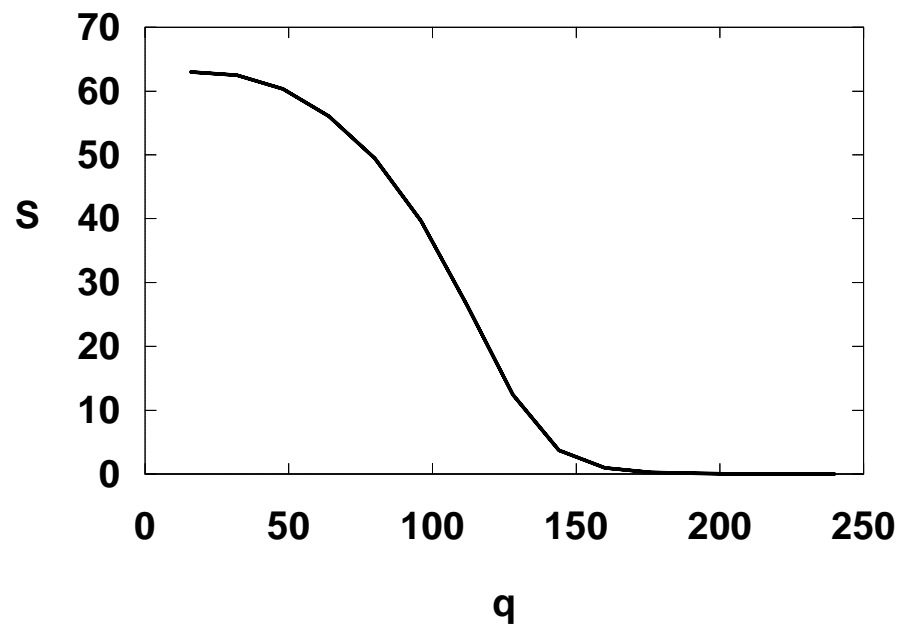
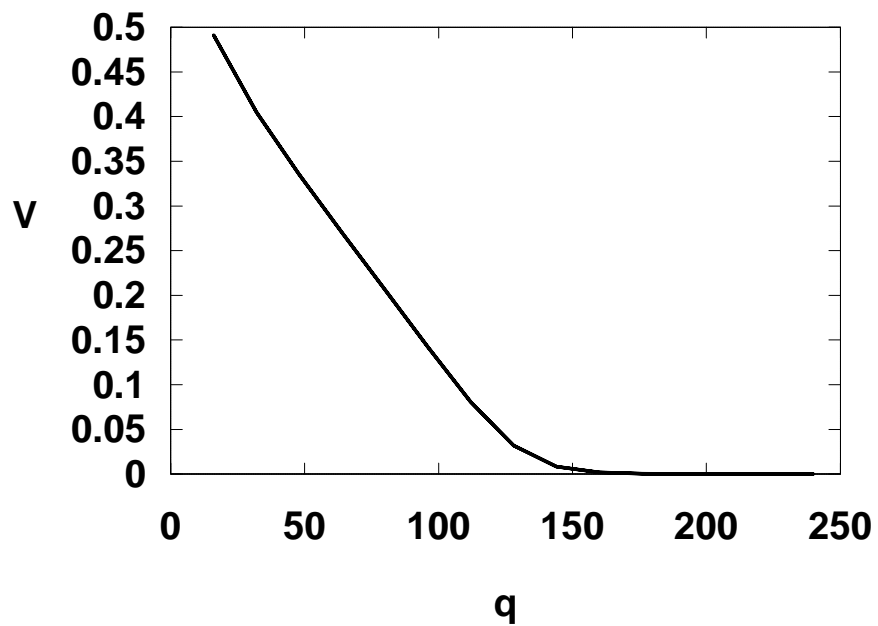


Fig.28

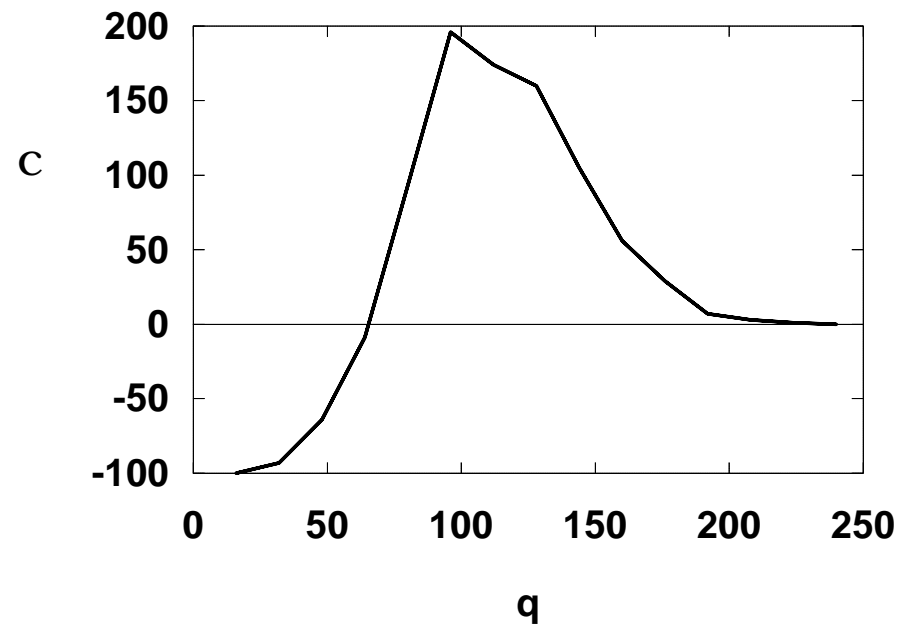
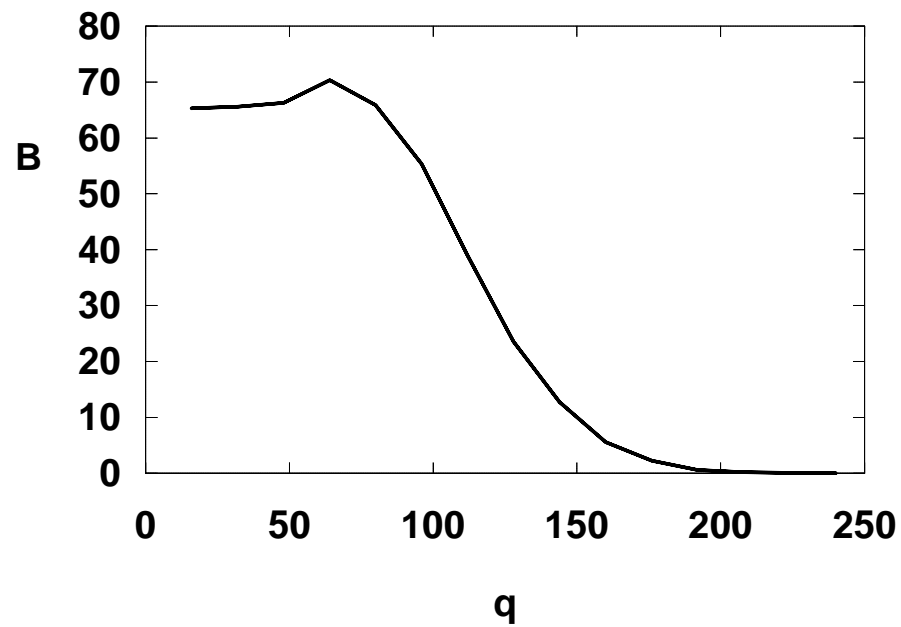
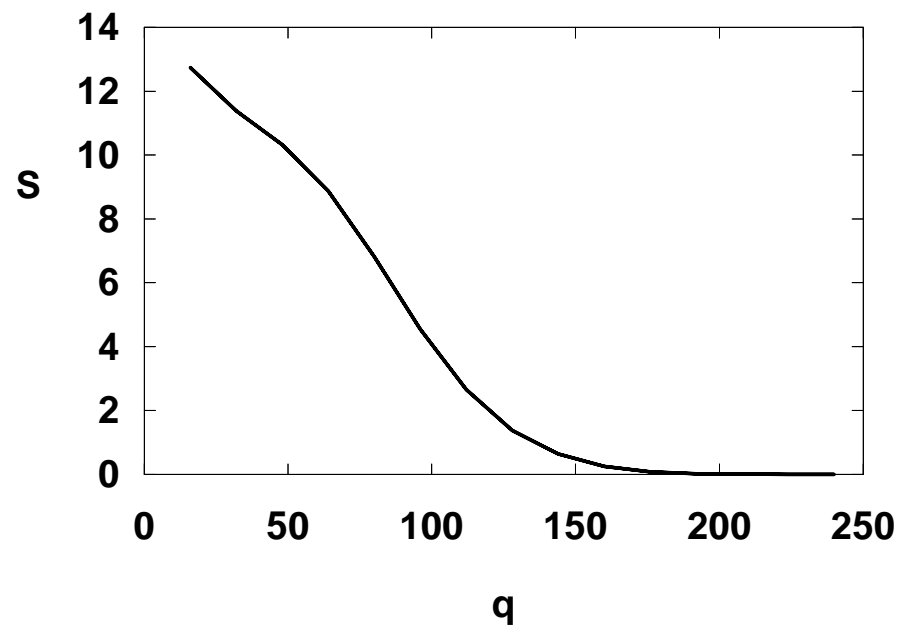
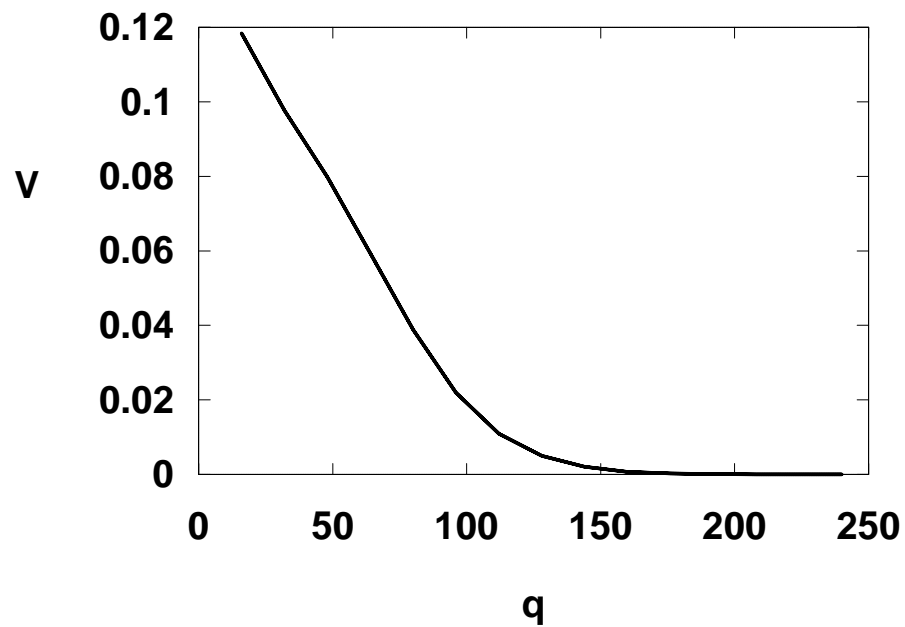


Fig.29

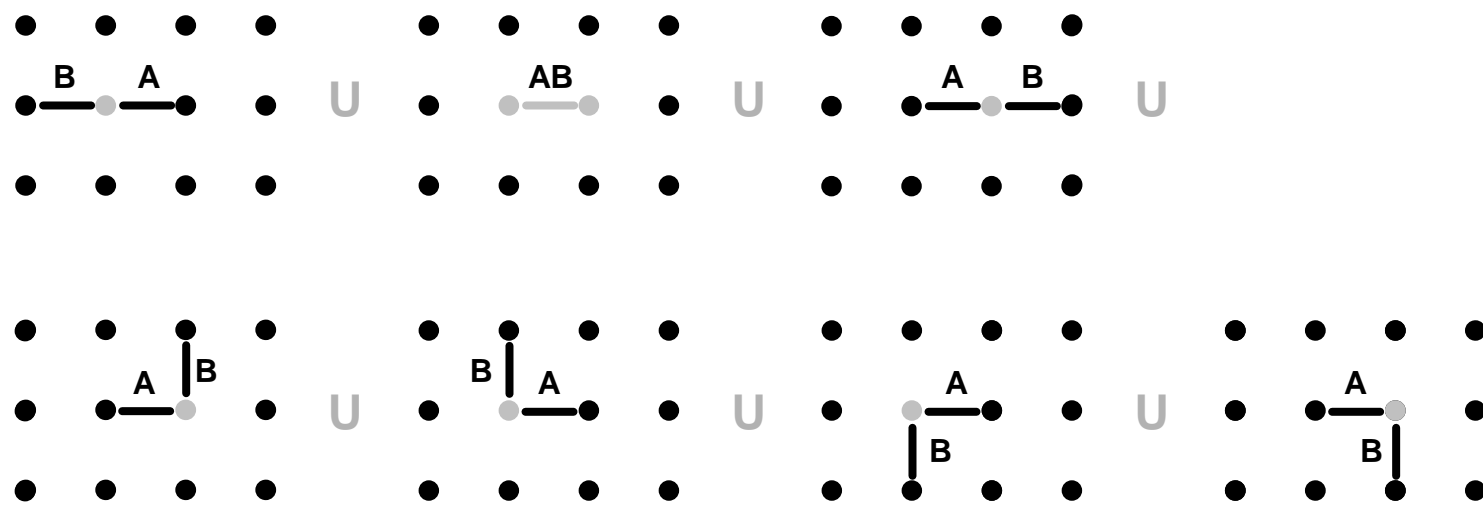


Fig.30

